CHARACTERIZATION OF ORGANIC AND INORGANIC OPTOELECTRONIC SEMICONDUCTOR DEVICES USING ADVANCED SPECTROSCOPIC METHODS

Raoul Schroeder

Dissertation submitted to the Faculty of the Virginia Polytechnic Institute and State University in partial fulfillment of the requirements for the degree of

Doctor of Philosphy
in
Physics

James R. Heflin, co-chair
Bruno Ullrich, co-chair
Wilhelm Graupner
Richey M. Davis
John R. Ficenec
Guy Indebetouw

December 14, 2001
Blacksburg, VA

Keywords: Spectroscopy, Semiconductors, Cadmium Sulfide, Conjugated Polymers, Ultrashort Laser Pulses, Two-Photon Absorption

To My Parents

And All the Other Wonderful People in My Life

Virginia Polytechnic Institute and State University

CHARACTERIZATION OF ORGANIC AND INORGANIC OPTOELECTRONIC SEMICONDUCTOR DEVICES USING ADVANCED SPECTROSCOPIC METHODS

by Raoul Schroeder

Abstract:

In this thesis, advanced spectroscopy methods are discussed and applied to gain understanding of the physical properties of organic conjugated molecules, II-VI thin film semiconductors, and vertical cavity surface emitting lasers (VCSEL). Experiments include single photon and two-photon excitation with lasers, with subsequent measurements of the absorption and photoluminescence, as well as photocurrent measurements using tungsten and xenon lamps, measuring the direct current and the alternating current of the devices. The materials are investigated in dissolved form (conjugated polymers), thin films (polymers, II-VI semiconductors), and complex layer structures (hybrid device, VCSEL). The experiments are analyzed and interpreted by newly developed or applied theories for two-photon saturation processes in semiconductors, bandgap shrinkage due to optically induced electron hole pairs, and the principle of detailed balance to describe the photoluminescence in thin film cadmium sulfide.

TABLE OF CONTENTS:

LIST OF FIGURES

LIST OF TABLES

ACKNOWLEDGMENTS

An endeavor such as researching and writing a PhD is such that it cannot be done alone. There are several people who have significantly contributed to the pieces of paper you are holding in your hands. If you enjoy reading these pages and you find them interesting, it is not just my achievement, but also that of everyone who has contributed to my education.

I would like to thank Dr. Wilhelm "Willi" Graupner for introducing me to the world of optoelectronics and conjugated molecules. Already the advisor of my master's thesis, we continued our collaboration well into the first half of my PhD, and have continued to work closely together even after he has answered the call from industry. He somehow manages to always squeeze in a little extra time in his tight schedules to help me along with problems.

Equally, I am indebted to Dr. Bruno Ullrich, with whom I have worked for the majority of my PhD thesis. He "re-initiated" me into inorganic semiconductors, and with our different backgrounds, a good deal of very fruitful work has emerged. He has encouraged me to explore even the most outrageous ideas, and has always had an open ear for any kinds of "toys" I have suggested acquiring. In the end, I think time will be the only thing in the way of even more achievements. The experiments in Chapter 4 are interpreted with his theoretical models, since he is the CdS expert.

Aditionally, the faculty and staff of both Virginia Tech and Bowling Green State University have always provided me with good advice. Dr. Robert Boughton, Diana Tussing, and Alex Hahn (the man with two golden hands) at BGSU as well as Dr. Lay Nam Chang, Dr. James Randy Heflin, Judy Faw, and Janet Sanders at Virginia Tech have helped me with any administrative problems and beyond, for which I am very grateful. Chris Thomas is a special case, since I owe her so much by now – she has always had her watchful eye over me. ☺ Thank you for all you have done!

I would like to thank everyone on my committee - namely Dr. James Randy Heflin, Dr. Guy Indebetouw, Dr. John Ficenec, and Dr. Richey M. Davis in addition to my advisors - for making the time for my qualifying exam and my thesis defense.

Additionally, the following people have worked closely with me during my PhD thesis and have helped me gain very valuable insights: Emil J.W. List, Martin Drees, Chris Williams, Dr. Satoshi Yano, Artur Erlacher, Thomas Piok, and Charuta Soman. Part of the experimental work done in Chapter 3, i.e. the measurement of the optical spectra, was performed by Charuta Soman and Artur Erlacher.

Finally, and most importantly, I wish to thank everyone who has provided me with a base on which I could build this work. My parents who have supported me emotionally, intellectually, and financially for all my life – and that is quite some time by now – my sister

Alexandra-san, and especially Jennifer, who actually keeps me going and pushing forward when I feel overwhelmed.

I would also like to acknowledge and thank all the people out there in the world, who use their brains to come up and manipulate thoughts in their mind, and come up with wonderful ideas that bring mankind further collectively. This thesis could not have been done without many, many forethinkers throughout many centuries. This work relies on many published facts from the second half of this century, and mostly from the post-1980 era, but the foundations of physics lie very deep. People like Newton, Sommerfeld, Einstein, Schroedinger, and Maxwell, to name a few, have formed new ideas, new radical ideas that paved the path for more practical ideas. So, my gratitude goes out to everyone who writes important thoughts down on paper, so it shall be discovered and rediscovered in the future, opening up new gates and windows – pun intended – for humanity.

GLOSSARY

Word.

Bandstructure:	When the Schrödinger equation is solved for a periodic potential (i.e. a crystalline solid), the electrons can be delocalized in so called bands. Two bands are extremely important for the electronic character of a material, the valence band and the conduction band. The valence band is the last band that is fully filled with electrons. The conduction band is either completely or partially empty, e.g. insulators and metals, respectively.
Semiconductors:	are a special case intermittent between a metal and an insulator. The conduction band is empty as in the insulator, however the bandgap is small enough to allow some thermal or optical excitation. Also, by chemical impurities (doping), free charge carriers are generated.
Electron volts (eV):	refer to the energy needed to move an electron against a potential of one Volt Commonly used unit in semiconductor theory and solid state physics l eV ≈ 1.6. 10^{-19} J.
Organic:	based on the most common molecules found in all life that are based on chains of carbonates with sidegroups consisting of carbon, hydrogen, nitrogen, oxygen, sulfur …
Monomer:	A unit of several atoms, which can form larger chains in repetition
Oligomer:	A chain consisting of several monomers. These chains are usually formed when two hydrogen atoms or sidegroups attached to two monomer units are re- placed by a bond to attach to another monomer unit. Oligomers usually consist of repetitive units from two to ten.
Polymer:	Oligomers with more than ten repetitive units.
Backbone:	This term characterizes the atoms and bonds along the shortest connection between the beginning and the end of the polymer chain. Attached to the backbone there are hydrogen and other atoms, or longer sidegroups.
Conjugated Molecules:	The term conjugated means that along the backbone the bonds between carbon atoms alter between single and double bonds. Since the electrons of the double bonds are delocalized, they form a band structure extended over the whole range of the effective conjugation length.

Conjugation length: Conjugation length is the length of a completely undisturbed alternating single bond / double bond segment, being planar and allowing maximum overlap of π-electrons.[1] This is the ideal case. The *effective* conjugation length is often shorter than the conjugation length, where impurities, distortions, shifts, or any other kind of irregularities limit the overlap of π-electrons.

Excitons: When a negative charge carrier, an electron, is excited into the conduction band and is bound to the positive charge (the lack of an electron, or so-called holes) left in a valence band, an exciton is formed. Excitons are just inside the bandgap, energetically, since the Coulomb attraction lowers their energy. For inorganic semiconductors, the binding energy is from five to fifty meV ($\geq 1.6\ 10^{-20}$ J) (4.9meV GaAs, 27meV CdS, 59meV ZnO),[5] less than or on the order of the thermal energy. The binding energies for excitons in organic materials are higher.

Polarons: are the "free charge carriers" in some organic materials. Due to Coulomb interactions with the backbone, a charge carrier slightly deforms the surrounding bonds -thus lowering its energy. Polaronic states are found in the forbidden zone, usually close to the valence band and the conduction band.

Absorption: (spectra, edge) Absorption is basically the damping of the electromagnetic field inside a material. Talking about absorption spectra in the context of solar cells usually signifies the absorption spectra from the ultra-violet (UV) region via the visible (Vis) part of the spectrum to the near infrared (NIR). The absorption edge is found at the energy at which allowed optical transitions between the two energetically closest states are possible. For free electron/hole transitions it is the energy difference of the band gap, for bound excitons it is the bandgap energy difference minus the binding energy for the exciton. For solar cells, semiconductors with allowed optical transitions from one to four Electron Volts ($\sim 1.6\ 10^{-19}$ J) are interesting.

Optical Density (OD): determines on a logarithmic scale, how strongly a material absorbs. It is defined as the negative decadic logarithm of the relative transmission. This only holds true for the case that the sum of the transmission and absorption is 100%; so the reflectivity and scattering have to be negligible. Especially the former condition is difficult to achieve.

Photoluminescence: (PL) Excitons created by absorption of a photon can recombine radiatively or non-radiatively. The photoluminescence spectra give

an idea about the probability that radiative recombination occurs and at which energies the material absorbs and emits.

Trap state, Trap: A chemical impurity (either a dopand, e.g. an atom that can bind or donate an electron, or a crystal structure defect) in a semiconductor forms so-called trap states. The trap state attracts a charge carrier that is localized at the trap for a limited amount of time.

Sandwich Device: This refers to a device where the active layer, i.e. a thin film semiconductor, is "sandwiched" between the electrodes. By making the active layer very thin, the internal fields (due to the different potential of the electrodes) are high (on the order of 5 $10^6 Vm^{-1}$, where O.5 V is the voltage by created by the difference in workfunctions of the electrodes, and 100 nm is a typical length for organic solar cells).

Airmass Spectra: (AM Spectra) To measure the performance of Solar Cells in relation to the sun's intensity on Earth, one uses the normalized AM spectra. The number after AM describes how much atmosphere the light has to travel through before reaching Earth's surface in relation to the shortest path (when the sun is in the zenith). There are three very common ones:

1. AM 0 spectrum: It describes the solar intensity outside the Earth's atmosphere and ionosphere. Thus, it is very close to a 5800K black body emitter, minus some absorption in the outer atmosphere and corona of the sun. Matching this intensity distribution is important for satellites and interplanetary probes.

2. AM 1 spectrum: This is the solar intensity at a ninety degree angle, the zenith. Of course, this value is only useful at very rare times during the day and limited locations on Earth. In addition to the AMO spectrum there are features like scattering of blue light (thus "red shifting" the maximum of the spectrum) and absorption peaks from molecules (ozone absorbs highly below 300nm in the ionosphere, H2O around 700nm in the atmosphere).

3. AM l.5 spectrum: This is the most commonly referenced spectrum. It measures the light intensity at a forty-five degree angle and can be seen as a good average of daytimes and locations around the world. Matching this intensity distribution is one of the major goals of solar power engineers.

HOMO: The Highest Occupied Molecular Orbital is defined as the bonding electronic state highest in energy and can be seen as something similar to the highest state of the occupied valence band in an

	inorganic semiconductor. Since the electronic states in a polymer or oligomer are not dense enough to be realistically described as bands, the molecular orbitals are a better approximation. The orbitals below the HOMO are often described as HOMO-l, HOMO-2 …
LUMO:	The LUMO is the lowest anti-bonding electronic orbital in a molecule. It can be seen as similar to the conduction band. The levels above the LUMO are often written as LUMO+l, LUMO+2 …
Self-absorption:	(parasitic absorbtion). Absorption of light in the active layer itself, either altering the shape of the emission spectrum, or the shape of the photocurrent spectrum, when electron/hole pairs are created, but do not contribute to the current.
Doping:	Introduction of charge carriers into a semiconductor either by chemical doping (permanent) or injection/optical creation (temporary).
Short-Circuit Current:	Current measured at zero external resistivity. The short circuit current directly depends on the number of charge carriers created and thus depends linearly on the intensity of the absorbed light (disregarding any trapping effects)
Open-Circuit Voltage:	Voltage measured at infinite external resistivity. Depends on interface qualities, workfunctions of the electrodes, logarithmically on the light's intensity.
Bias (forward, reverse):	A bias is an external voltage applied to a diode (semiconductor sandwich with n- and p-doping, respectively). When the negative pole of the external voltage is attached to the n-doped semiconductor, it is called forward bias, when the positive pole is attached to the n-doped semiconductor, it is called a reverse bias.
Principle of detailed balance:	Description of the photoluminescence by describing the emission in the material with Planck's photon energy distribution and applying the self-absorption of the material to the distribution.

Chapter 1

MOTIVATION AND EXPERIMENTAL OUTLINE

There is a single light of science, and to brighten it anywhere is to brighten it everywhere.

- Isaac Asimov

1.1 General Introduction

The inquisitive mind has a thirst for knowledge. The driving force within a scientist is to gain an understanding of the world – an understanding more profound than the superficialities that we encounter in our every day life. My interest for semiconductor physics, specifically organic conjugated materials, was already sparked during my master's thesis research.[1]

I think that being a true scientist means being addicted to finding the truth. In a lot of ways the scientist's work today is driven by the need to get funding and to publish papers. But the truth is that we strive to know what makes something tick. Once we know, we also need to share this knowledge, but the most important part is just the understanding itself. This is the motivation that keeps me going, the need to see behind the scenes of nature, and it is a very powerful source.

1.2 Motivation

Another important motivation for me was that I think it is time to look ahead and really invest into renewable resources. This is why part of my work has always been devoted to understand the principles of photovoltaics and how to improve the efficiency and stability of new systems. Ultimately, I hope that we can use the sun as a source much more effectively. Let us consider one of the most basic and most important laws of thermodynamics:

$$\Delta S \geq 0\,, \tag{1-1}$$

where ΔS is the change of entropy in any (circular) process.

The only time when Equation (1-1) is equal to zero is in the hypothetical case of a circular reversible process – read: never. Life as we know it, and most processes in this universe, increases entropy. Life on Earth would be impossible without the low entropy sunlight. The more conversions of energy we choose to apply to the basic low entropy sunlight, the more inefficient the process is. Now, the amount of light arriving from the sun at the outskirts of the atmosphere does not change noticeably in the time frame of years, nor is it influenceable. Ever after, it is in the hand of plants, and to some extent that of humans to make the most of it.

Human efforts, however, do not strive to excel in philosophical terms outlined above, but are directed towards the advancement of the individual and the species. A lot of that is technical advancement, and the pride to show off new gadgets is unmatched. The trend to make things smaller and more efficient has lead to a strong demand for new materials for displays, photocells, accumulators and other objects that have been so strongly integrated into our lives. Semiconductors have been subject to very intense research, both to try and get the most out of more conventional inorganic semiconductors, such as silicon (Si) or gallium-arsenid (GaAs) or other more conventional techniques, such as the step from regular cathode ray tubes to thin tunneling displays that are in the prototype stage now and ready to conquer; as well as introducing organic conjugated molecules into basic semiconductor research. Clearly, inorganic semiconductors have different qualities than their organic counterparts, and often, these two need to be worked together into one solution to provide the desired properties.[3]

Part of me wants to have the philosophical outlook and improve life itself. Part of me also wants to be on the forefront of introducing new technical concepts. In my thesis, the esteemed reader will find that I tried to pick up some of the concepts outlined here and let them influence my work. I am in the extremely fortunate position to be advised by two highly experienced people in two very different fields, and learning the best of both worlds, so to speak. Two chapters will be entirely devoted to organic semiconductors and the application of advanced spectroscopy methods to determine basic physical properties of these materials. There will be one chapter on simple inorganic CdS structures, and an interpretation of the film qualities using two-photon excitation. One chapter will discuss the layer analysis of a vertical cavity semiconductor laser (VCSEL), equally probed with two-photon excitation. And finally it will be shown how to combine the different photovoltaic properties of CdS and a terrylene based material to create a photovoltaic cell with well-designed properties.

This is meant to be a brief introduction into this thesis, so that the esteemed reader can see what motivated me to go for a PhD, to do the research required for it, and to write this thesis; also it gives an outline of what is to follow. Clearly, when I started my PhD studies I had no idea that in the end such a diverse work would emerge, and it is most interesting for me to note what all the results that I had accumulated over the past 2.5 years, are. I hope you will enjoy reading these pages as much as I enjoyed writing them.

1.3 Experimental Setups

1.3.1 Photocurrent Measurements

Depending on the needs of spectral range for the photocurrent measurements, two setups were at our disposal.

For measurements in the range of 250 – 800 nm, it consisted of:

- CVI 150 W Xenon lamp (an Oriel Xenon lamp at Virginia Tech)
- CVI CM110 monochromator
- UV lens, f = 10cm
- SRS optical chopper (optional)
- Keithley 485 picoammeter
- Keithley 2000 multimeter (only at Bowling Green State University)
- SRS 530 lockin amplifier

The typical impinging power on a device with 1 nm FWHM on a device was on the order of 10^{-5} W.

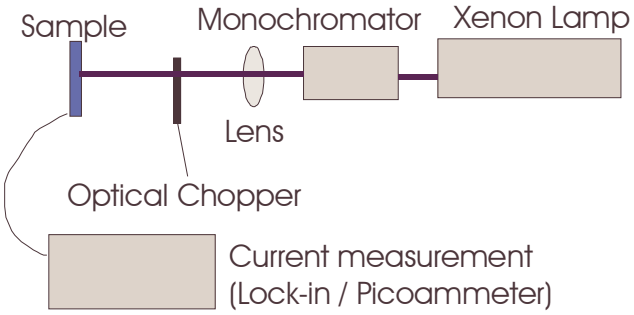

Figure 1 Photocurrent measurement setup for the range of 250-800 nm

For measurements in the range of 400 – 1200 nm (Bowling Green State University only):

- SPEX 300 W tungsten lamp
- SPEX 500 mm monochromator
- Lens, f = 15 cm

- SRS optical chopper (optional)
- Keithley 485 picoammeter
- Keithley 2000 multimeter
- SRS 530 lockin amplifier

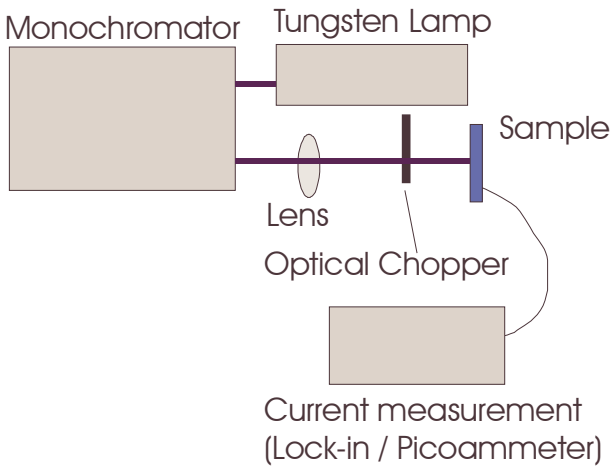

Figure 2 Photocurrent measurement setup for the range of 400-1200 nm

The output power curves were first measured with a calibrated silicon diode, and the photocurrent was divided through the power output spectrum to find the ampere per watt (A/W) spectra.

1.3.2 Transmission measurements

Transmission spectra were collected similarly; the silicon diode placed behind the sample holder and the current through the diode measured once with and once without the sample in place, while the wavelength was varied. Division of the two curves led to the transmission spectrum. Again, dependent on the desired wavelength of the transmission spectrum, either one of the two previously mentioned (1.3.1) measurement setups was used. The setup is the same as in Figure 1 or Figure 2, respectively, but the silicon diode is placed behind the sample and connected to the picoammeter, as shown below.

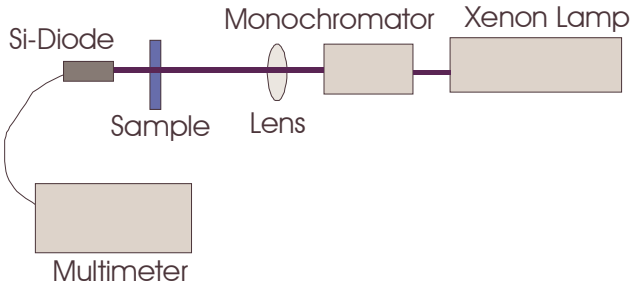

Figure 3 Transmission measurement setup for analysis of the 250-800 nm range.

1.3.3 Photoluminescence measurements

The excitation was provided either by the Xenon lamp CVI monochromator combination, or, in most cases, by Ar+ and HeNe lasers, with excitation wavelengths of 457 nm, 475 nm, 487 nm, 517 nm, 532 nm, and 632 nm. The emission spectra were collected with an Ocean Optics fiber optics spectrometer S2000 (USB).

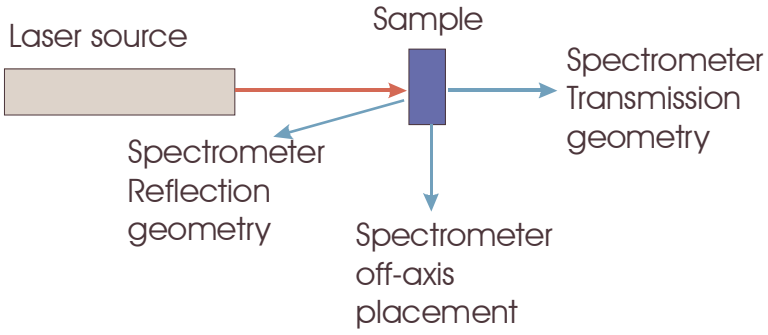

Figure 4 Photoluminescence measurement setups

1.3.4 High power femtosecond pulses

For the two-photon excitation experiments, a Coherent femtosecond laser system was used. A Coherent Innova Ar+ 30 W output power laser pumped a Coherent Mira Ti:Sapphire femtosecond oscillator and a Coherent RegA femtosecond amplifier.

The cw output power of the Mira was typically around 500 mW, with a pulse length of 200 fs FWHM and a repetition rate of 1+ MHz. The cw output power of the RegA was around 1 W, with a repetition rate of 249 kHz. Thus, the energy of pulse is three orders of magnitude higher with the amplifier locked into the system. The energy per pulse is

calculated to be 4 μJ, and the average power of the pulse is 20 MW average or 31 MW Gaussian peak power. When focused down to a radius of 50 μm, the intensity of the laser pulse is 180 GW/cm^2 mean intensity, and 276 GW/cm^2 peak.

Chapter 2

THEORETICAL CONSIDERATIONS

The great tragedy of science – the slaying of a beautiful hypothesis by an ugly fact.

Thomas Huxley

2.1 Bandstructure Theory

This part of the chapter is by no means supposed to be a thorough introduction into one of the most complicated theories in semiconductor physics. It is designed to be a short excursion and to establish the foundation on which I will build the rest of the thesis. These coming paragraphs will loosely follow a book recommended to me by Dr. Ullrich, *Semiconductor Optoelectronics*.[4]

2.1.1 Bloch's Ingenious Theorem

(Remark: It is not necessary to read through the next two sections to understand the remainder of the thesis, albeit useful.)

Giving a mathematical description of an electron in free flight? Piece of cake! An electron under the influence of a single ion – a scattering problem that is still relatively simple to solve. Many electrons feeling the presence of many ions, such is the case in crystals, is a problem that is much more complicated and can be taken to any degree of realism without ever becoming boring.

It was Bloch who simplified this problem, however. Realizing that most solid state crystals exhibit a certain degree of order, he saw that an electron effectively could not tell, in which repeated unit of the ordered whole it was. As such, he postulated that the solution to Schroedinger's equation in a crystal (below) can be expressed as the product of a planar wavefunctions and a crystal potential specific function,

$$\left(\frac{-\hbar^2}{2m_0}\nabla^2 + U(\mathbf{r})\right)\psi(\mathbf{r}) = E\psi(\mathbf{r}), \qquad (2\text{-}1)$$

where: ħ *is Planck's number,* m_0 *is the electron mass,* U(**r**) *is a potential that suffices the relation* U(**r**) = U(**r**+**R**) – **R** *being a vector to the next repetition unit -* ψ *is the wavefunction of the electron,* E *is the energy eigenvalue of the electron.*

This simplifies our problem a lot. We can now write the wavefunction as,

$$\psi(\mathbf{r}) = e^{i\mathbf{kr}} u_k(\mathbf{r}), \tag{2-2}$$

where **k** *is the momentum vector, and* u_k *is the wavefunction within one unit cell. The only difficulty is to find* u_k*, and depending on our requirements, this function can be quite complex.*

However, it turns out that for very many semiconductors, the highest partly occupied electron shells (and therefore the chemically active ones) are s and p shells. This holds true for the most interesting classes of semiconductors, II-VI, III-V, and IV inorganic semiconductors, as well as organic semiconductors that mostly rely on sp^3-hybridized carbon bonds. Bearing that in mind, at least the bandstructure for the conduction band within the first Brillouin zone can be easily described. The minimum of the conduction band at $k = 0$ is always due to the s-orbital, because of the symmetry requirements of an $l = 0$ electron. Any minimum of the conduction band at $k \neq 0$ is due to p-orbital or s+p degenerate orbitals. When the absolute minimum of the conduction band occurs at k = 0, the semiconductor is called a direct semiconductor. This is due to the fact that the maximum in the valence band is always at $k = 0$, and only transitions where the minima lie very close in terms of k are possible without the additional interaction of a phonon – a lattice vibration small amounts of energy but significant amounts of momentum. Photons themselves, in fact, carry very little momentum:

$$k_{Ph} = \frac{2\pi}{\lambda_{Ph}} = \frac{2\pi\nu_{Ph}}{c} = \frac{\hbar\omega_{Ph}}{\hbar c} \cong 1.5\times10^7\, m^{-1}eV^{-1} * E_{Ph}(eV), \tag{2-3}$$

where: k_{Ph} *is the photon momentum,* ν_{Ph} *is the photon frequency,* c *is the speed of light in the medium,* E_{Ph}*(*eV*) is the photon energy in Electronvolts.*

The k-scale of the Brioullin zone, however, is on the order of magnitude of 10^{10} m^{-1}. Thus, the momentum of hundreds to thousands of photons together would be required for a transition to a conduction band minimum away from $k = 0$, which is typically located at the *X*-symmetry position. This is called an indirect transition, and is achieved via an electron-photon-phonon process. With two particles involved, transitions are less likely to occur, and non-radiative recombination is dominant compared to luminescent recombination. This is the reason why all optoelectronic emissive devices are based on direct bandgap semiconductors.

2.1.2 Bandstructure Calculations, Introduction

The conduction band can be described, near the minimum of the edge, with a parabolic function. This is also called the "*nearly free electron bandstructure*". A typical function for the conduction band minimum in a direct semiconductor is shown in Figure 5 below, for a diamond type semiconductor like silicon is shown in Figure 6:

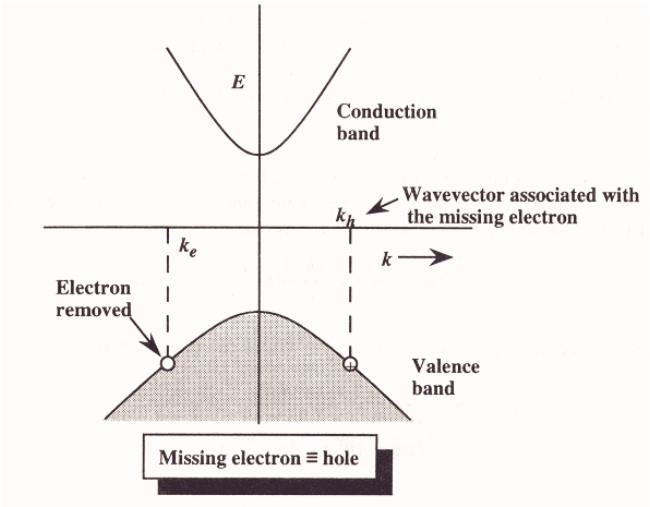

Figure 5: Simplified bandstructure schematics in k-space. Parabolic bands using the almost free electron band model near the bandgap edge of a direct semiconductor.[4]

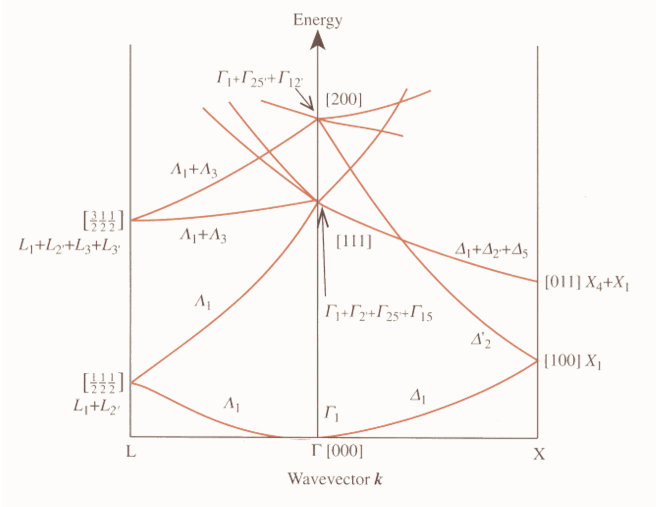

Figure 6 Band structure of nearly free electrons in the reduced zone scheme for silicon.[5]

Whereas the approach in Figure 5 is rudimentary at best, Figure 6 shows how to get reasonable results, using the following method. First, a non-zero crystal potential is assumed, and the wavefunctions are symmetrized to the potential. That way, the structural information of the lattice in question is not lost with the simple approach of nearly free electrons. Afterwards, the crystal potential is taken to zero. The results are already a reasonable approximation for a diamond type lattice.

However, for a more detailed description, the potential in the Schroedinger equation needs to represent the lattice better. It is clear that the minimum of the conduction band depends mostly on one position in the lattice, since the propagation vector k is close to zero in the direct semiconductor. To model the bandstructure in a larger area, the potentials need to be approximated more realistically – which will be discussed over the next few paragraphs.

One important method that delivers realistic results with little effort for diamond type semiconductors is the *pseudopotential method*.[5]

If we were to solve for the valence electron functions in the crystal for real, we would run into difficulties. This is mainly due to the fact that near the core, valence electrons have very oscillating wavefunctions since they are orthogonal to the core wavefunctions. However, the interaction of these two wavefunctions gives a "pseudo kinetic energy", which can just be regarded as the Pauli exclusion principle. That means that the exact shape of the valence electron wavefunctions near the core has very little influence on the bandstructure. Thus, the real core potential can be approximated by a weaker, smoother potential, the so-called pseudopotential. The Schroedinger equation has the same form as Equation (6-1), but the potential is now the pseudopotential, and the wavefunctions are the pseudo-wavefunctions.

$$\left(\frac{-\hbar^2}{2m_0}\nabla^2 + V_{\mathrm{ps}}(\mathbf{r})\right)\psi_{\mathrm{k}}(\mathbf{r}) = E\,\psi_{\mathrm{k}}(\mathbf{r}) \tag{2-4}$$

The pseudo-wavefunctions will be smooth, due to the pseudopotential, and similar to the free electron wavefunctions, so they can be approximated by a linear combination of plane waves.

$$\psi_{\mathrm{k}}(\mathbf{r}) = \sum_{(h,k,l)} a_{(h,k,l)} \left|\mathbf{k},(h,k,l)\right\rangle \tag{2-5}$$

where: (h,k,l) *is a reciprocal lattice vector defined by the Miller indices,* $a_{(k,k,l)}$ *is a weight factor,* $\mathbf{k}$ *is the momentum vector of the plane wave.*

The $a_{(h,k,l)}$ are zero unless (h,k,l) are an actual reciprocal lattice vector for the investigated crystal. This is due to the fact that the matrix elements of the pseudopotential are defined by the Fourier components of the pseudopotential:

$$\left\langle \mathbf{k}\left|V_{ps}\right|\mathbf{k},(h,k,l)\right\rangle \propto \frac{1}{\Omega}\int_{\Omega} V_{ps}\, e^{-i\mathbf{r}^*(h,k,l)}\, dr = \tilde{V}_{(h,k,l)} \tag{2-6}$$

The Fourier components are defined as the form factors and structure factors, where the structure factors only play a role when there is more than one atom per unit cell. These Fourier components are, for example, extremely important for X-ray analysis, where they are important to interpret the individual strength of the diffraction peaks correctly.

In Figure 7, the calculated electron bandstructure of silicon is shown.

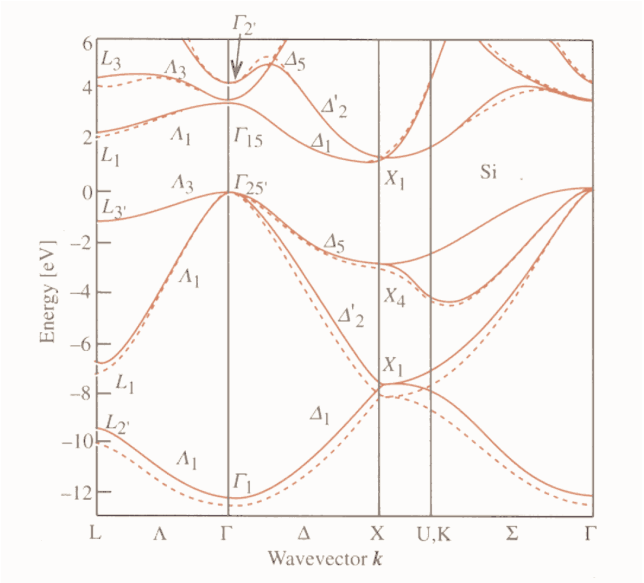

Figure 7 Calculated silicon bandstructure using the pseudopotential method.
The solid lines represent a nonlocal approach, the dotted lines a local one.[5]

Comparing Figure 7 to Figure 6, we see that the pseudopotential approach gives more detailed result, especially around the ***X*** symmetry point, whereas at the ***L*** and ***Γ*** point, the results are rather similar.

To find the form factors, one can either apply the empirical pseudopotential method, which relies on the comparison of the calculation with variable potentials and experiments – or self consistent approach, which takes a theoretical model for the potential, where the resulting wavefunction (and its associated potential) is compared to the initial potential.

Another method of calculating bandstructures, often used for organic molecules, is the LCAO method, the linear combination of atomic orbitals.

The base of this method is that the atomic electron wavefunctions can be superposed to describe electron wavefunctions in a crystal. In crystals it is often used to describe the valence band rather than the conduction band, because it is a tight binding approach. Also,

the fit parameters in the bandstructure calculation are the so-called overlap parameters, which actually have a physical meaning, interpreted as the interaction with crystal electrons.

As mentioned earlier, in most cases only s and p shell valence electrons contribute to the bonds and the bandstructure. S electrons can only form sigma type bonds (in axis bonds), whereas p electrons can form both sigma type bonds as well as pi type bonds (out of axis). Pi type bonds have lower binding energies, the electrons are therefore more delocalized. Pi type bonds typically occur in conjuction with sigma type bonds as double bonds or triple bonds. The s shell and p shell electron bonds are shown in Figure 8 and Figure 9, respectively.

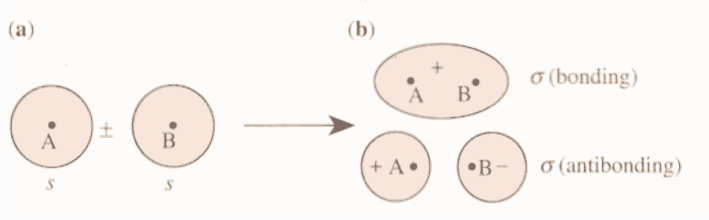

Figure 8: 2 s-electron forming sigma bonds.
When A and B have symmetric wavefunctions, and thus anti-symmetric spinfunctions, the bond is σ bonding, if they have antisymmetric wavefunctions and symmetric spinfunctions, the bonds is σ anti-bonding.[5]

The bond overlap parameters are found as the matrix elements of the interaction Hamiltonian in the spherical harmonic representation. There are only 5 non-zero matrix elements of the interaction Hamiltonian:

$$\begin{aligned} \langle s|H|s\rangle &= E_{ss\sigma} \\ \langle s|H|p_z\rangle &= E_{sp\sigma} \\ \langle p_z|H|p_z\rangle &= E_{pp\sigma} \\ \langle p_x|H|p_x\rangle &= \langle p_y|H|p_y\rangle = E_{pp\pi} \end{aligned} \quad , \qquad (2\text{-}7\ \text{a-d})$$

where: s *is the azimuthal wavefunction of the s orbital,* p_x, p_y, *and* p_z *are the three distictnce azimuthal wavefunctions of the p orbital, and* E *is the bond energy. The difference in energy of bonding and antibonding bonds is twice that energy. It is assumed that the z-axis is along the bond, and thus the x-axis and y-axis are interchangeable.*

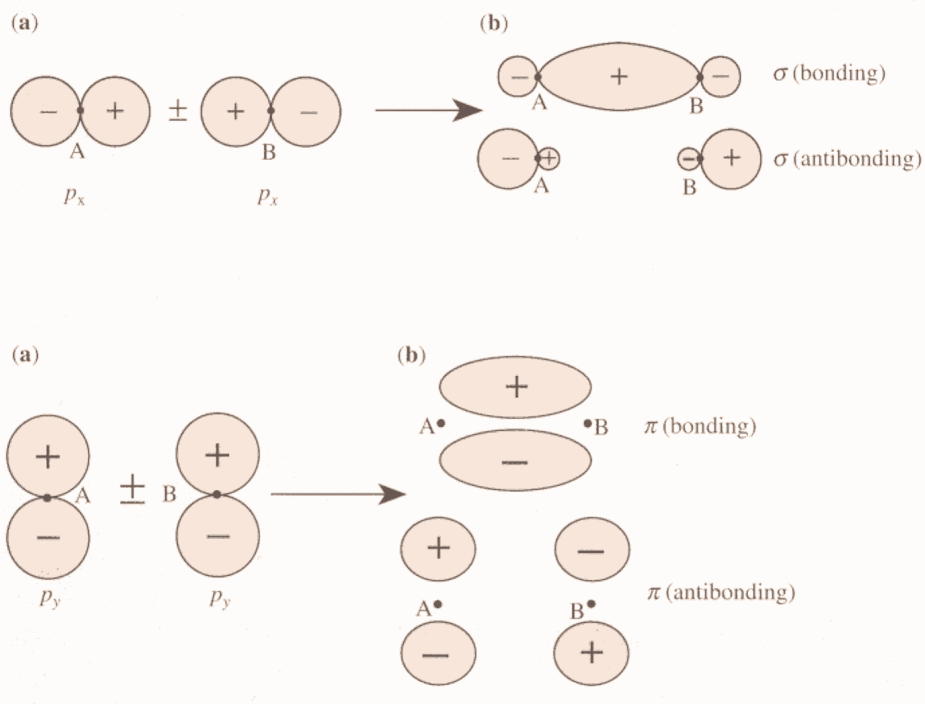

Figure 9: Bonds formed by p-shell electrons.
Top shows in-axis σ bonds, again symmetric wavefunctions and antisymmetric spinfunctions are called bonding σ bonds, and antibonding vice versa. Bottom shows out-of axis π bonds. It is seen that the overlap of the two wavefunctions is not as strong in a π bond than in a sigma bond, and the binding energy is lower. By the same token, the repulsion of the antibonding π bond is also weaker.[5]

A great advantage of the LCAO method is that when calculating the bandstructure of compounds, the overlapping parameters can be estimated from pure materials. Just from the knowledge of the lattice constants and the crystal structure, important knowledge can be obtained. In the figure below, three type IV semiconductors are compared. α-Sn is interesting in that it is actually a metal, because of the higher lattice constant and thus lower overlap energy.

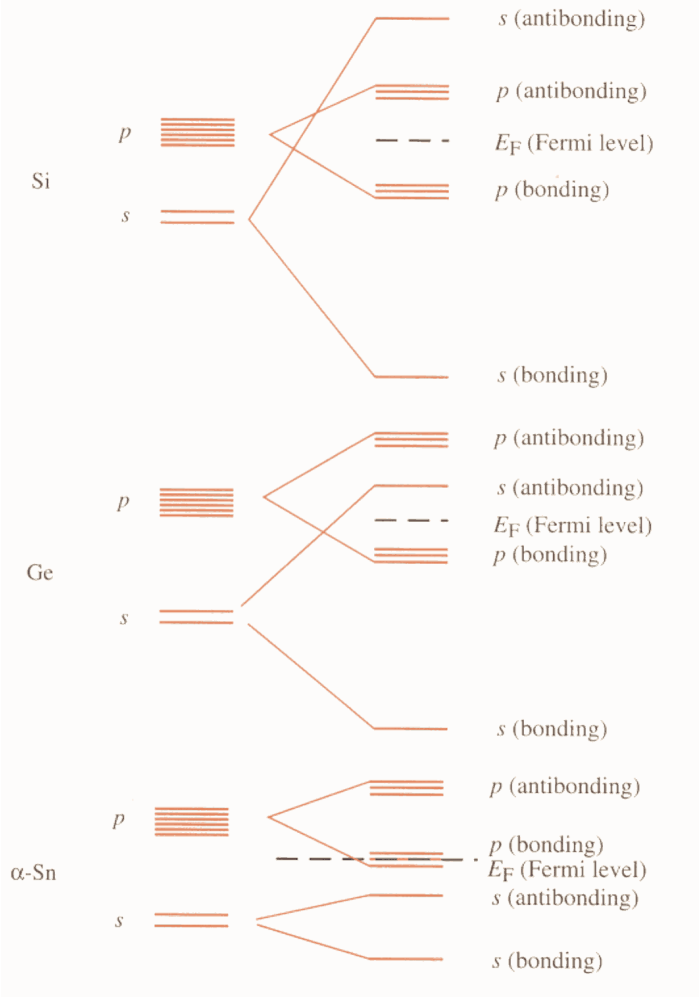

Figure 10: Overlap parameters and band splitting in the type IV-semiconductors silicon, germanium, tin.
α-tin acts like a metal due to the position of the Fermi level (partially filled p orbital) [5]

Not only is the LCAO method very useful for deriving qualitative results of the bandstructure and quantitative results of the valence bands, it is also the method of choice for many bandstructure calculations in organic semiconductors. Above all, the continued inclusions of further bonds to repetition units allows us to understand the nature of the molecular orbitals in oligomers and short polymers.

2.1.3 The molecular levels of organic semiconductors

(Editorial remark: This section has been taken largely from my second guest lecture for the 2001 summer workshop at BGSU. Its style is different from my previous writings, which by all means should be a delightful diversion for the reader at this point)

From Quantum Mechanics we know that atoms have discrete, separated electronic levels.

Only certain (low energy) levels are populated with electrons, all other levels are empty. Light or temperature can excite electrons to higher levels, and when they relax to low energies, they emit light (e.g., a red glowing metal rod). This picture, also shown in Figure 11, is very different from the bandstructure picture that we have previously discussed.

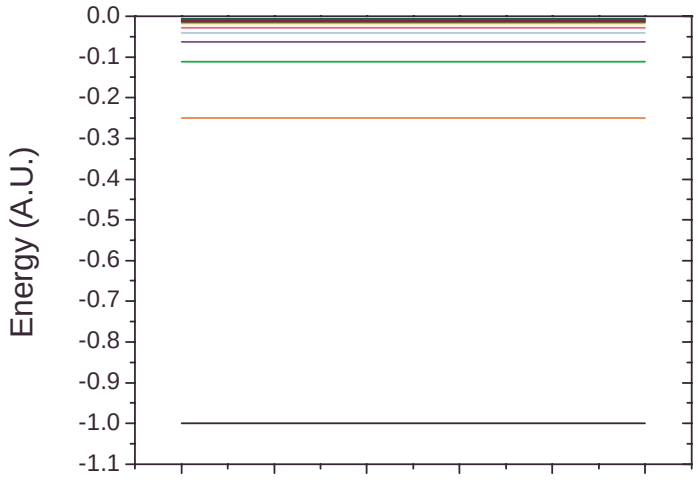

Figure 11: Schematics of the electronic levels of an atom like hydrogen.

This introduction will discuss how we get from single atoms to (semi-) conducting polymers. First of all, let's consider what will happen if two of the atoms bond to each other, i.e. form a molecule. When there is only one atom, every specific state in the atom can take two electrons at most, one with spin up, one with spin down. With two atoms together, electrons can again have one spin up and one with spin down, but it is also possible for them to both have the same spin. This is what we discussed above in the LCAO section.

Because two electrons that bind two atoms to a molecule can be in one of two states that are actually different in energy, the levels that contribute to the bond split and therefore double the states in which the high energy electrons can be. It is also clear that in above molecular bond, the up/down spin combination is actually the "binding" configuration since it is lower in energy than for two separated atoms. The up/up or down/down

configurations are called "anti-binding", since they are higher in energy than the levels in two separate atoms.

How strongly the binding and anti-binding levels are separated in energy depends on the type of bond. A regular covalent bond will separate the levels very strongly, and all the electrons will sit in the binding states. So, although we have anti-binding states that are less localized – and could therefore contribute to conduction – no electrons will be in those states. (Hence most molecules are insulators.) These bonds are typically known as sigma bonds (ref. Figure 12).

How can we get the levels closer together? Well, we have to introduce a weaker bond, i.e. were binding and anti-binding energies are closer together. One of the weakest molecular bonds is the π bond in a double bond (or even a triple bond). One bond will still be a sigma bond, but the other one will be a less strong, more delocalized pi bond (ref. Figure 12).

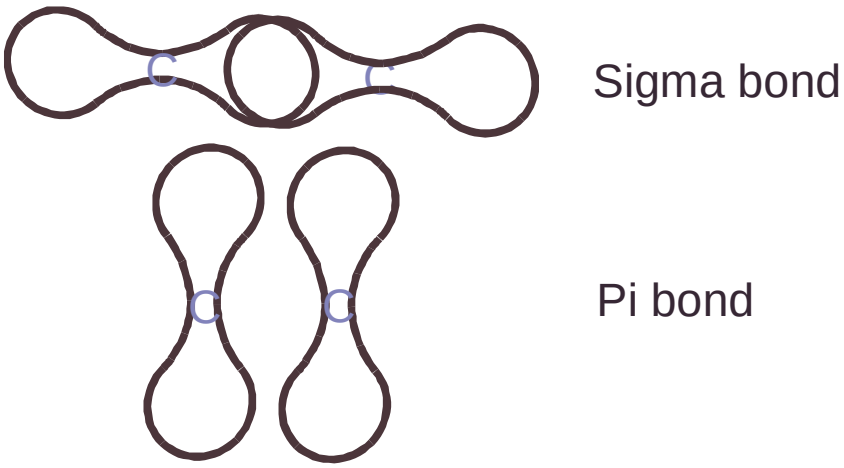

Figure 12: Illustration of the difference of p-shell sigma and pi bonds in carbon-carbon bonds.

In turns out that the best delocalisation is achieved by having alternating a single bond and a double bond between carbon atoms (although semiconducting bonds are not limited to C-C bonds). In this case, bringing together more and more atoms to one molecule, the levels will split up but will stay close in energy. This is called "conjugation", and the "conjugation length" determines how many bonds in a row we have that are alternating single and double bonds. This will have a great significance in our discussion.

We can easily imagine that if we build a string of more and more atoms, we will get more and more levels, always split in binding and anti-binding levels. This is depicted in Figure 13, where from left to right we introduce more and more bonds and atoms into the molecule.

We see that apart from having more and more levels, the levels also get closer and closer together. If we imagine taking the process started in Figure VII-4 to infinity, it would seem

that the levels completely overlap and we would recover a bandstructure as previously discussed.

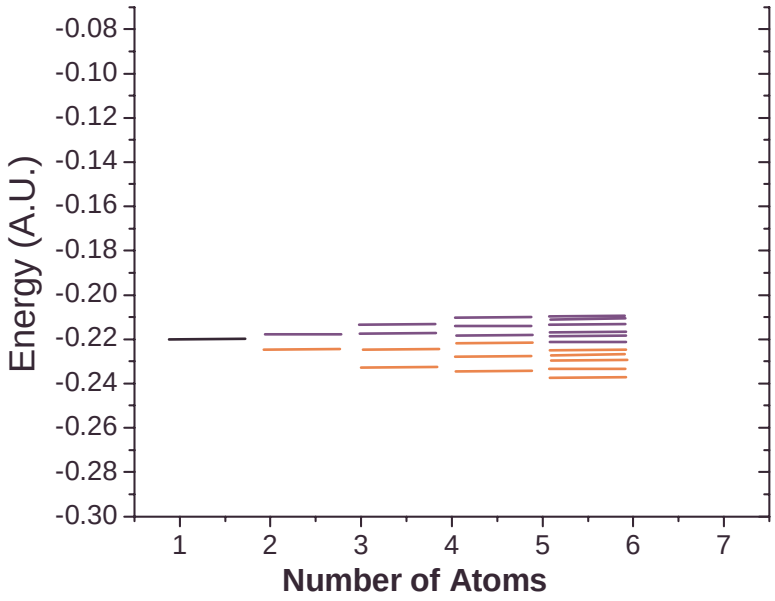

Figure 13: Electronic level going from one to many atoms

To summarize, for a small molecule, we have completely discrete energy levels, and for infinitely long molecules we recover band structures (with a small bandgap if there are pi bonds, large bandgap if there are only sigma bonds).

However, it is very difficult to synthesize long chain molecules – polymers – without introducing any defects. So, we still need to discuss what happens when there are defects and what happens if we really do just have short chains.

Let's start with a more thorough definition of polymers and oligomers. Both are put together from many so-called monomers, or simply repetition units. A monomer is the building block for strands of oligo- or polymers. It is a small unit that is repeated many times. An example (PVC – polyvinyl chloride) is shown in Figure 14. Other examples are shown in Figure 15.

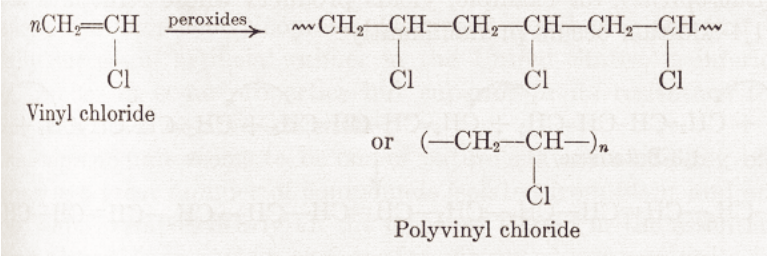

Figure 14: Polymerization of Polyvinyl chloride

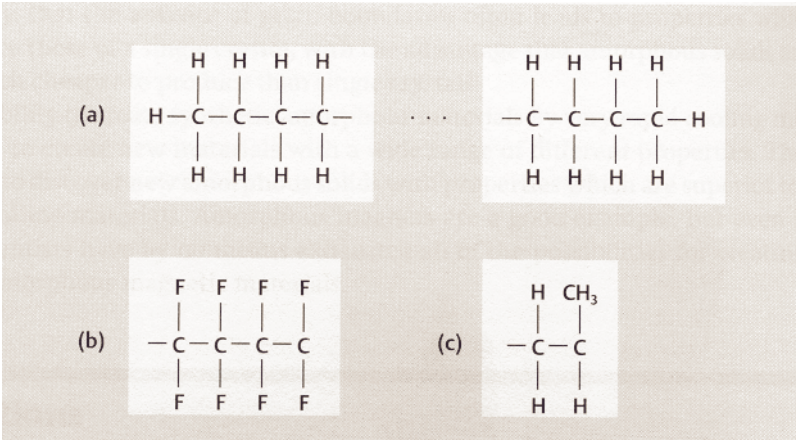

Figure 15: Examples of polymers and their endgroups
(a) shows a Polyethylene molecule, the monomer unit is CH2, the end unit is CH3, **(b)** shows part of a polytetrafluoroethylene, and **(c)** is a polypropylene monomer unit.

So, the number of repeated monomer units determines the electronic characteristics, and we call the resulting molecule a monomer (one repetition unit), an oligomer (more than two repetition units and less repetition units than xxx, where xxx is a really fuzzy number), or a polymer.

The line between an oligomer and a polymer is not well defined. Long undisturbed chains of perfect repetition are rare, so very often we count a molecule to be a polymer already with 15 repetition units. We will see that for the case of a (semi-) conducting polymer there is a much better way of defining the borderline, namely, how many repetition units does it take for there to not be much of a change in the electronic properties by adding another monomer unit.

How can this be understood? Well, from introductory Quantum Mechanics (I will not repeat the calculation here, I will just treat the most important part), we can determine the solution 1-D particle in a box problem, and we will see that there is some significance in it for our problem.

In this problem, we assume we have an infinitely extended 1-D space that has a potential energy of zero. In this space, around the origin ($x = 0$) we introduce a rectangular potential with the energy depth -*U*. This is shown in Figure 16 for different box sizes:

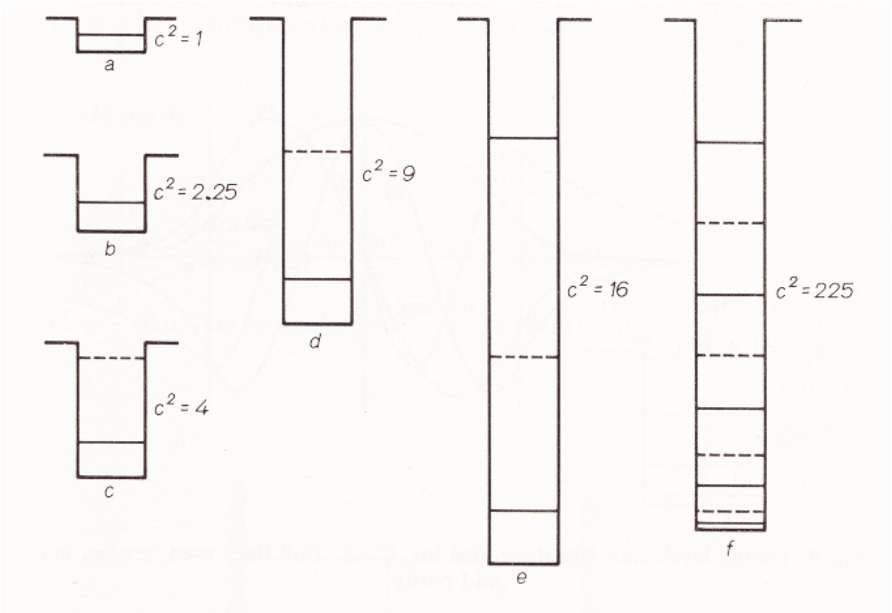

Figure 16: Particle in a box.
C denotes the width of the box (unfortunately not shown in this image), we see that as C gets larger, the box gets deeper, until the lowest energy is finally the potential -*U*.

This problem simplifies a lot if we just assume that the potential -*U* is equal to -∞. We further rescale the energy so that the bottom of the box is at energy 0, and the borders go to +∞. In such a case, the particle (represented by a sinusoidal wave in the simplest case) can only be inside the box. As such, the amplitude at the borders has to be zero (otherwise the derivatives at this point would not be smooth). The wavelength for a standing wave is very simple:

$$\lambda_n = \frac{2L}{n}, \tag{2-8}$$

where: λ_n *is the wavelength of the* n^{th} *state,* L *is the length of the 1-D box.*

Using the de Broglie relation between momentum and wavelength

$$p_n = h/\lambda_n, \tag{2-9}$$

where: p_n *is the momentum of the particle in the* n^{th} *state, and* h *is Planck's constant.*

we can calculate the kinetic energy as follows:

$$E_n = \frac{p_n^2}{2m} = \frac{\left(h/\lambda_n\right)^2}{2m} = \frac{n^2h^2}{8mL^2}. \tag{2-10}$$

We see that for n=1, we get the lowest energy (the so called ground state energy).

Also, it is obvious that as L approaches ∞, the ground state energy approaches zero, which is exactly the energy of the potential after we rescaled the energy axis. The wavefunctions are shown in Figure 17. In general, we prefer bound states to have negative energies, and the potential not to be negative infinity. The calculation is a little bit more complicated, so here is just the result:

$$E_n = -U\left(1 - \frac{n^2h^2}{8mL^2}\right). \tag{2-11}$$

We see that as we make the box infinitely large, we always recover with the potential energy of the box, and as the box gets smaller and smaller, the energies get higher and higher. The proportionality is $E_n \propto L^{-2}$.

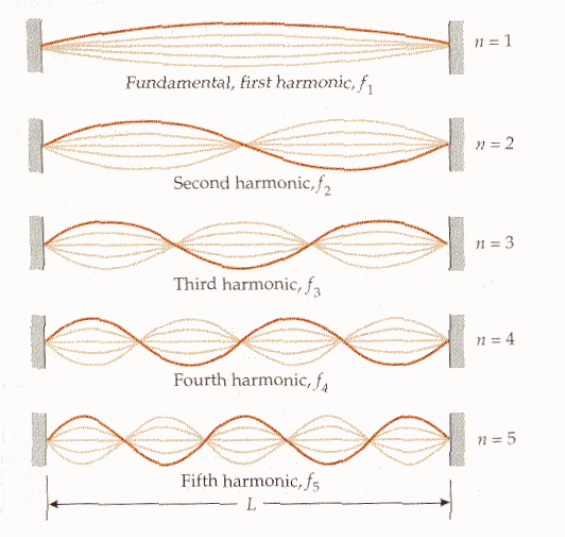

Figure 17: Standing waves – the particles in the infinitely deep box.

In this first approximation for our problem of an increasingly long chain, we see that the difference in energy between 5 and 6 repetition units will still be relatively big, whereas the energy difference between 100 and 101 is small. If the difference between two chains of

length and length+1 is very small, then the length does not matter so much anymore, and we can assume it is a polymer.

However, there were a lot of assumptions made in this estimation (1-D, rectangular continuous potential, no adjacent chains) and Equation (6-11) in fact does not hold. It has been shown in several papers, the for conjugated oligomers and polymers, the dependence of the energy with the chain length is in fact (see also Figure 18),:

$$E_n = const - \frac{const}{n_{rep}}, \tag{2-12}$$

where E_n *is the energy for n repetition units,* n_{rep} *is the number of repetition units.*

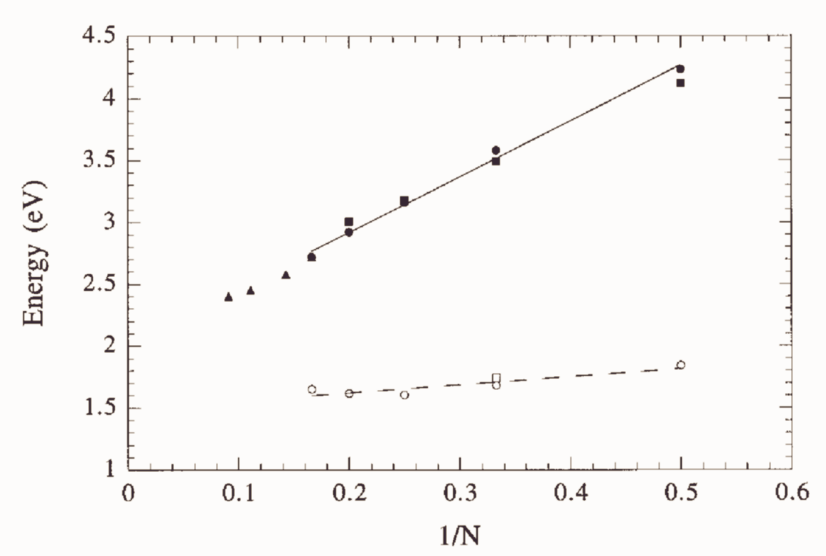

Figure 18: Dependence of the bandgap energy with the chain length.
Comparison between the bandgap energy change with the inverse number of thiophene rings, 1/n, of (i) the INDO/MRD-CI singlet-triplet S0 ⇒ S1 (solid line, closed circles) and singlet-triplet S0 ⇒ T1 (dashed line, open circles) energies and (ii) the experimental S0 ⇒ S1 (closed squares, closed triangles and S0 ⇒ T1 (open squares) energies obtained from measurements in solution. [6]

We see that oligomers mith more than 20 repetition units do not vary the bandgap energy strongly with respect to each other, and in fact that is a very good border at which to define the intersection between polymers and oligomers. However, since very often defects delimit the number of actual "pure, undisturbed" repetition units – we will discuss this in more

detail below – very often the transition from oligomers to polymers is set for ten repetition units.

2.2 Band Diagrams

(A note from the author: This section is taken from my second guest lecture at the 2001 summer workshop at BGSU. I originally intended to write it completely new, but I realized that the explanation of the different electronic junctions with examples of device applications is actually quite intuitive.)

The term band describes an infinite multitude of states (places where electrons can be located) that are close together in energy, so that they can be regarded as a continuous energy band, in which electrons can be located anywhere.

A "Valence Band" is a band in which electrons are localized around one atom. It is the last band that is entirely filled with electrons. Thus, if an electron wants to move to a different state, the electron has to exchange places with another one, since there are no empty states. Since there is no "net" movement (electrons are indiscernible), no current flows. A "Conduction Band" is a band in which electrons are delocalized (not closely bound to an atom) so that they can move around relatively freely to any adjacent unoccupied states. A conduction band is either empty or partially filled. Thus, there are empty states and a "net" movement of electrons is possible.

The simplistic picture of a bandstructure for the three different types of conductors is shown below in Figure 19 and Figure 20:

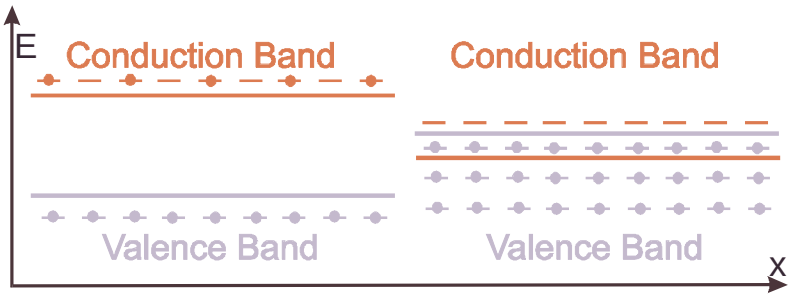

Figure 19: The bandstructure of metals:
The left picture signifies a metal where the conduction band is separated from the valence band, but partially filled. The right picture shows a metal where an empty conduction band overlaps with a valence band. The two cases are macroscopically identical.

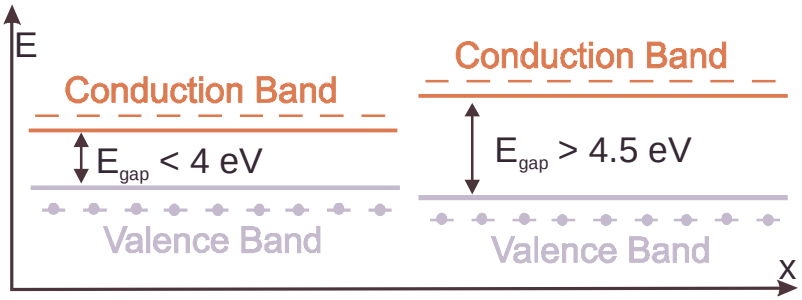

Figure 20: The bandstructure of semiconductors and insulators: In both cases, the conduction band is empty and the valence band is filled. The left picture shows a semiconductor, and since the energetic difference between the states in the conduction band and the valence band are relatively close so that some electrons in the valences band are excited into the conduction band. The conductivity at room temperature is much worse than that of metals – hence the name "semiconductor". The energetic gap between the two bands in the case of an insulator (right picture) is too large to allow any significant amount of conductivity. (The exact borderline between semiconductors and insulators is not perfectly defined; the values in the figure are guidelines)

The energy difference between the conduction band and the valence band can be overcome by many sources: thermal energy (T = 300K, room temperature is equivalent to 0.025 eV), photonic energy (light, X-rays, gamma rays), and incident particles, i.e. protons, neutrons, electrons. The closer the difference between the provided and the required energy is, the higher is the chance that a transition from a lower band to a higher band occurs. Being in a higher state (an "excited" state) is unfavorable for the electron, and it will "relax" into a lower state after a certain "lifetime".

It should just be noted at this point that the "lack" of an electron in the valence band contributes to the conductivity as well. It should be seen as the remaining electrons having a place to go to. The process is largely equivalent to an electron in the conduction band, but the "ease" with which they move in the respective bands may be different. In some semiconductors the "lack of electron" in the valence band has a higher mobility then the electron in the conduction band, and in some semiconductors the reverse is true. The "lack of an electron" is typically called defect-electron or hole. An electron carries a charge of negative $1.6\ 10^{-19}$ Coulomb, the lack of an electron, a hole, carries a charge of positive $1.6\ 10^{-19}$ Coulomb. Electrons and holes are summarized with the term charge carriers.

The remainder of this section will describe different electronic junctions in semiconductor devices, exemplary for the type of photodetectors they are used in. The basic principle of any photodetector is that it converts light into electricity, and typically (though not always) the current response is measured. When we discuss the different types of detectors, there are a couple of terms that will be important to describe the dissimilarities.

2.2.1 Undoped, single layer band schemes (application: photodetectors)

A photoconductor is the simplest photodetector imaginable. It basically consists of a piece of semiconductor with two electrodes. The choice of semiconductor will determine for which wavelength (= color) the detector will be most responsive. Germanium (Ge) will give infrared sensitivity, Silicon (Si) will respond most to red light, Cadmium Sulfide (CdS) will detect in the green, and Gallium Nitride (GaN) in the blue. The distance between the two electrodes will determine both response time and gain, if the electrodes are close together, the response time will go down and the gain will go up. For photoconductors, the gain can vary from 1 to 1 million, and the response time can vary from 10 nanosenconds (ns) to 1 millisecond (ms).

The basic working principle of the photoconductor is simple. When there is no light, the number of carriers in the valence and conduction bands is very low and there is no current. With incident light, charge carriers are created in the valence and conduction band, and the conductivity can increase over several orders of magnitude. An externally applied electrical field will invoke a higher current under illumination, which allows the detection and measurement of the incident photon flux.

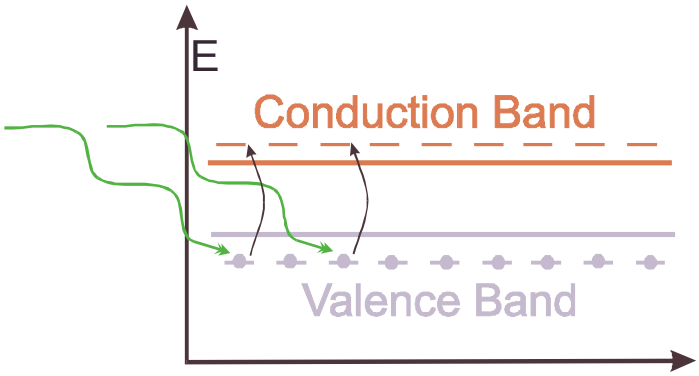

Figure 21: Photoconductor under illumination:
The green arrows show photons with enough energy to lift electrons from the valence band into the conduction band. The black arrows show that the two electrons from the valence band will have enough energy after the absorption of the respective photon to be in the conduction band.

With electrons in the conduction band and defect-electrons in the valence band, the conductivity is now substantial. Furthermore, the conductivity will depend directly on the number of absorbed photons, so it makes both a qualitative and quantitative analysis of the incident light beam possible.

The response of the detector is in form of a current under an external bias – a certain number of electrons passing per second (this is the definition of current). It should be noted

that for a photoconductor an applied external voltage is necessary to extract the photocurrent. Without an applied voltage, the conductivity is still increased, but no current flows and, hence, the absorbed photons are not detected.

For a constant applied external voltage, the current depends linearly on the number of absorbed photons.

2.2.2 Organic single layer and two layer semiconductor devices

In many current device applications, the organic layers are intrinsic, and the bands will look similar to the ones discussed in 2.2.1 – the band schematics of doped semiconductor devices will be analyzed in the upcoming sections. The limitations of that approach are that the hole and electron carrier concentrations are lower, which affects the conductivity in general. Also, the applied field drops over the whole area, unlike it is the case for doped device junctions discussed below.

Due to the fact that in organic semiconductors the electron/hole pairs (excitons, discussed in 2.3.2 on page 32) have a much higher binding energy than in their inorganic counterparts, the charge separation in the case of a single layer device as shown in Figure 22, top, is not very efficient. The tightly bound electron/hole pair is neutral macroscopically and therefore does not dissociate in weak electric fields.

Two layer devices, on the other hand, feature an interface between two organic semiconductors with different workfunctions/HOMOs and electron affinities/LUMOs, and therefore at the interface the electron/hole pair will readily dissociate. Using interdiffusion or lamination processes, the interface area can be extended and the charge separation process enhanced.

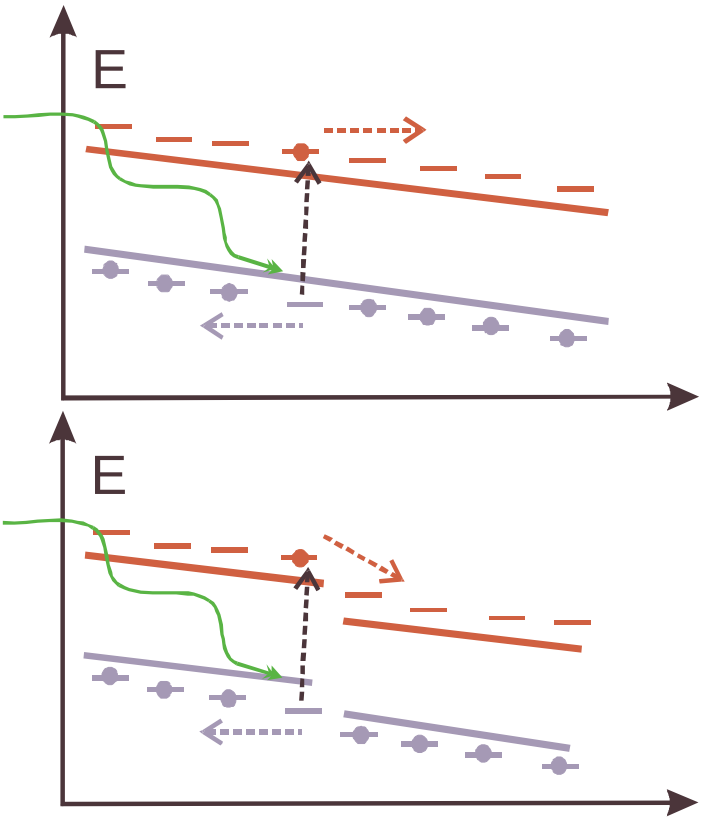

Figure 22: Band schematics for organic semiconductor devices. Above: Single layer organic device. An external applied field tilts the conduction and valence band in the entire device. The local fields are therefore often not sufficient to separate the electron/hole pair. Below: Two layer organic device. When two different materials are layered on top of each other, one material will have a stronger affinity for electrons, while the other should have a stronger affinity for holes. In this case, the electron/hole pairs are efficiently separated at the interface and are transported away in the respective direction by the applied external field.

2.2.3 P-N junctions (application: photodiode)

The restriction of the photoconductor – having to have an applied external voltage – is undesirable in some cases the require detection in a remote location without a constant access to electricity. This is possible with a photodiode.

In order to discuss the photodiode, we need to qualitatively introduce the concept of doping. Basically, doping introduces impurities near the conduction or valence band, making either more electrons available to the conduction band or less electrons (i.e. more "holes")

available to the valence band. The former case is called n-doping and the latter is called p-doping.

A simplistic picture of doping is shown below:

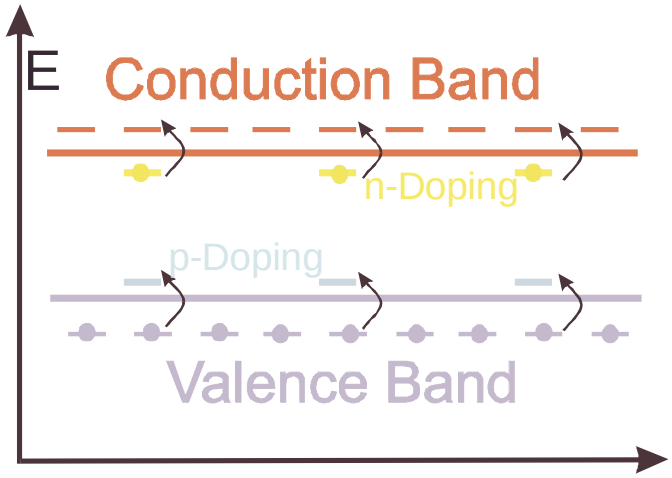

Figure 23: Doping in semiconductors.
Both p-doping and n-doping are shown in this figure, for applications only one or the other is used. The energetic difference between the doping states and the bands is so small, that thermal excitation at room temperature is enough to add electrons to the conduction band or remove electrons from the valence band, respectively.

The geometry of a photodiode is already a lot more complicated than that of a photoconductor. In the simplest case, it consists of a p-doped and an n-doped semiconductor put together. At the contact area between the two semiconductors, the "interface", the excess electrons on the on side and the lack of electrons on the other side cancel each other out. This is the so-called depletion layer. The depletion layer is the active part in the "p-n" photodiode; it is where the electron in the conduction band and the empty space left in the valence band get separated. This is illustrated in Figure 24, below.

The gain of any p-n photodiode is usually designed to be equal to one. The response time greatly depends on the thickness of the depletion layer – the smaller the depletion layer, the smaller the response time. However, since the electron-hole pairs generated by the absorption of a photon only separate in the depletion layer, a photodiode with a small depletion layer is fast, but insensitive.

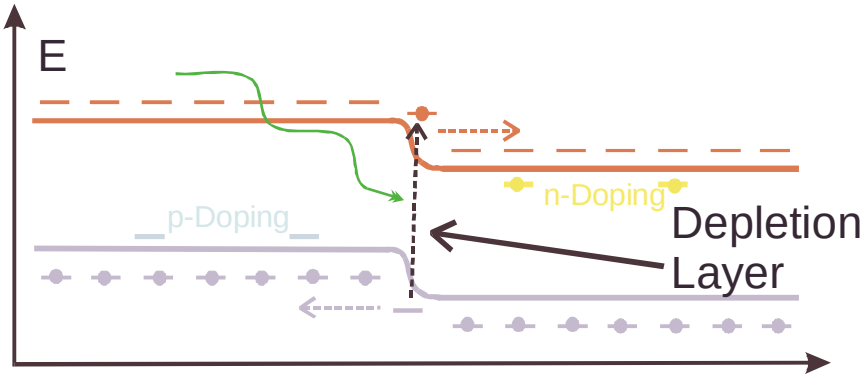

Figure 24: P-N photodetector.
A photon is absorbed near the depletion layer, and due to the high energetic difference, the electron in the conduction band and the now empty state (the hole) in the valence band separate. It should be noted that electrons fall "downwards" in energy, where as holes fall "upwards" in energy. Then, holes move to the left in the p-doped region and electrons to the right in the n-doped region until they are collected at the electrode.

2.2.4 P-I-N junctions (application: sensitive photodiodes)

The "i" in "p-i-n" stands for intrinsic, meaning that the semiconductor is neither n- nor p-doped. Thus, it is depleted of charge carriers and we can customly choose the thickness of the depletion layer. We can increase the sensitivity of the photodiode over several orders of magnitude, but sacrifice response time accordingly.

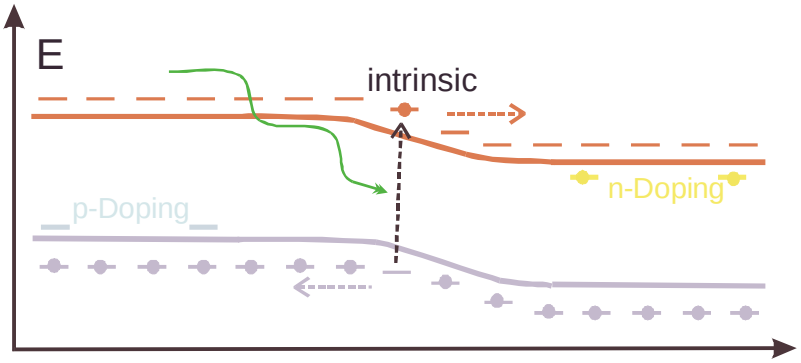

Figure 25: P-I-N photodetector: Note the larger "depleted zone" in comparison to a regular p-n photodetector

2.2.5 Metal-semiconductor junctions (application: fast photodetectors)

When a semiconductor and a metal are in direct contact, the excessive charge carriers (electrons or holes) will be drawn from the semiconductor into the metal, basically inducing a depleted zone similar to that of a p-n junction. Again, the active zone is around the junction, and the larger the junction, the higher the sensitivity of the detector. Since the electron-hole pairs need to be created near the junction for a fast response, the light has to go through the metal in this detector, and the metal electrode needs to be very thin,around 20 nm, and has to have an anti-reflection coating. This junction allows extremely fast charge separation for high speed detectors. This stems from the fact that the charge carrier generation occurs close to one electrode, which makes recombination impossible.

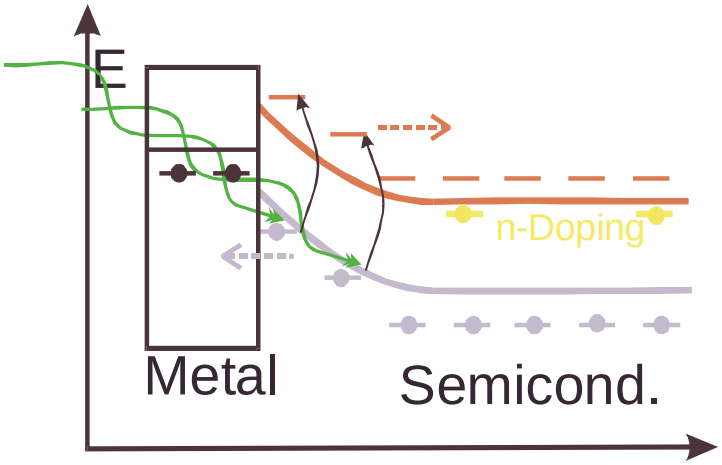

Figure 26: Metal – n-type Semiconductor Detector:
Near the metal – semiconductor interface, the n-doping of the semiconductor is removed, as the electrons are taken by the metal. In the depletion zone near at the interface, photons are absorbed. The electrons are extracted via the n-doped part of the semiconductor, and the holes are immediately removed by the metal. This allows very short response times.

The response time is 0.01 nanoseconds, as it was the case for the p-n photodiode, but the sensitivity is higher comparatively speaking.

The metal-semiconductor photodetector is used similarly to a regular photodiode and just shows an improved response, albeit it has to be more specifically for certain wavelengths to make sure that the metal electrode is mostly transparent at the chose wavelength, and also to make sure that the semiconductor shows optimum response.

2.2.6 Metal-insulator(oxide)-semiconductor junctions (application: charge accumulation detectors)

For this class of detectors, an insulating layer is inserted between the metal and the semiconductor interface. Very often, those insulating layers are metal-oxides or semiconductor-oxides. Thus, they are often called metal-oxide-semiconductor detectors, or MOS detectors. The abbreviation MIS is rarely used. Below is a figure explaining the functionality of the MOS:

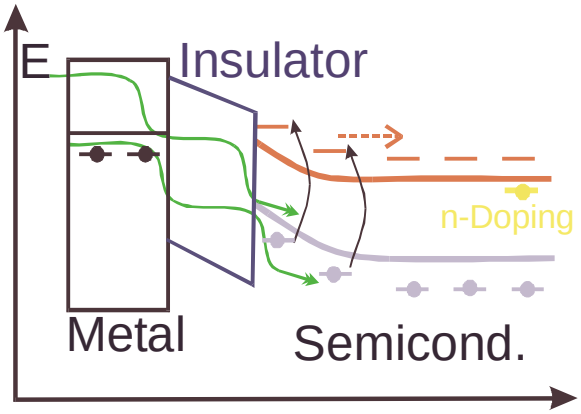

Figure 27: Metal-Oxide-Semiconductor Detector:
Shown here is an n-doped semiconductor with an interface to an insulator. The insulator is in contact with an electrode.

It has to be noted at this point that due to the insulator, this system does not conduct a current anymore, even with an applied external voltage and under illumination. The electrons (in the case of an n-doped semiconductor) are still extracted after the illumination of the semiconductor-oxide interface, but the holes stay at the insulator due to the field that stems from the external voltage. Thus, at this interface, a charge is collected – in this case a positive charge.

How can we use that to our advantage? Well, the first aspect is that we can now let the MOS "sit" in light until it has accumulated enough charge. This is good for low intensity applications that do not need fast responses. We can integrate the incoming light flow for a certain time span, until enough light has been absorbed to give us a charge packet large enough for detection. To extract the charge, a negative voltage is applied to the n-doped semiconductor ("reverse-bias"), we can extract the positive charge that has been accumulated. The negative voltage attracts the holes.

An array of MOS detectors is called a CCD, a charge coupled device. CCDs are used for digital cameras and camcorders, but also for spectrometers, like the Ocean Optics fiber spectrometer – which has been used to accumulate quite a few spectra for this thesis.

2.3 Charged and Excited Species in Semiconductors

2.3.1 Free electrons (and holes)

The following discussion discusses the "Drude" model. Electrons in the conduction band will freely diffuse when an external potential is applied. Their mobility is limited by collisions with lattice ions, the lattice potential, which screens the external potential and can be described as an effective mass, and also by so-called trap states, impurities with a high electron affinity. The average velocity of an electron in a solid is, neglecting everything but electron-lattice interactions: [7]

$$\mathbf{v}_d = -\frac{q\mathbf{F}\tau_c}{m^*}, \tag{2-13}$$

where: $\mathbf{v}_d$ *is the average drift velocity,* q *is the electron charge,* $\mathbf{F}$ *is the electric field,* τ_c *is the average free flight time between two ion-electron collisions,* m^* *is the effective mass of the electron.*

The current density can thus be written as:

$$\mathbf{j} = -nq\mathbf{v}_\mathrm{d} = \frac{nq^2\tau_s}{m^*}\mathbf{F}, \tag{2-14}$$

where: $\mathbf{j}$ *is the current density,* n *is the electron density.*

Equation (2-14) shows that the current depends on three material constants, namely the average electron free flight time, the electron density, and the effective mass. It also depends on the applied external field. It has therefore become a custom to summarize all the intrinsic factor under one term, the conductivity:

$$\sigma_e = \frac{nq^2\tau_c}{m^*}. \tag{2-15}$$

The average velocity, in turn, depends only on the average flight time and the effective mass intrinsically, and the applied field extrinsically, and thus the mobility is defined as:

$$\mu_e = \frac{q\tau_c}{m^*}. \tag{2-16}$$

The effective mass of electrons in a solid is typically up to two orders of magnitude smaller than true electron mass. Only in rare cases, e.g. the electron in conjunction with the longitudinal phonon in the indirect semiconductor Germanium, is the effective mass higher.

Equations (2-13) to (2-16) are valid for the description of hole conductivity as well, however, the minus signs in (2-13) and (2-14) are omitted. The hole conductivity is denoted as σ_h and the mobility as μ_h, whereas the density of charge carries is written as *p*. Effective

hole masses also vary between the true electron mass and a values of up to two orders of magnitude below and can either be higher or lower as the effective electron masses.

2.3.2 Excitons – bound electron/hole pairs

Due to the Coulomb force attraction between the oppositely charge electrons and holes in a semiconductor, a pair of an electron and a hole has a lower energy in the band and is localized. It is also electrically neutral, with just a dipole moment.

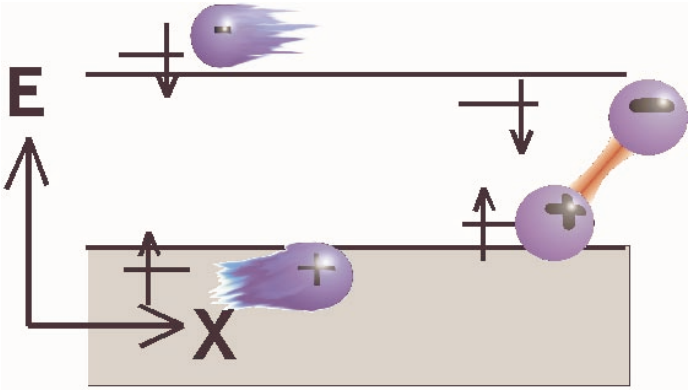

Figure 28: A comparison of free charge carrier pairs and excitons
Left side: free pair of charge carriers. The electron and the hole can move independently. Right side: Exciton lowered into the band by the coulombic binding energy.

There are actually two types of excitons:

- Wannier-Mott exciton:[8] This type of exciton extends over several lattice constants or monomer repetition units, and they are relatively weakly bound due to the Coulomb screening of the lattice and electrons in between the Wannier electron/hole pair. In fact, the binding energy of the Wannier-Mott exciton depends on the dielectric constant of the material:

$$E_n = -\frac{m^* q^4}{32(\hbar\pi\varepsilon)^2}\frac{1}{n^2}, \tag{2-17}$$

where: E_n *is the energy eigenvalue of the* n^{th} *excitonic state,* ε *is the dielectric function of the semiconductor,* n *is the excitonic eigenstate;* m^* *is the effective mass of the Wannier-Mott exciton.*

From Equation (6-17) it can also be seen that Wannier-Mott excitons have several discrete levels like a hydrogen atom, which can be spectroscopically verified for optically active semiconductors. In the case of inorganic semiconductors, this is by

far the most common type of excitons, only Wannier type excitons contribute to the physical properties of the semiconductor; the typical binding energies range from five to sixty meV (c.f. Table 1). This should be compared to the thermal energy at room temperature, $k_b T$ = 25 meV. Thus, at ambient temperatures, the Wannier excitons in most inorganic semiconductors are thermally dissociated or the excitonic levels are broadened too strongly for the excitonic absorption to be discernible from the regular optical absorption.[5]

- Frenkel exciton:[9] This exciton is extremely localized, basically within one unit cell of the lattice. Therefore, the attractive force between the electron/hole pair is not shielded and also involves interactions with core electrons and associated potentials. Therefore, Frenkel excitons are much harder to describe, as the complete bandstructure must be known, and the binding energies are much higher. Frenkel excitons are rarely observed in inorganic semiconductors.

Table 1: Exciton binding energies for several zinc-blende and wurtzite semiconductors.[5]

Material	GaAs	InP	CdTe	ZnTe	ZnSe	ZnS	ZnO	CdSe	CdS
Exciton binding energy /meV	4.9	5.1	11	13	20	29	59	15	27

In the case of organic semiconductors, we expect exciton binding energies to be higher than in inorganic semiconductors. First of all, the dielectric constants in organic semiconductors are lower than in inorganic materials, increasing the excitonic binding energy. Secondly, excitons in some materials may be Frenkel excitons. There have been many different claims on the actual binding energy of excitons in organic conjugated materials, ranging from around fifty meV [10] to almost one eV [11]. Typically, values around three hundred to four hundred meV are discussed to this day. [12-14] It should be noted that excitons in many organic polymeric semiconductors have not been directly observed, mainly due to the fact that inhomogeneous absorption edge broadening, excitonic features are not readily discernible from the bandgap absorption – the measured absorption spectrum is a superposition of both. Although the length of polymers can be controlled strictly today by means of chemistry, the effective conjugation length can vary due to excitations and charges on the chain, impurities, and chain – chain interactions.

Due to the specific geometries of polymeric conjugated strands, it is helpful to divide occurring excitons into two different groups:

- Intrachain excitons, electron/hole pairs on the same polymer chain within the same conjugation element. This is the most commonly expected excitonic species in polymers.[15-17]

- Charge transfer excitons, where the electron and the hole are separated on two different molecules, or two different polymeric chains with different bandgap energies, i.e. interchain excitons.[18]

Excitons can be dissociated by two different means, thermal dissociation and field induced dissociation. In inorganic semiconductors, at room temperature, most excitons are thermally dissociated at room temperature, with the exceptions of ZnS, ZnO, or similar materials. In organic materials, with binding energies ten times higher, the thermal energy required would mean exposing the organic compound to several thousand degrees Kelvin, beyond the evaporation point. This is clearly not an option, but excitons can be dissociated by fields as well. In principle, we want to tunnel the electron out of the common potential by applying an external field $F_{ext} > \frac{E_{exc}}{qr_{exc}}$. E_{exc}, the binding energy, is assumed around 0.3 – 0.4 eV for most conjugated molecules, and r_{exc}, the exciton radius, is normally on the order of 5-10 nanometers. Thus, a field of at least 0.6 x 10^6 V/cm is required for the dissociation process. If this value is just met, the dissociation will not be very effective as the tunneling probability for the electron will be low, but as that field is increased by another order of magnitude, the dissociation will be contribute significantly to the overall conductivity.

Local field distortions provide such strong electric fields. Impurities (read: traps) can lead to significant exciton dissociation, and it has been measured that the photocurrent response goes up initially during the process of photo-oxidation,[1] before the mobility is decreased more significantly. It is much more reliable though to actually introduce acceptor molecules into the system, either by blending two organic materials, or using two layers on top of each other (ref. Figure 22 on page 26). In the latter case, charge separation is very efficient,[19,20] although confined due to the interface depth. By increasing the interpenetration of the two layers, the interface depth can be increased, and efficiencies are increased as well. [21,22]

2.3.3 Polarons

Polarons are charge carriers that interact with the lattice, moving one or more of the ions in a unit cell, creating a slightly bound state in the solid. The effective mass of a polaron is higher than that of free electron, because of the added attraction, and therefore the mobility of a polaron is lower. At room temperature, polarons are not detected in inorganic semiconductors and only need to be considered for physical properties at low temperatures.

Due to the specific nature of the sp^3 hybrid bonds between carbon atoms in organic molecules with alternating single and double bonds in conjugated systems, the electronic systems is delocalized over the backbone of the polymer. Additionally, the electron cloud strongly interacts with the individual carbon bonds, which means that a charge carrier, a local distortion in the electron system of a conjugated molecule, strongly affects the charge

distribution along the backbone, and the bond lengths between the carbons with it. Additionally, the charge carrier, which is now a polaron, can push or pull electrons to form double bonds in new positions. This can result in the removal of a rotational degree of freedom of a carbon-carbon single sigma bond. This is called a quinoid structure, and occurs in the vicinity of a polaron traveling along the backbone.

The fact that there are no free charge carriers in conjugated polymers, but negative and positive polarons with much lower mobilities instead, seriously reduces the mobility in organic devices, which is usually four to six orders of magnitudes below that of inorganic semiconductors. In molecular crystals, bonds are often better planarized and cannot be compressed as much, which is part of the reason why high conductivities have been observed in such systems.[23] Polarons show distinct energy signatures, are located within the bandgap,[24] and can be quantitatively measured with photon-induced absorption (PIA).[25]

Chapter 2

Chapter 3

SPECTROSCOPY OF ORGANIC MOLECULES

Science is facts; just as houses are made of stones, so is science made of facts; but a pile of stones is not a house and a collection of facts is not necessarily science.

Henri Poincaré

3.1 Exciton dynamics analysis by CW method

3.1.1 Motivation

Exciton dynamics in organic semiconductors are of exceptional importance for the understanding any kind of active device. Diffusion, dissociation, and recombination are probably the three most important properties to understand. Since excitons are overall neutral, as explained in 2.3.2 on page 32, they cannot drift into the dissociation or recombination zone of a device. In fact, only the removal of excitons in the area of dissociation or recombination lets new excitons diffuse there. It was also explained in 2.3.2 that excitons in organic molecules are normally dissociated through high local fields, because of their high binding energies. This can occur at dopand locations or heterojunctions in the device, for blend or multilayer devices, respectively.

Radiative recombination in conjugated molecules is a very important physical property for the application of organic semiconductors. In light emitting devices, the rate of radiative recombination of charge carriers – **electroluminescence** – will give an upper limit to the emission efficiency. Non-radiative recombination processes will increase the heat produced in the device, limiting its lifetime. In photovoltaic (PV) devices, however, radiative recombination – **photoluminescence** – reduces the number of charge carriers in the system, and reduces the PV-efficiency. Thus, the performance of a conjugated molecule as an emitting or photovoltaic device can be estimated by monitoring the photoluminescence under different conditions. However, high photoluminescence yields do not always equate high electroluminescent rates in an emitting device, neither does low photoluminescence guarantee few total recombination processes and high photovoltaic efficiencies.

By controlling the film morphology, composition and thickness of devices made of conjugated molecules, the physical properties carrier mobility and lifetime can be changed. Altering these properties to suit the application emissive or photovoltaic devices can be monitored by measuring photoluminescence from devices of different composition. Being able to control the morphology and composition of these devices is not only important for the development of efficient devices. Doing this on a nanometer scale also gives insights into physical details of charge excitation and lifetimes.

Normally, the analysis of the dynamics of recombination and charge dissociation has to be done with ultra-fast spectroscopy and pump-and-probe type experiments. In this section, however, it is shown how to perform this experiment by a tricky arrangement of multiple layers of different organic molecules. This layer deposition technique is called "ionically self-assembling monolayers", short ISAMs. This technique allows for a detailed study of charge generation and charge transport properties. Since the ISAM process allows us to build layers with nanometer scale control, changes in dynamic effects like exciton diffusion and charge generation from excitons can be achieved through layer control. These changes can simply be monitored through cw photoluminescence experiments, which are much easier to perform than time-resolved photoluminescence measurements.

There are many fundamental research efforts going into the understanding of charge generation and transport properties, still, many details are unclear to date. Recent publications cover the area from semiconductor theory to processing and engineering methods.[26-29] It is relatively undisputed in the field of organic semiconductors that an absorbed photon results in the formation of an exciton, an assumption that I will use henceforward.

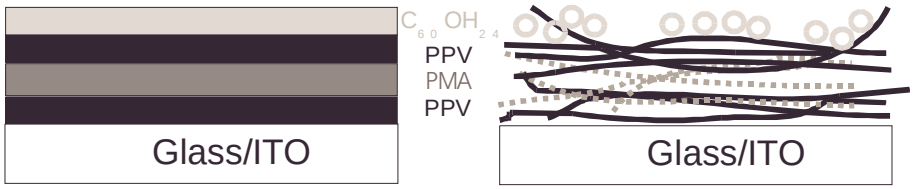

Figure 29: Layer structure of semiconductor films deposited using the ISAM method.
In this figure, PPV (black - solid thick black lines), PMA (dark gray - dotted thick grey lines), and C60(OH)24 (light gray circles) are shown as an example. This corresponds to sample 3 in Table 1 below. On the left the layers are depicted as clearly distinct and separated. In such a case, conduction would be impossible due to the insulating character of PMA. The picture on the right shows a more realistic image of the sample (as it is really deposited), the layers are actually interpenetrating[30], thus making conduction possible.

In this paper, devices composed of the following materials were studied: Poly-(para-phenylene-vinylene) (PPV), Poly-(methacrylic acid) (PMA), $C_{60}(OH)_{24}$, and copper

phthalocyanine tetrasulfonic acid (CuPC). Multi-layer devices with the following compositions of the organic layers were fabricated: PPV – { PMA / $C_{60}(OH)_{24}$ } and PPV – { PMA / Cu-PC}. The relative concentrations of the two respective materials in the curly brackets vary. These layers were created using an ISAM process to allow donor molecules (PPV) and acceptor molecules (CuPC, $C_{60}(OH)_{24}$) to lie adjacent to each other (ref. Figure 1). They were deposited on glass substrates with indium tin oxide (ITO) on top. ITO is an indium doped metal oxide, transparent in the visible region and conductive.

A PPV spincast single layer photovoltaic device[31] performs almost identically to a PPV–PMA ISAM device[32] of similar thickness made from the same precursor and converted in high vacuum at 300 Celsius, and the latter can thus be used as a reference to standard device forming methods. PMA is an insulator and is non-absorbing in the visible region. In thin layers, it also does not inhibit charge transport processes between the PPV chains, since these layers are not strictly separated by the PMA, but interpenetrating.[30] PMA is used in "pure" PPV devices to form negative counter-ions for the positive PPV-precursor solution on the substrate, otherwise only one PPV-precursor layer could be deposited. The term "pure" therefore means that PPV is exclusively responsible for absorption, charge generation and transport.

By replacing some PMA layers with $C_{60}(OH)_{24}$ or CuPC, a very efficient charge transfer of electrons from PPV molecules to the electron acceptors is introduced, resulting in a high exciton dissociation rate. This corresponds to a reduced photoluminescence via a decreased number of singlet excitons due to the enhanced charge generation. By studying the changes in photoluminescence and photocurrent, insights on the time scale of the energy transfer processes (Förster and Dexter)[33] can be gained.

3.1.2 ISAM device processing

The ISAM deposition technique is a special way of applying sub-nano to ten nanometer thick individual layers. This is achieved by alternately dipping a slightly (negatively) charged substrate into cationic and anionic solutions, repeatedly. The substrate for photovoltaic devices is typically glass, covered by indium tin oxide (ITO). ITO is a conducting metal oxide and acts as a transparent electrode. The substrate is then dipped into a cationic solution, consisting of a molecule or polymer dissolved, using acids and salts to adjust the pH and the ionic strength. The positively charged cations attach themselves onto the negatively charged substrate. The two parameters of pH and ionic strength play an important role in altering the conformation of cations and anions and the coiling of poly –anions/–cations , changing the morphology and thickness of the monolayer. Thus, the parameters have to be chosen very carefully and monitored closely. Then, it is dipped into an anionic solution, in which the negative anions attach to the previously deposited cations. This process is repeated until the desired film thickness is achieved. Initially, this technique was used by Decher[34,35] and further refined and applied by Rubner[36,37] and others.[38,39]

The following materials were used for device production:

Poly-(para-phenylene vinylene) (PPV):

Deposited as precursor using the Wessling (thiophene) precursor,[40,41] converted at 300 Celsius under vacuum. The heating ramp was very slow, allowing all residual water to slowly evaporate. This is done so that the film morphology is not altered by vapor. The structure is shown in Figure 30.

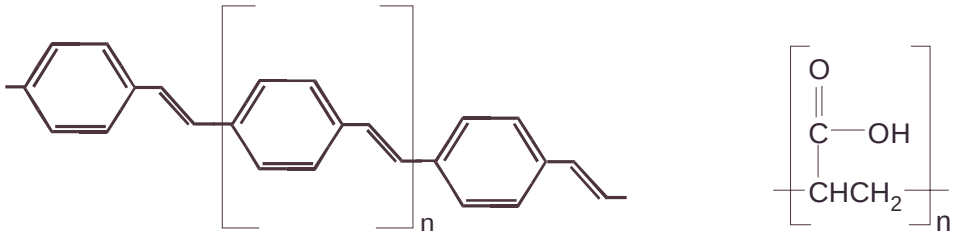

Figure 30: Chemical structures of PPV (left) and PMA (right)

Poly-(Metacrylic Acid) (PMA):

The structure is shown in Figure 30. PMA was purchased from Aldrich and processed from an aqueous solution

$C_{60}(OH)_{24}$:

With the attachment of 24 OH groups to a fullerene entity, C60 becomes highly soluble in water. For the structure, refer to Figure 31. The molecule was purchased from MER Corporation in Tucson, AZ.

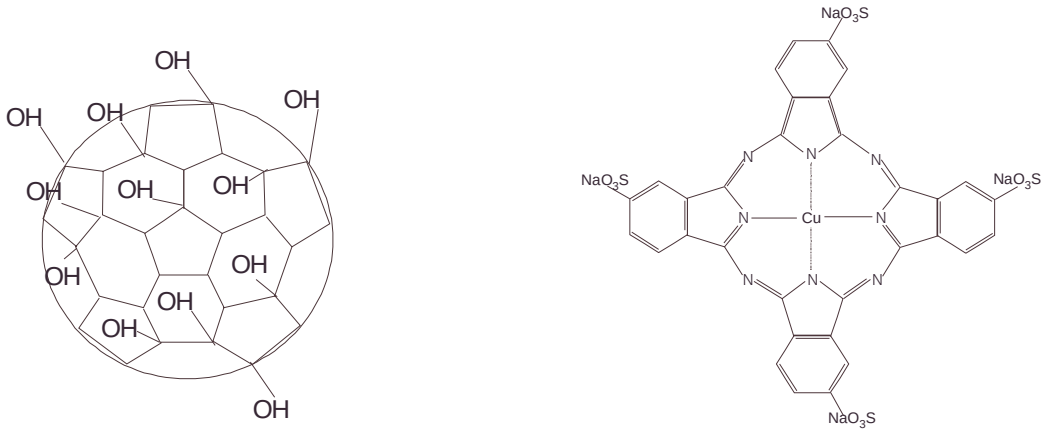

Figure 31: Chemical structure of $C_{60}(OH)_{24}$ (left) and CuPC (right)

Copper-phthalocyanine - CuPC:

Cu-Phthalocyanine tetrasulfonic acid tetrasodium salt was purchased from Aldrich.

After the deposition of the final layer, aluminum is evaporated as the second electrode to build the device. The pH and salt concentration for the devices presented in this paper were held constant as follows:

PPV precursor concentration in the dipping solution was 10mM. The pH was 4.5 and the molarity of the NaCl was 0.3 M. The PMA dipping was done with a concentration of 10 mM, pH=2.5, 0.1 M NaCl. The CuPC dipping solution was prepared as follows: 10mM, pH 3.5, for $C_{60}(OH)_{24}$: 10mM, pH 3.5, respectively.

All films were deposited from aqueous solution. Solubility in water was achieved either by using precursor polymers or by using molecules with solubility enhancing side groups.

3.1.3 Experimental

The ISAM devices as discussed above were excited through the glass/ITO substrate with the emission of 150 W Xenon lamp passed through a CVI CM110 monochromator. The emitted photoluminescence spectra were collected with an Ocean Optics spectrometer through a 20 μm optical fiber in reflection geometry. I.e., the fiber was placed on the same side of the device as the excitation beam from the monochromator. Although the emission spectra were collected for several excitation wavelengths, only the ones for a 375 nm are presented, as they showed the maximum emission intensity. The shape of the spectra was identical.

The reflection and transmission spectra were collected with a Filmmetrics optical fiber spectrometer and normalized for transmission and reflection to be 100 % of the incident intensity. The spliced top fiber was used for illumination and collecting the reflection spectra, the base had another fiber hookup used for collecting the transmission spectra. Thus, the two could be measured in the same spot and the same time, which is important to measure the optical density accurately.

3.1.4 Measurements and discussion

The following samples were investigated optically and through photoluminescence measurements:

Table 2: Composition of the measured samples.

Layers are not strictly divided, but interpenetrating, which means that two layers a separated by a layer b are in electrical contact with each other.

Sample:	*Composition:*	*Layer structure:*
Sample 1	$(PPV/PMA)_{32}$	ABABABAB
Sample 2	$((PPV/PMA)_3/(PPV/C_{60}(OH)_{24}))_8$	ABABABAC
Sample 3	$((PPV/PMA)/(PPV/C_{60}(OH)_{24}))_{16}$	ABA***C***ABA***C***
Sample 4	$((PPV/PMA)/(PPV/C_{60}(OH)_{24})_3)_8$	ABA***C***A***C***A***C***
Sample 5	$(PPV/C_{60}(OH)_{24})_{32}$	A***C***A***C***A***C***A***C***
Sample 6	$((PPV/PMA)/(PPV/CuPC))_{15}$	ABA***D***ABA***D***
Sample 7	$(PPV/CuPC)_{30}$	A***D***A***D***A***D***A***D***

The optical transmission and reflection spectra for $PPV/C_{60}(OH)_{24}$ films and PPV/CuPC films are depicted in Figure 32 and respectively. It is very obvious from Figure 32 (right) and Figure 33 (right) that the reflection component is not to be neglected when calculating the optical density, especially since the relative reflection is high near the absorption edge. Therefore, the following formula is used for more accurate results.

From Lambert-Beer's law:

$$\frac{I}{I_0} = 10^{-OD}, \tag{3-1}$$

where: I *is the transmitted intensity,* I_0 *is the incident intensity,* OD *is the optical density.*

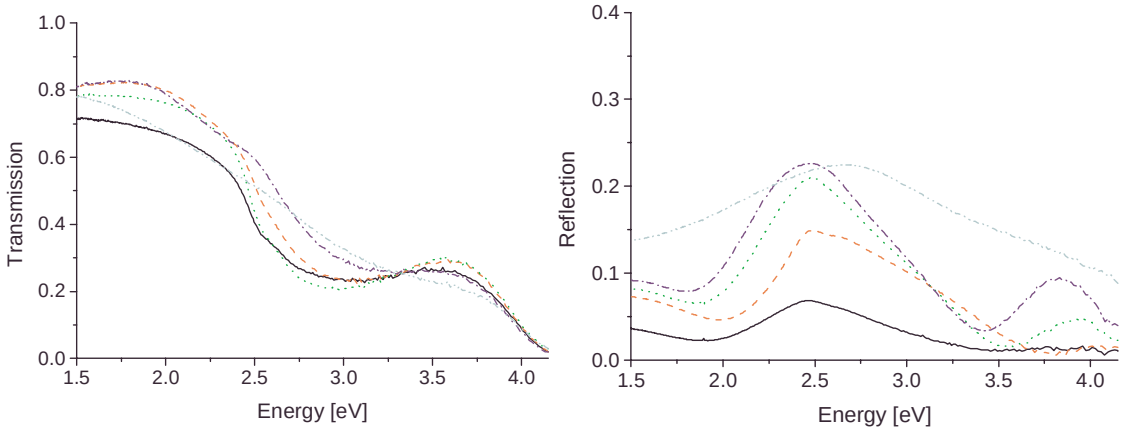

Figure 32: Transmission spectra (left) and reflection spectra (right) of $PPV/C_{60}(OH)_{24}$
Solid line: sample 1 – $(PPV/PMA)_{32}$
Dashed line: sample 2 – $((PPV/PMA)_3/(PPV/C_{60}(OH)_{24}))_8$
Dotted line: Sample 3 – $((PPV/PMA)/(PPV/C_{60}(OH)_{24}))_{16}$
Dash-dotted line: Sample 4 – $((PPV/PMA)/(PPV/C_{60}(OH)_{24})_3)_8$
Dash-dot-dotted line: Sample 5 – $(PPV/PMA)_{32}$.

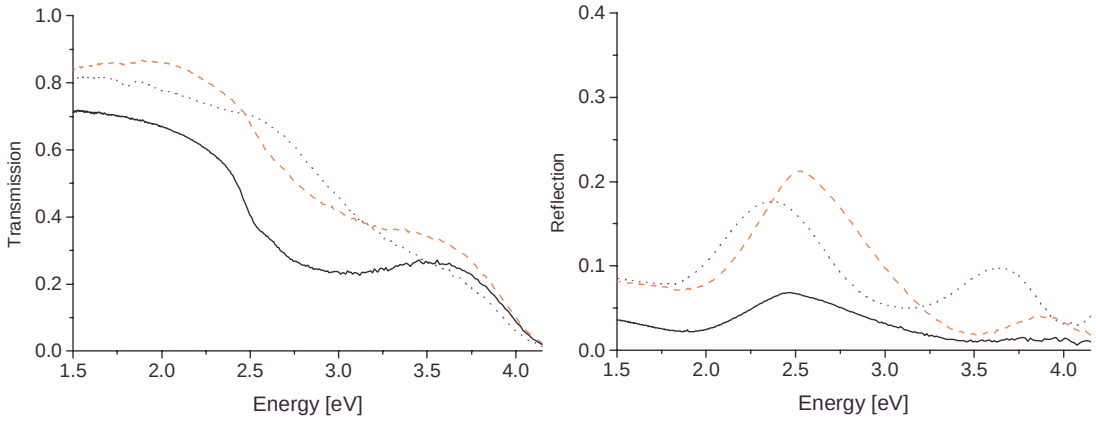

Figure 33: Transmission (left) and reflection (right) spectra of PPV/CuPC
Solid line: Sample 1 – $(PPV/PMA)_{32}$
Dashed line: Sample 6 – $((PPV/PMA)/(PPV/CuPC))_{15}$
Dotted line: Sample 7 – $(PPV/CuPC)_{30}$

The optical density is defined as,

$$OD = \alpha d \log_{10} e\,, \tag{3-2}$$

where: α *is the absorption coefficient,* d *is the thickness of the layer,* e *is Euler's number.*

A transmission spectroscopy setup typically measures the intensity passing through a sample normalized to the incident light. In general, there are three loss mechanisms for radiation through a sample – reflection, scattering, and absorption. The amount of light actually entering the sample can be described as (1-R-S), where R is the reflectivity, and S represents scattering (both normalized to the incident light, i.e. 0 < R, S < 1), respectively. In the sample, the intensity decays with Lambert-Beer's law from Equation (3-1),

$$T = \frac{(1-R-S)10^{-OD} I_0}{I_0}. \tag{3-3}$$

I_0 cancels, and the optical density *OD* can be expressed as the following (neglecting the scattering losses),

$$OD = -\log\left(\frac{T}{1-R}\right). \tag{3-4}$$

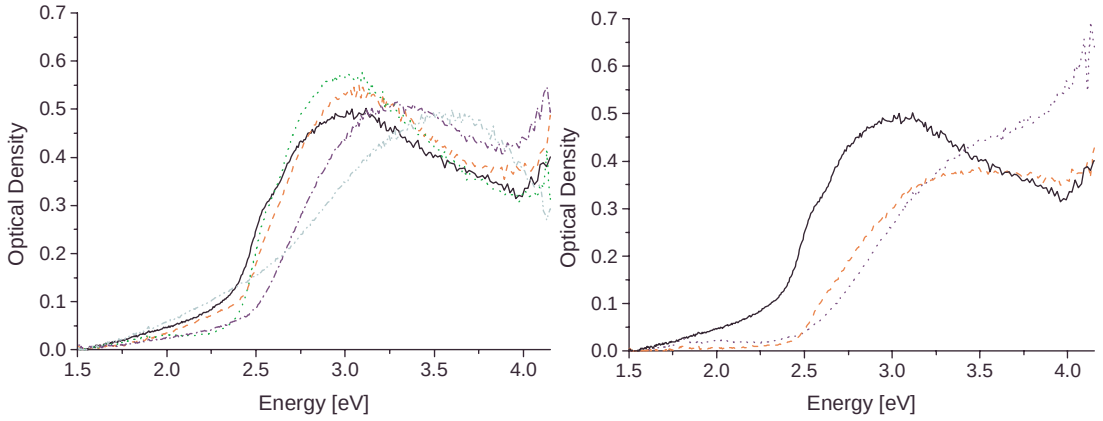

Figure 34: Optical Density of the PPV/$C_{60}(OH)_{24}$ samples (left) and the PPV/CuPC samples (right)

Solid line: Sample 1 – $(PPV/PMA)_{32}$ Sample 1 – (PPV/PMA)32
Dashed line: Sample 2 – $((PPV/PMA)_3/(PPV/C_{60}OH_{24}))_8$ Sample 6 – $((PPV/PMA)/(PPV/CuPC))_{15}$
Dotted line: Sample 3 – $((PPV/PMA)/(PPV/C_{60}OH_{24}))_{16}$ Sample 7 – $(PPV/CuPC)_{30}$
Dash-dotted line: Sample 4 – $((PPV/PMA)/(PPV/C_{60}OH_{24})_3)_8$
Dash-dot-dotted line: Sample 5 – $(PPV/PMA)_{32}$

Additionally, with the *OD* values from Figure 34, the thickness of the samples can be determined. From Equation (3-2) the relation between the optical density and the sample thickness is given. α for this batch of PPV is on the order of 1.8 10^5 cm^{-1}. The thickness of the PPV/$C_{60}(OH)_{24}$ samples is d = 6.4 10^{-6} cm or 64 nm, the thickness of the PPV-CuPC samples is d = 5.1 10 cm or 51 nm. This does not include the thickness of the PMA layers and the $C_{60}(OH)_{24}$ and CuPC layers, so the total thickness is on the order of 80 nm to 120 nm.

It can be seen from Figure 34 (left), that the PPV concentration Sample 1, 2, and 3 is the same, which is expected. For higher $C_{60}(OH)_{24}$ concentrations, the PPV content seems to change – one possible explanation is that the pH value of the $C_{60}(OH)_{24}$ solution detaches the PPV precursor film from the substrate again. Sample 6 and 7, the CuPC samples, show a lower PPV content than the PPV/$C_{60}(OH)_{24}$ samples, but the same content relative to each other.

3.3 Photoluminescence Measurements

After the absorption of a photon and the creation of an exciton, there are 4 different processes that compete with each other:

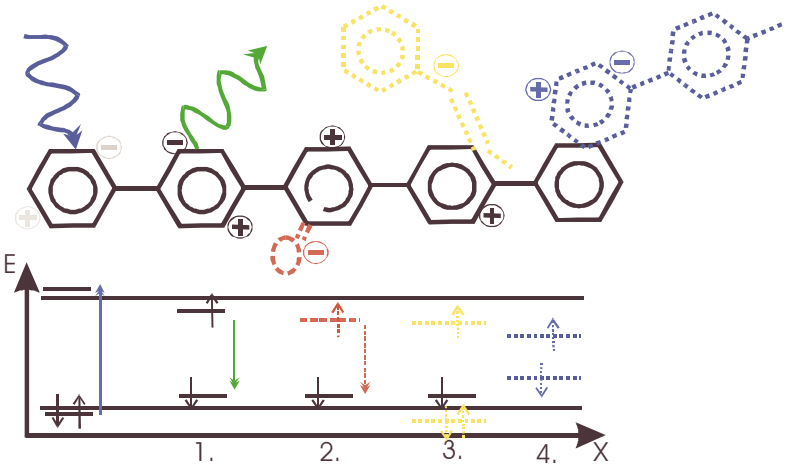

Figure 35 Competing processes in the dissociation/recombination of an exciton
1. Radiative recombination (photoluminescence), which has a distinctive lifetime for a specific material. 2. Non-radiative recombination, which is a function of the impurity of the device 3. Charge generation (dissociation of an exciton) 4. Migration (energy transfer). This only lowers the energy of the exciton, but it is conserved and can decay in one of the other three processes.

If 2 and 3 are strong, then only little photoluminescence will be seen. For non-identical molecules (e.g. PPV of different conjugation lengths) there are different energies for the emitted photons (4). Thus, migration effects can be seen as emission only from the longest conjugated molecules. Since the migration rate is higher than the radiative recombination rate, most of the emission comes from the longest molecules.

When the rate of the charge generation goes up (via introducing a guest molecule as charge acceptor):

- The PL emission intensity is lowered (the PL is "quenched"). This happens in any case.
- The PL emission is blue-shifted if the molecules have different conjugation lengths. Because not all the excitons can migrate to the longest molecules before they recombine or dissociate by processes 1, 2, and 3, less and less emission occurs on the longer chains. When the doping is high enough to prohibit all migration, only excitons absorbed by the long molecules also are emitted there. Relatively, more higher energetic excitons are emitted overall in this case.
- Finally, and strongly related to the point above, since all molecules contribute more evenly to the PL emission, the emission itself is broader. Since the 2nd effect can often be mistaken with self-absorption, the peak broadening is a much more conclusive sign of PL quenching.

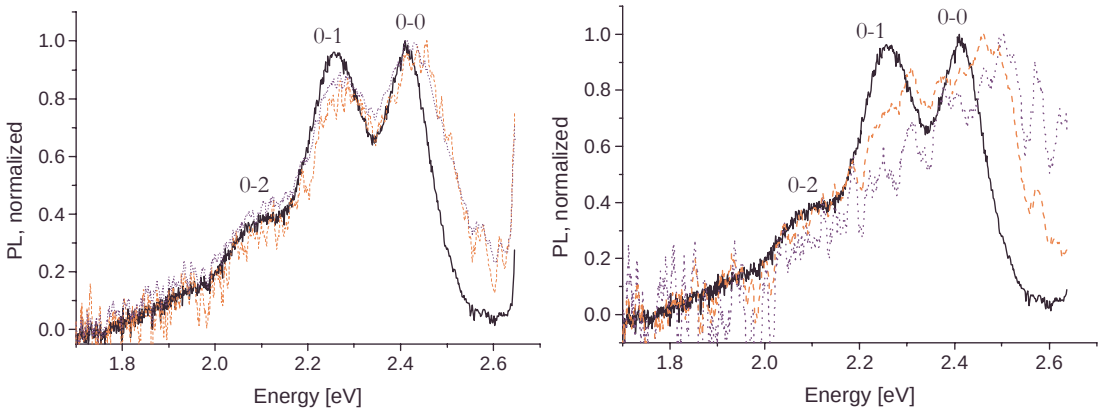

Figure 36: Photoluminescence spectra of samples 1, 2, 3 (left) and of samples 1, 6, 7 (right)

The photoluminescence spectra have been normalized to one for the 0-0 transition in PPV (2.41 eV). "0-0" stands for the direct electronic transition, which does not involve electron-phonon interactions. The "0-1", "0-2" transitions are decay processes involving the emission of one photon and one or two phonons, respectively. The relative intensities of the PL can be found in Table 2. All the PL spectra have been recorded for an excitation wavelength of 2.95 eV. The black solid line is always sample 1. In Figure 36 (left), the dotted line is sample 2, low $C_{60}(OH)_{24}$ concentration, the dashed line is sample 3, medium $C_{60}(OH)_{24}$ concentration. Figure 36 (right), the dashed line is sample 6, low CuPC concentration, the dotted line is sample 7, high CuPC concentration. All samples exhibit a blue shift and peak broadening with respect to sample 1. Sample 4 and 5 exhibit no more photoluminescence due to the high guest concentration.

From the relative PL intensities in Table 3, both $C_{60}(OH)_{24}$ and CuPC can be identified as efficient quenching guests in PPV. It is difficult to estimate the absolute efficiency of the quenching though via the emission intensities, since the exact amount of emitted light depends on the exact alignment of the sample, the concentration as well as absolute amount of the PPV, reflection losses etc. A method to evaluate and cross check the quenching results can be understood when looking at Figure 37. Polymer chains with a long effective conjugation length have a lower energy difference between the HOMO and LUMO than others with a short effective conjugation length. The chain-to-chain migration of the excited species in PPV happens on a picosecond time scale,[42] and the radiative recombination happens on the nanosecond scale, most of the emission comes from the short chains.

Table 3: Photoluminescence data for the samples 1, 2, 3, 6, 7.
The relative intensities are the 0-0 transition PL values at the peak maximum, normalized with respect to the pure PPV/PMA sample 1. The energy shift is the shift of the 0-0 peaks with respect to the 2.42 eV emission peak in sample 1. The time constant in the last column was evaluated based on our modeling of data obtained from time resolved spectroscopy[42,43] – extrapolated in Figure 38, the solid line. Due to the high errors, asymmetric error bars are necessary. The Huang Rhys Factor was determined using the peak heights, not the peak areas.

	Composition	*Relative. Inten.* ± *5%*	*Energy Shift [eV]* ± *0.01eV*	*Huang Rhys Factor*	τ *[ps]* low–**best**–high
Sample 1	$(PPV/PMA)_{32}$	100%	0.00	1.82	**1000** [42,43]
Sample 2	$((PPV/PMA)_3/(PPV/C_{60}(OH)_{24}))_8$	29%	0.02	1.69	30–**110**–350
Sample 3	$((PPV/PMA)/(PPV/(C_{60}(OH)_{24}))_{16}$	13%	0.03	1.66	7.5–**36**–130
Sample 6	$((PPV/PMA)/(PPV/CuPC))_{15}$	17%	0.04	1.67	1.8–**12**–30
Sample 7	$(PPV/CuPC)_{30}$	6%	0.05	1.60	0–**1.5**–4

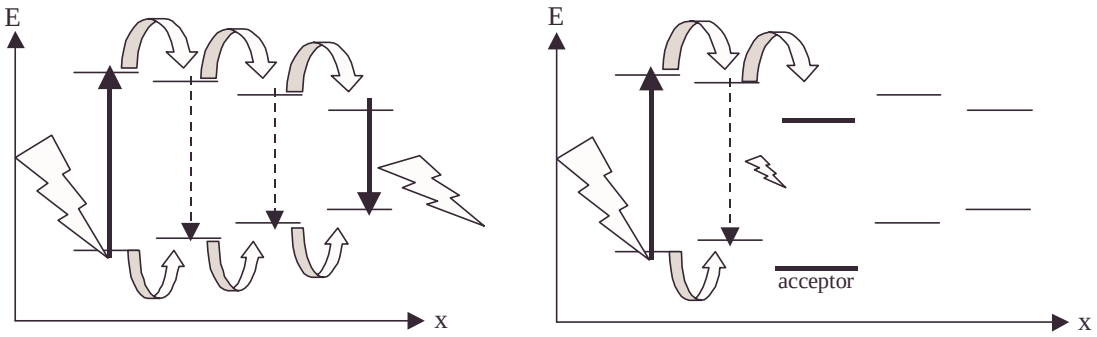

Figure 37: Migration of excitons in doped and undoped samples. Left: Exciton migration in polymers with an effective conjugation length distribution. Right: Exciton migration in a polymer when an electron transfer to an acceptor interrupts the migration.

If there is a donor or acceptor molecule near one of the short, high energy chains, the migration sequence is interrupted by a charge transfer of a hole or electron and the timescale of the PL can go down to sub ps.[44] Thus, the emission spectrum shifts to higher energies, since the excitons cannot migrate to the low energy chains anymore.[45] The result is a quenched photoluminescence, which is also shifted to higher energies (ref. Figure 37).

As mentioned above, $C_{60}(OH)_{24}$ and CuPC are basically quenching guests in PPV. Since they act as a charge acceptor for excited species created in PPV, it can be described as doping. As such, sample 1 with no quenching guests will be described as undoped sample.

From the energy shift of the PL peaks, the hopping time of the exciton can be estimated. From ultra short laser experiments, the energy shift depending on the time of emission can be quantified.[42,43] For a pure PPV film, the time scale of the radiative recombination is known to be on the order of 1 (to 1.3) nanosecond.[46] The data from [42] has been used to model and then extrapolate the strictly exponential behavior up to the lifetime of an exciton. The result is shown in Figure 38, assuming that at 1ns all the excitons have arrived at the

sites lowest in energy. We have set the energy shift to zero at the "earliest available datapoints" – see Figure 38

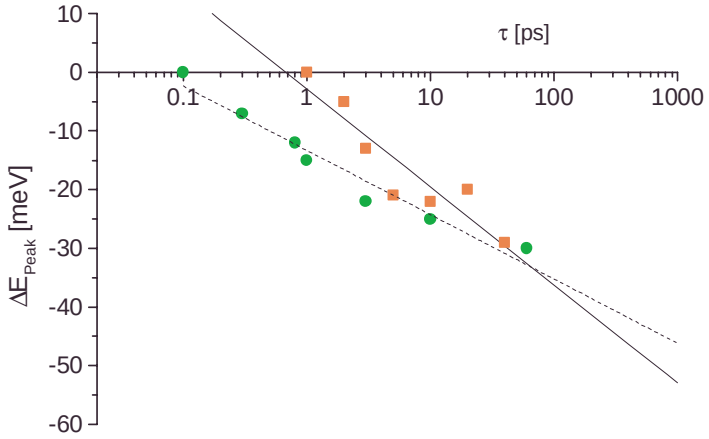

Figure 38: Extrapolated shift energy – life time relation for PPV. The datapoints marked as squares were taken from Ref.[43] the datapoints marked as circles taken from.[42] The solid line is the modeled behavior of the squares, the dotted line of the circles, respectively. In both references, the authors assumed that the energy shift was zero at the earliest measured time. The logarithmic time scale is for clarity purposes only. The linearity shows that the relaxation behavior can be described sufficiently well by an exponential behavior as described below.

The curves were fitted using a linear model for the energy shift versus the logarithm of relaxation time:

$$\Delta E = \Delta E_0 - k \log(\tau), \tag{3-5}$$

and E_0 was chosen so that the energy shift is zero for the first measured point. Its value is the energy shift at 1ps. The fit values for the datasets differ slightly due to the different time resolution of the experiments. We obtain for Ref. 43: k = 4.8 meV, E_0 = 13.3 meV; for Ref. 42: k = 2.8 meV, E_0=7.3 meV.

To determine the lifetime from the energy shift, Equation (3-5) needs to be expressed in terms of τ:

$$\tau = 10^{(\Delta E_0 - \Delta E)/k} \tag{3-6}$$

It is important to look at the error progression from the relative energy shifts. Differentiating Equation (3-5) with respect to ΔE_0 and ΔE leads to:

$$\frac{1}{\tau}\frac{\partial\tau}{\partial(\Delta E)}\log(e)=\frac{1}{k} \qquad \text{resp.:} \quad \frac{1}{\tau}\frac{\partial\tau}{\partial(\Delta E_0)}\log(e)=-\frac{1}{k} \tag{3-7}$$

If the errors are small, we can substitute the differential quotient by the difference quotient ($\delta \to \Delta$) and get:

$$\frac{\Delta\tau}{\tau}=\frac{\Delta(\Delta E_0)}{k\log(e)} \qquad \text{resp.:} \quad \frac{\Delta\tau}{\tau}=\left|-\frac{\Delta(\Delta E)}{k\log(e)}\right| \tag{3-8}$$

The error of ΔE_0 from the linear regression is small – around 0.5 meV – against the error of ΔE – 10 meV – and does not show a major contribution. Inserting an error $\Delta(\Delta E)$=10 meV and the value for k=4.8 meV, the relative error in Equation (3-8) comes out to 400%. With the minor contribution of $\Delta(\Delta E_0)$ the relative error can be specified as 400% < $\Delta\tau/\tau$ < 500%. Obviously, the error is too big to justify linearization. This can be seen in the fact that an absolute error of the shift energy in Figure 38 results in a very asymmetric error for the value of the lifetime. Table 3 and Table 4 therefore show minimum, maximum, and best values for the lifetime and any values derived from that quantity.

With the knowledge of the model curves above, we can obtain the approximate lifetime of the exciton in the doped samples via the measured shifts in energy (Table 3). Thus the diffusion radius of the exciton can be estimated with Equation (3-9), which leads to the values of the average distance between the absorption site and the dopand in the ISAM structures.

$$r_{diff} = v_{diff}\,\tau \tag{3-9}$$

The steady state undoped diffusion radius of PPV has been established to be on the order of 8nm.[47,48] However, these values highly depend on the PPV itself. A very pristine sample will show high photoluminescence yields and high lifetimes. The value of the exciton lifetime in the undoped sample is important for the calibration of the peak energy shift. The value of the exciton lifetime was taken from ref. 46.

In the literature values for the excitonic lifetime and diffusion radius are summarized for a pure PPV sample. With Equation (3-9), the diffusion velocity can be estimated to be on the order of 8 ms^{-1}. With the obtained lifetimes for the doped samples, the respective diffusion radii can be calculated. This value goes linear with the lifetime, so the asymmetric errors stay and are again expressed by low, best, and high values.

As mentioned above, the value for the exciton lifetime in the undoped sample is important for the exact estimate of the diffusion times and radii. By changing the lifetime marginally, the effects will be very visible in the short time regime.

Table 4: Average Diffusion Radius in Undoped/Doped PPV

Sample	*Composition*	τ *[ps]* low–**best**–high	r_{Diff} *[nm]* low–**best**–high	τ_{charge}*[ps] (Equation 3-10)* low–**best**–high
Sample 1	$(PPV/PMA)_{32}$	**1000**[42,43]	**8.00**[47,48]	assumed: **∞**
Sample 2	$((PPV/PMA)_3/(PPV/C_{60}(OH)_{24}))_8$	30–**110**–350	.24–**0.88**–2.80	31–**124**–539
Sample 3	$((PPV/PMA)/(PPV/C_{60}(OH)_{24}))_{16}$	7.5–**36**–130	0.06–**0.29**–1.04	7.6–**37**–149
Sample 6	$((PPV/PMA)/(PPV/CuPC))_{15}$	1.8–**12**–30	0.01–**0.096**–0.24	1.8–**12**–31
Sample 7	$(PPV/CuPC)_{30}$	0–**1.5**–4	0–**0.01**–0.03	0–**1.5**–4.0

This is why the values in Table 4 have such a high error margin – the error margin comes from not being able to characterize the exciton lifetime exactly. The relative life times and relative PL emission intensities should have roughly the same ratio between each other. This is not the case; the measured emission intensities show relatively higher ratios than the extracted lifetimes. The ratios differ by up to 50%. But even with a minimum uncertainty of 50% and a maximum uncertainty of about 400%, the decrease in lifetime shows the strong quenching effect and breakdown of exciton migration – a value for the diffusion radius of picometers does not signify the breakdown of the model. The diffusion radius has to be seen as an average value. Whereas most excitons stay on the same chain before the charge transfer (zero migration, so to speak), a few percent do migrate to the next chain before dissociating.

It has to be noted that both the relative intensities and the extrapolated lifetime show some uncertainties. It is difficult to determine absolute intensities while changing the samples, and small differences in alignments can change the emission intensity by a few percent. The samples were measured again in a 2nd series, and the results were reproducible within 10% - 15% of the original emission intensity.

The accuracy of the extraction of the lifetime from the energy shift depends highly on the estimated lifetime of an exciton in a pure PPV device. This lifetime is a function of film morphology, precursor quality, and conversion conditions. The better the film and polymer quality, the higher is the lifetime of the exciton, and the higher is the photoluminescence yield observed.

The lifetimes shown in Table 3 are effective lifetimes, which depend on the three dissociation rates for radiative recombination, non-radiative recombination, and charge generation:

$$\frac{1}{\tau_{eff}} = k_{rad} + k_{non-rad} + k_{charge} = \frac{1}{\tau_{rad}} + \frac{1}{\tau_{non-rad}} + \frac{1}{\tau_{charge}} \qquad (3\text{-}10)$$

If we assume that k_{rad} does not depend on the guest concentration (typically a good assumption), and that the same holds true for $k_{non\text{-}rad}$ (only approximately valid), the sum of

k_{rad} and $k_{non\text{-}rad}$ can be determined from Equation (3-10) - assuming that the generation rate is very low compared to the other two rates. Using that number, the generation rate can be obtained for the different guest concentrations. The results of this calculation are shown in Table 4.

A strong indication of a breakdown of exciton migration can be seen in the lack of any detectable photo-luminescence in sample 4 and sample 5, although both still exhibit a typical PPV short circuit action spectra in a photovoltaic measurement.[32] The dissociation of excitons, leading to higher photocurrent responses and lower photoluminescence yields, is a function of defect or guest concentrations in the host, as shown in ref. [49].

To determine the kind of charge or energy transfer from the host to the guest, the HOMO and LUMO levels of the two materials have to be considered. For CuPC, the HOMO, 4.8eV, and LUMO, 2.7eV, are well suited to accept charges from PPV, 5eV, 2.5eV respectively (ref. Figure 39). Since the HOMO is higher in energy and the LUMO is lower in energy, the whole exciton can transfer to the CuPC molecule, a very fast and efficient process. However, no photoluminescence signature of CuPC is seen in the spectra, which can be understood since the PL yield has been shown to be very low – since the PPV PL is already difficult to detect, the CuPC cannot be seen. The $C_{60}(OH)_{24}$ is electronically very different from C_{60}, and no HOMO and LUMO data is known for this molecule.

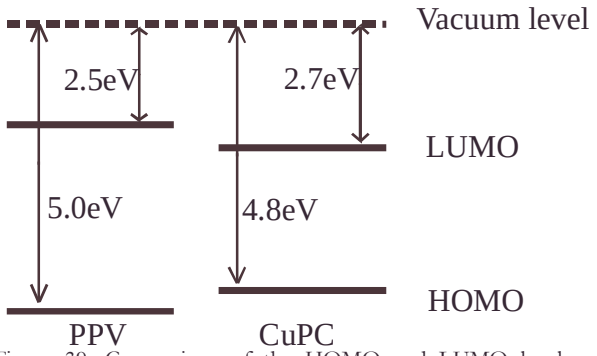

Figure 39: Comparison of the HOMO and LUMO levels of PPV[50] and CuPc[51]

In conclusion, it is seen that by tuning the layer thickness and composition of ISAM devices, the charge collection rate can be highly improved. By comparing the PL emission spectra shifts due to exciton migration in PPV, and comparing it to time resolved PL measurements in PPV, the average lifetime of excitons can be established. This number allows us to determine what the rate of exciton dissociation in different layer structures is, and gives us the possibility to study charge collection efficiencies in ISAM devices without seeing the influence of the charge extraction efficiencies measured by photocurrent measurements, which also depend on the layer structure.

3.2 Exciton Quenching Rate Analyzed by Two Photon Spectroscopy

3.2.1 Motivation for Measuring Exciton Quenching Rates in Luminescent Polymers

In the previous sections, we had discussed how the film morphology affects the exciton dissociation rates. We had also assumed that the rates of non-radiative and radiative recombination were constant for the films, noting that although not 100% correct, it is a good approximation. However, in luminescent devices, the rate of exciton dissociation / charge generation has to be very low or zero, because it is the one competitive process to radiative recombination that can be controlled. This can be achieved by depositing high quality films with low impurity concentrations. In that case, non-radiative recombination becomes the most competitive process to radiative recombination.

In general, photoluminescence efficiency is only one of many factors influencing the efficiency of electroluminescent devices. Photoluminescence quantum yields (PLQY) in molecular films can be as high as 90% and more, however other factors that will reduce the effienciency of the OLED are: injection efficiencies,[52] spin statistics,[53] the balancing of the electron and hole current, and optical outcoupling[54] of the device. Film morphology can affect the PLQY, as can interchain exciton-exciton interaction for polymeric films. But even excitons on the same chain can induce non-radiative recombination – intrachain exciton quenching. This happens only at high excitation rates, which is an important range for organic laser materials. Although interchain exciton-exciton interactions have been studied in the literature,[74] intrachain exciton-exciton interactions have not been analyzed for most organic luminescent materials.

Two of the most promising luminescent polymers, especially in light of possible blue organic light emitting devices (OLEDs), are polyfluorene (PFO) [55-57] and methyl-substituted ladder-type poly(*para*-phenylene) (mLPPP),[58-60] both synthesized with the focus on high photoluminescence quantum yields. PFO has a repetition unit of two phenyl rings planarized by a ladder-type bond. Two adjacent repetition units, however, can rotate with respect to each other (see Fig. 1(a)). As a consequence, its electronic character can be varied in the bulk and it has been noted that symmetries can be broken or established by simple film forming techniques.[61,62] The other polymer, mLPPP has a similar structure built of benzene rings, which are, however, connected with a ladder-type bond. The entire backbone is planarized providing the material with unique absorption and emission properties, most notably the subtle Stokes shift (ref. Fig. 1(b)).[63] In addition, due to the fast radiative recombination properties,[64] mLPPP possesses the potential for non-linear optics (NLO) and fast upconversion applications.

In order to determine the suitability for NLO applications, like upconversion lasers, fluorescence imaging, or volumetric holographic memories, the specific properties have to be measured and compared with the application requirements. Thus far, two-photon absorption coefficients have been measured either directly through transmission

experiments[65] or through z-scan measurements[66], where it has been suggested, that z-scan measurements deliver more reliable results. However, the emission properties due to the two-photon excitation have not been the subject of a detailed study, as far as we are aware of, especially considering the recombination behavior at high excitation. Two-photon processes are interesting for certain upconversion experiments, but even more importantly for large volume writing of holographic memory. Additionally, due to the fact that two-photon absorption coefficients are much smaller than single photon absorption coefficients, and because the absorption only decreases with $1/t$ and not according to Beer's law $\exp(-\alpha t)$, where t is the sample thickness and α the absorption coefficient, ultra-fast laser pulses penetrate the specimen much deeper providing more homogenous excitation. Applications include in-situ layer analysis and fluorescence imaging. As such, the two-photon excited photoluminescence properties are especially important to know as calibration standards for two-photon fluorescence imaging.[67]

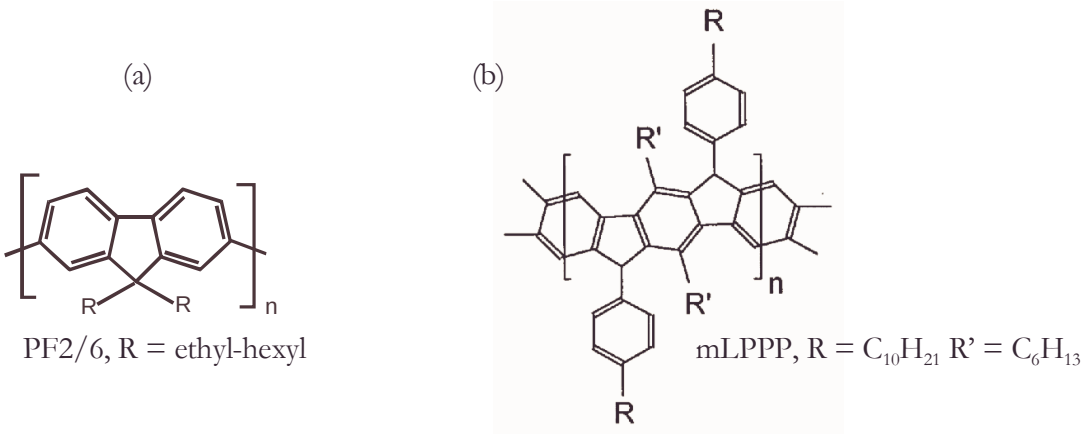

PF2/6, R = ethyl-hexyl

mLPPP, R = $C_{10}H_{21}$ R' = C_6H_{13}

Figure 40: (a) Chemical structure of PF2/6. (b) Chemical structure of mLPPP

3.2.2 Organic molecules analyzed by two-photon absorption

In this section, the two-photon absorption (TPA) and the two-photon excited photoluminescence (TEPL) properties of poly(9.9-bis (2-ethylhexyl) fluorene-2.7-diyl) – PF2/6 – dissolved in toluene and methylene-substituted ladder-type poly(para-phenylene) – mLPPP – dissolved in chloroform, are analyzed and discussed. The chemical structure of these polymers is shown in Figure 40. PF2/6 had a concentration of $c_{PF2/6}$ = 0.49 mmol/l, mLPPP a concentration of c_{mLPPP} = 0.22 mmol/l. This corresponds to optical densities at the absorption peak of 18 and 9, respectively. At twice the incident photon energy, 3.08 eV

or 402.5 nm, the optical densities are 7 and 4.5, respectively. These values correspond to a repetition unit concentration of $N_{PF2/6} = 2.4 \times 10^{17}$ cm^{-3} [65] and $N_{mLPPP} = 1.3 \times 10^{17}$ cm^{-3}.

3.2.3 Experimental

As mentioned above, PF2/6 was dissolved in toluene, mLPPP was dissolved in chloroform. The solutions were placed in glass vessels of 2 cm length and width. The solutions were illuminated with the 805 nm (1.54 eV) emission line of a 200 fs oscillator and amplifier system. The laser light was focused into the solution with a f = 10 cm lens and the focal spot had a diameter of around 0.01 cm. The photoluminescence spectra were measured at an angle of 90 degrees out of the optical axis directly at the focal point with an Ocean Optics fiber optics spectrometer. The fiber diameter was 100 μm. The transmission was measured with a calibrated silicon diode and a Keithley picoammeter. The transmission is an average of different intensities, since the beam diameter varies slightly with the position in the solution. Due to the fact that a two-photon process is investigated, the area directly around the focal point plays the biggest role in the transmission process. With an energy per pulse of 4 μJ, the intensity in the focal points reached up to 270 GW cm^{-2} Gaussian peak intensity.

3.2.4 Theoretical foundation for two-photon spectroscopy experiments

The TPA of PFO and mLPPP are shown in Figure 41 and in Figure 42, respectively. There are two different intensity scales; the bottom one is the mean intensity, assuming constant intensity for the pulse duration, which is not quite accurate but commonly used. The top is the Gaussian peak intensity, which will be used henceforward unless otherwise noted.

The change in number of photons per length element for a two-photon process is described by the following equation,

$$\frac{dI}{dx} = -\alpha_2 I^2, \tag{3-11}$$

where, x *is the actual depth of the beam in the sample,* I *is the intensity at* x*, and* α_2 *is the two-photon absorption coefficient.*

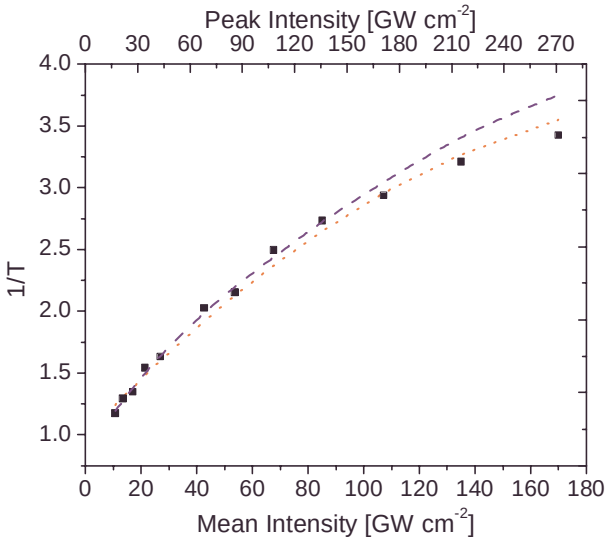

Figure 41: TPA measurements of PF2/6.
The black squares show the experimental data for PF2/6, the dashed curve shows the phenomenological hyperbolical fit with Equation (3-14), and the dotted curve shows the physically correct fit with Equation (3-25). It can be seen that for low intensities, both approaches give good results; however, the hyperbolical fit does not saturate enough at high intensities to explain the data.

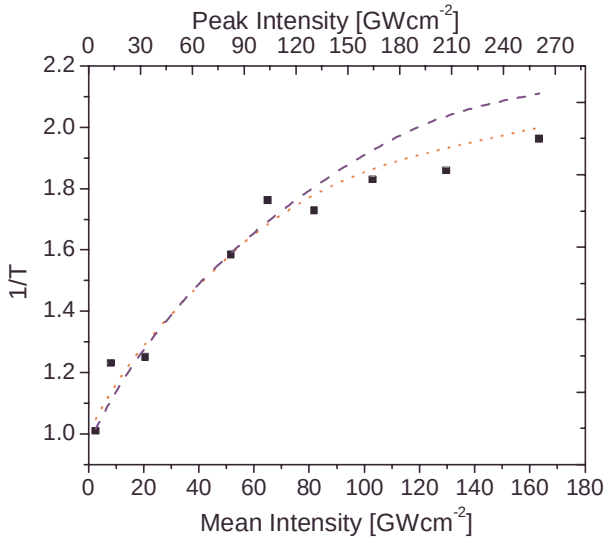

Figure 42: TPA measurements of mLPPP.
The black squares show the experimental data for mLPPP, the dashed line shows the phenomenological hyperbolical fit with Equation (3-14), the dotted line shows the physically correct fit with Equation (3-25). Again, it can be seen that at low intensities, both approaches give

good results, however, the hyperbolical fit does not saturate enough at high intensities to explain the measurements.

Assuming α_2 does not depend on the intensity, integration of Equation (3-11) results in,

$$\frac{1}{I_t} - \frac{1}{I_0} = \alpha_2^0 t\,, \tag{3-12}$$

where, I_t *is the transmitted intensity,* I_0 *is the incident intensity, and* α_2^0 *is the constant (or low level light) two-photon absorption coefficient.*

In general though, α_2 is a function of the incident intensity. There have been several approaches to describe saturation processes in two-photon processes empirically, specifically to describe the behavior of organic molecules in applications such as storage (photochromic polymers) and optical power limiting applications.[68-70] Another very common approach is to assume hyperbolic saturation.[65,71,72] Despite the fact that the hyperbolic approach allows for reasonable fits most of the time, the formula describes single-photon absorption saturation, only.[73] Still, it will be interesting to compare this to the physically correct approach. Hence, a derivation for both methods shall be shown. We start with the hyperbolical approach.

As mentioned above, the hyperbolical phenomenological approach uses the following equation to describe the saturation of the absorption coefficient:

$$\alpha_2 = \frac{\alpha_2^0}{1 + \dfrac{I}{I_{sat}}}\,, \tag{3-13}$$

where, I_{sat} *is the saturation intensity, and* I *is the incident intensity.*

Substitution for the TPA coefficient from Equation (3.13) in Equation (3.11) and integration leads to:

$$T = \frac{I_{sat}}{\ln(T) I_0 + \alpha_2^0 t I_{sat} I_0 + I_{sat}}\,, \tag{3-14}$$

a transcendental equation that converges very quickly using a self-consistent approach. This fit is represented as the dashed line in Figure 41 (PF2/6) Figure 42 (mLPPP). Similarily, photoluminescence can be fitted with Equation (3-15) for a hyperbolically saturating two-photon process:

$$I_{TEPL} \propto \alpha_2 I_{\mathrm{exc}}^2 = \frac{\alpha_2^0}{1 + \dfrac{I_0}{I_{\mathrm{sat}}}} I_{\mathrm{exc}}^2\,. \tag{3-15}$$

Equation (3-14) actually describes the experimental TPA data reasonably well, however we see that at high excitation intensities, the saturation is stronger than a hyperbolical trend.

This can be seen from Figure 41 and Figure 42, where the hyperbolical fit is shown as the dashed curve. The biggest problem with data fits using Equation (3-14), however, is that albeit being able to fit the experiment, the obtained values for the parameters α_2^0 and I_{sat} are off considerably. Fitting the PF2/6 data from Figure 41 with the hyperbolical approach gives α_2^0=1.6 x 10^{-2} cmGW^{-1} and I_{sat}=85 GWcm^{-2}. Compared to the results obtain from Equation (3-25) below, shown as the dotted curve, α_2^0 is 33% too high and I_{sat} is 52% too low. In other words, it is easy to derive wrong values for those two essential non-linear parameters by choosing the wrong model. Especially for materials with higher saturation intensities, such as PF2/6, both models give similar fits with very different parameters.

Therefore, saturation intensities and values for α_2^0 derived by this phenomenological approach should be handled with care and require reconsideration. The exact expression for the intensity dependence of α_2 is derived here.

At first, we consider the temporal behavior of the density of singlet excitons N_a, i.e. the variation of occupied states above the bandgap,[73]

$$\frac{\mathrm{d}N_a}{\mathrm{d}t} = -\frac{N_a}{T_1} + \frac{\alpha_2 I_0^2}{\hbar\omega}, \tag{3-17}$$

where, $\hbar\omega$ is the energy of two impinging photons (3.08 eV) since that is the energy absorbed per singlet exciton.

It is important to note that since the α_2 in Equation (3-17) depends on the difference between the number of electrons ground states and excited states, the second term signifies both the absorption process as well as the stimulated emission process. Equation (3-17) could be written differently using the transition crosssections for both the absorption and stimulated emission, but behavior of the equation does not change. Since the recombination time (T_1) – typically in the picosecond range – clearly exceeds the pulse duration we write,

$$\int \mathrm{d}N_a = \int_{-\infty}^{\infty} \frac{\alpha_2 I_0^2(t)}{\hbar\omega}\mathrm{d}t = \int_{-\infty}^{\infty} \frac{\alpha_2}{\hbar\omega}\left(I_0 e^{-\frac{4\ln(2)t^2}{\tau^2}} \right)^2 \mathrm{d}t\,, \tag{3-18}$$

where, τ is the FWHM pulse width of the laser.

Before the integration of Equation (3-18), one more obstacle has to be considered. α_2 is not a constant with time, since it depends on the number of available electrons in the ground state and the number of available states in the excited state. In first order, we can integrate Equation (3-18) assuming a constant, mean value of α_2 and integrate only over the intensity distribution, which gives,

$$N_a = \frac{\alpha_2 I_0^2 \tau}{\hbar\omega}\sqrt{\frac{\pi}{8\ln(2)}}\,. \tag{3-19}$$

The absorption coefficient itself can be described by the following equation,

$$\alpha_2 = \frac{(N_g - N_a)}{N}\alpha_2^0, \tag{3-20}$$

where, N_g *is the number of occupied states below the bandgap, and* N *is the total number of occupied states.*

In Equation (3-20) it is assumed that all the ground states and excited states have similar energies, and can therefore be treated as a two niveau system. This is a reasonable assumption for conjugated polymers. Per definition, $N = N_a + N_g$ and it follows by substituting N_a with Equation (3-19):

$$\alpha_2 = \frac{(N - 2N_a)}{N}\alpha_2^0 = \left(1 - 2\frac{\alpha_2 I_0^2 \tau}{N\hbar\omega}\sqrt{\frac{\pi}{8\ln(2)}}\right)\alpha_2^0. \tag{3-21}$$

Solving for α_2 leads to:

$$\alpha_2 = \frac{\alpha_2^0}{1 + I_0^2\left(\frac{2\alpha_2^0\tau}{N\hbar\omega}\sqrt{\frac{\pi}{8\ln(2)}}\right)} = \frac{\alpha_2^0}{1 + \frac{I_0^2}{I_{sat}^2}}, \tag{3-22}$$

with:

$$I_{sat} = \sqrt{\frac{N\hbar\omega}{2\alpha_2^0\tau}\left(\frac{8\ln(2)}{\pi}\right)^{\frac{1}{2}}}. \tag{3-23}$$

Both N and α_2^0 are expected to depend linearly on the concentration of the solution (i.e., the concentration of the repetition units) and therefore I_{sat} does not depend on the concentration.[65] However, Equation (3-23) allows us to determine the two-photon absorption coefficient α_2^0 very precisely, since the saturation intensity I_{sat} is determined reliably. In fact, to fit the transmission spectra correctly, I_{sat} has to be determined to 5% accuracy, to fit the TEPL as well, it has to be within 2% accuracy. Even more importantly, this enables us to calculate the value of α_2^0 with good precision just from TEPL measurements. The knowledge of I_{sat} and α_2^0 with Equation (3-19) makes the precise calculation of the excited carrier density possible.

Substituting the intensity dependent α_2 in Equation (3-11) with Equation (3-23) leads to the following equation,

$$\int_{I_0}^{I_t}\left(\frac{1}{I^2} + \frac{1}{I_{sat}^2}\right)dI = -\int_0^t \alpha_2^0 dx, \tag{3-24}$$

where, t *is the thickness of the sample.*

Defining the transmittance by $T = I_t/I_0$, we get from Equation (3-24),

$$T = \frac{1}{2}\left(-\frac{I_{sat}^2}{I_0^2} - \frac{I_{sat}^2}{I_0}\alpha_2^0 t + 1\right) \pm \sqrt{\left(\frac{I_{sat}^2}{2I_0^2} + \frac{I_{sat}^2}{2I_0}\alpha_2^0 t - \frac{1}{2}\right)^2 + \frac{I_{sat}^2}{I_0^2}}\,, \tag{3-25}$$

whereas only the positive root gives physically relevant results.

Knowing that $I_{TEPL} \propto N_a$, the substitution of Equation (3-23) into Equation (3-19) leads to the following proportionality,

$$I_{TEPL} \propto \frac{\alpha_2^0}{1 + \frac{I_0^2}{I_{sat}^2}} I_0^2\,, \tag{3-26}$$

for the emitted TEPL intensity.

3.2.5 Fit of the experimental data and discussion

The transmission data of PF2/6 and mLPPP in Figure 43 (b) and Figure 44 (b), respectively, are fitted with Equation (3-25). For this fit, both I_{sat} and α_2^0 are relevant fit parameters. The TEPL data of PF2/6 and mLPPP shown in Figure 43 (a) and Figure 44 (a) are fitted with Equation (12), where only I_{sat} is a relevant parameter, α_2^0 is absorbed into the proportionality factor. The TEPL emission from the polymers in solution is also shown in Figure 45. The values obtained by fitting TPA and TEPL are shown in the first four columns of Table 5. For comparison reasons, the values for the Gaussian peak intensity scale and the mean intensity are shown.

Equation (3-23) allows verification of the values of α_2^0. τ is 200 fs, for N the number of repetition units is stated in the experimental section. The results are shown in the last column of Table 5. These values are in reasonable agreement with those obtained via the transmission fit method, however they are significantly more accurate.

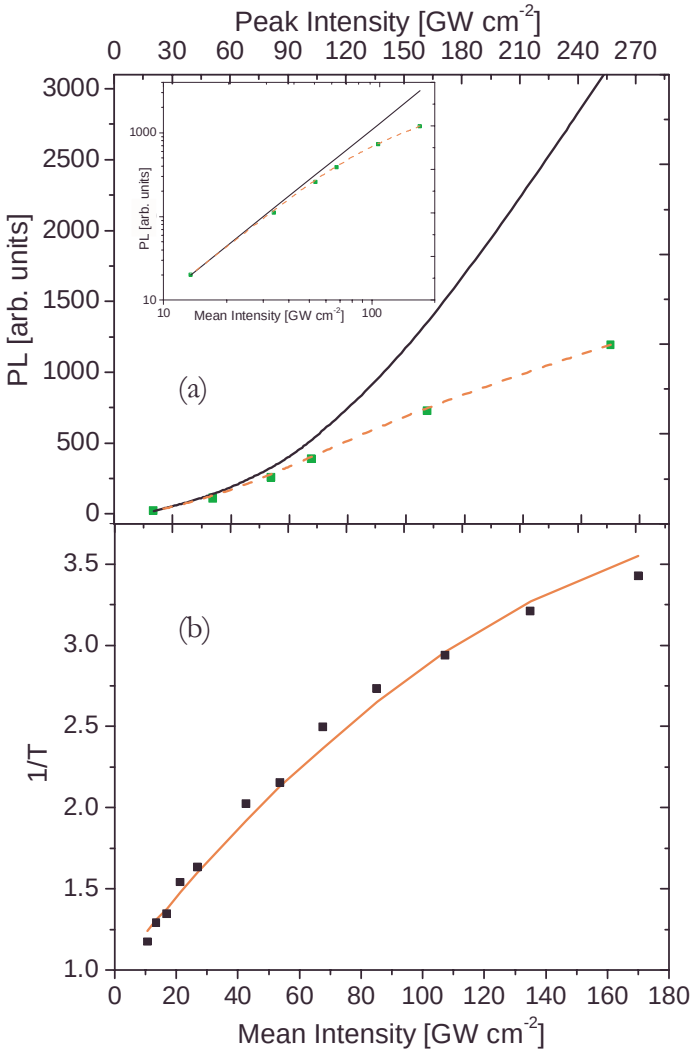

Figure 43: Two-photon spectroscopy of PF2/6.
(a) TEPL of PF2/6. The squares represent the measurement data, the solid line a purely quadratic function, the dashed line a saturating quadratic function. The inset shows the same graphs in a double-logarithmic diagram. (b) TPA of PF2/6. The squares represent the measured data, the solid line the fit according to Equation (3-20). The x-axis scale is the same as in (a).

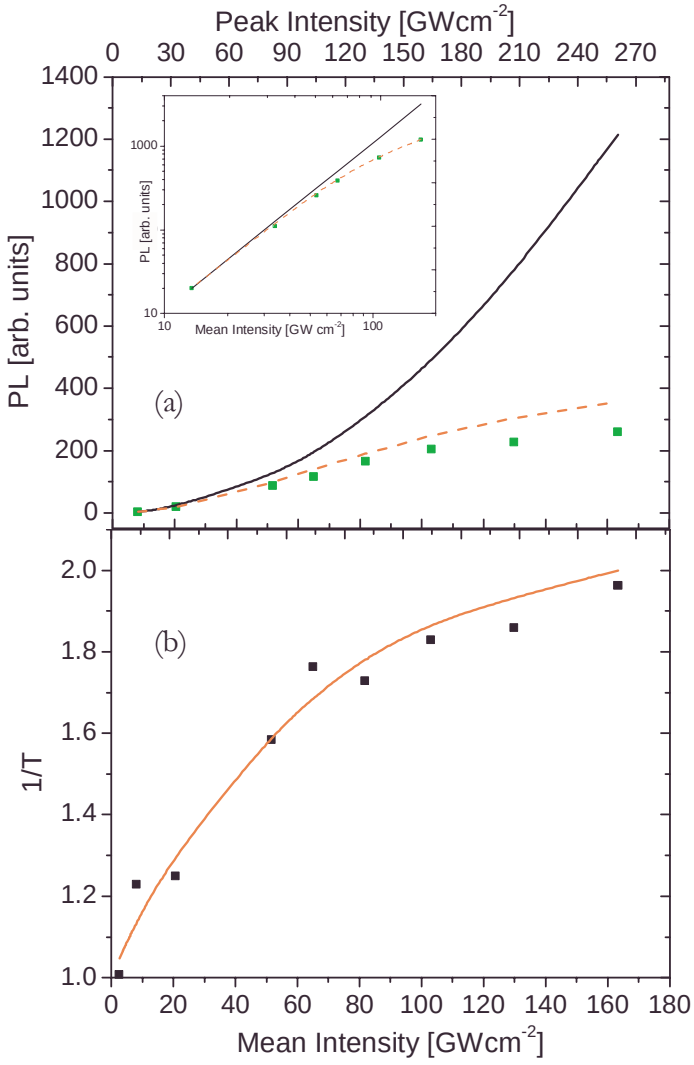

Figure 44: Two-photon spectroscopy of mLPPP.
(a) TEPL of mLPPP. The squares represent the measurement data, the solid line a purely quadratic function, the dashed line a saturating quadratic function. The scales are identical to Figure 43. The inset shows the same graphs in a double-logarithmic diagram. (b) TPA of mLPPP. The squares represent the measured data, the solid line the fit according to Equation (10). The x-axis scale is the same as in (a).

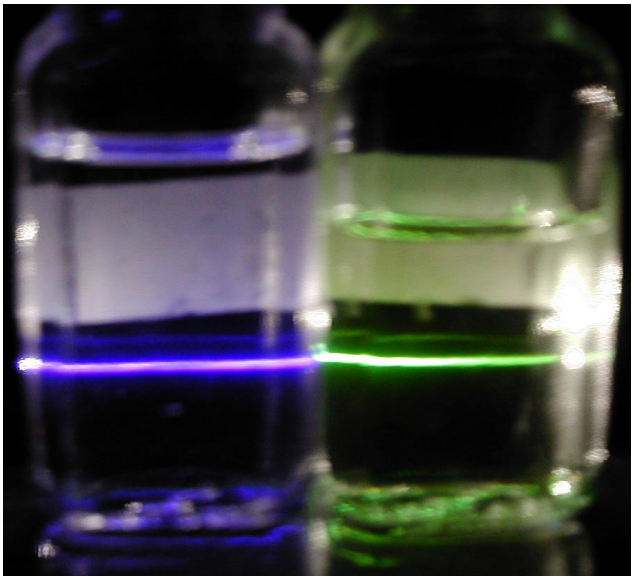

Figure 45: Two photon excited photoluminescence in solution. Left, the blue emission of PF2/6, right the green emission of mLPPP.

Table 5: Summary of two-photon absorption parameters for PF2/6 and mLPPP

	Parameters fitted with measured data				Calculated
	α_2^0 (cm/GW) peak intens.	I_{sat}(GW/cm^2) peak intens.	α_2^0 (cm/GW) mean intens.	I_{sat}(GW/cm^2) mean intens.	α_2^0 (cm/GW) peak intens.
PF2/6	7×10^{-3}	207	1.2×10^{-2}	130	9.2×10^{-3}
mLPPP	5.5×10^{-3}	160	9×10^{-3}	100	7.9×10^{-3}

Using Equation (3-19) the number of excited repetition units is calculated. The results are shown in Figure 46, where the scattered points coincide with measured intensities, and the curves extrapolate the results to higher intensities. The saturation effect visually limits the ratio of excited repetition units to 30% in TPA processes for very high intensities. This value holds true only for the fitted parameters. If we calculate α_2^0 instead, we get 50% excitation for very high intensties, as expect by Equations (3-19) and (3-22). Notably, in both samples, the percentage of excited charge carriers is in excess of 15% already at the saturation intensity, which is already a very high rate of excitation. Since there was no efficient feedback coupling between the molecular emitters in the solution, as introduced in cavities, no line narrowing was seen in the polymer solution, despite the high rate of

excitation in the polymers. In light of the number of excited repetition units it is interesting to once more look at the associated TEPL in Figure 43 (a) and Figure 44 (a). Whereas the fitted TEPL fits the PF2/6 data perfectly, the TEPL of mLPPP is lower than predicted by the theory, starting at an intensity of about 160 – 170 GW cm^{-2}. This corresponds to 15% excited repetition units in mLPPP, at which point the emission seems to be decreased by intrachain luminescence quenching. Interchain photoluminescence quenching has been observed previously.[74] However, by measuring the TEPL in solution, where the concentration is several orders of magnitudes lower than in a film, we excluded the occurrence of that kind of quenching. Thus, we actually observe the interaction of singlet excitons on the same chain in mLPPP, but not in PF2/6. This leads to the conclusion that the wavefunction of the singlet exciton in PF2/6 is more confined and does not interact with adjacent excitons. It is especially noteworthy that PF2/6 does not show any luminescence quenching within the investigated regime underlining once more its outstanding emission properties.

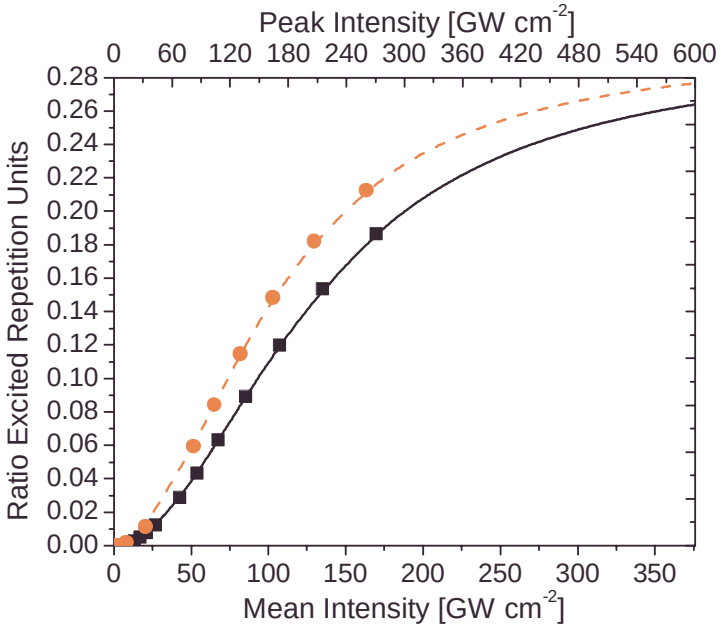

Figure 46: The ratio of excited to ground state repetition units. PF2/6 data is shown as squares, mLPPP data is shown as circles. The underlying lines, PF2/6 solid, mLPPP dashed, extrapolate the behavior to higher excitation rates. The theory predicts a complete saturation at 25% excited repetition units for both materials in the case of two-photon absorption.

From the measured and theoretically fitted TEPL intensities, the exciton-exciton quenching rate is calculated. The quenching itself is defined as ($I_{\mathrm{TEPL,theor}} - I_{\mathrm{TEPL,\,exp}}$), and the quenching rate is

$$\eta_{\text{exc.quench}} = \frac{I_{\text{TEPL,theor.}} - I_{\text{TEPL,exp.}}}{I_{\text{TEPL,theor.}}}. \qquad (3\text{-}27)$$

Owing to the nature of two-particle interaction, the number of quenched excitons depends quadratically upon the exciton concentration in the polymer. Therefore, the quenching ratio $\eta_{\text{exc.quench}}$ in Equation (3-27) theoretically depends linearly upon the exciton concentration. In Figure 47, the quenching ratio in mLPPP is plotted versus the relative number of excitons per repetition unit and the absolute number of excitons per cubic centimeter. Indeed, in full accordance with the theory, the data shows a linear behavior. The result presented here is, to our best knowledge, the first proof of intrachain exciton-exciton quenching in the literature.

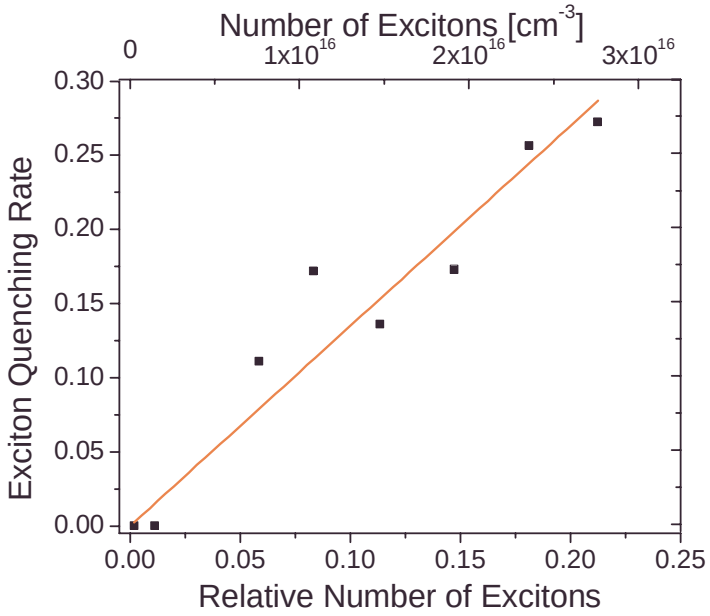

Figure 47: Exciton quenching in mLPPP.
The exciton quenching rate in mLPPP versus the relative number of excitons per repetition unit and versus the absolute number of excitons per cubic centimeter. The rate depends linearly upon the number of excitons in perfect agreement with the theory.

In the beginning of this section, we set out to determine the photoluminescence performance of two organic polymers at high excitation rates. We showed that in mLPPP excitons on the same polymer strand quench each other and therefore increase the rate of non-radiative recombination. We also saw that PF2/6, due to its intermittent ladder type structure, does not show any intrachain exciton quenching up to excitation rates of 25%.

Chapter 4

SPECTROSCOPY OF II-VI SEMICONDUCTORS

Discovery consists of seeing what everybody has seen and thinking what nobody has thought

Albert Szent-Györgyi

4.1 Motivation for Using II-VI Semiconductors

It was mentioned in 2.1.2 that inorganic semiconductors are crystals either of atoms in the IV column in the periodic table purely, or of combinations of column III and V or column II and VI materials. They have very different properties, for example type IV semiconductors like Si and Ga have indirect bandgaps[4] or are semimetals (α-Sn),[5] III-V semiconductors, such as GaAs,[75] InP,[76] or GaN[77] often have direct bandgaps and normally emit in the red and infrared spectral range, with the notable exception of nitride based semiconductors that emit in the green[78] or blue[79], dependent on the doping. II-VI semiconductors, including CdS,[80] ZnS,[81] and ZnO amongst others, are direct wide bandgap semiconductors and emit in the green and blue.

The main advantage of II-VI semiconductors is that apart from nitride based semiconductors, they make up the group of direct wide bandgap semiconductors – very important for both emissive as well as photovoltaic applications. The disadvantage is that especially Cd, but also the other metals with the same valence shell configuration are quite poisonous. Another disadvantage is that, unlike the III-V semiconductors, the thin film deposition is more difficult, especially when high purity is desired. A lot of focus in the research in the II-VI field is dedicated to the production of highly luminescent semiconducting thin films. The next sections in this thesis are dedicated to the analysis of thin film CdS and the associated deposition techniques. The ultimate limitations of the different deposition methods are analyzed and discussed. One of the biggest interests when it comes to the deposition technique is the analysis of the interfacial quality that can be achieve, since this will often limit the conduction and/or optoelectronic properties in a deceisive manner.

4.2 Materials and Thin-Film Deposition

4.2.1 Deposition techniques for thin film cadmium sulfide (CdS)

There are, at the very least, nine different deposition techniques used for CdS, with varying results for the photoluminescence quantum yield (PLQY). Apart from pulsed laser deposition (PLD),[82,83] spray pyrolysis,[84] close-space vapor transport (CSVT),[85] and evaporation,[86] which are discussed here, deposition may be done by chemical vapor deposition (CVD),[87,88] metallo-organic vapor-phase epitaxy (MOVPE),[89] chemical bath deposition (CBD),[90-92] photochemical deposition,[93] and rf sputtering.[94] Discussing all these methods would truly require a thesis in its own, and therefore I will only discuss deposition techniques for films that were actually studied as part of this thesis. The majority of this chapter will study the film qualities and emissive behavior of samples deposited by pulsed laser deposition and spray pyrolysis.

4.2.2 Spray pyrolysis

The basic concept of spray pyrolysis is to dissolve both parts of the semiconductor compound, e.g. Cd and S, in a chemical bath. The chemicals are sprayed onto a heated substrate, upon which the solvent evaporates due to the endothermic reaction of the two compounds forming the thin film. The substrate can be preheated, which allows for immediate reaction on the surface, avoiding dangling bonds due to incomplete reaction between the two compounds. The crystallinity at the interface, however, suffers from that approach. The spray nozzle can be driven either by gravity (top-down configuration) or by gas pressure (top-down and sideways configurations). Driving by gas pressure has two advantages, for one the flow can be controlled much more sensitively, but also the gas can also be used as part of the compound semiconductor, such as O_2 for ZnO. However, for most compound semiconductors, N_2 or an inert gas is used to avoid chemical reactions between the compound materials and/or the solvent, which would lead to additional impurities. It is important to heat the substrate enough to allow complete evaporation of the compound solvents and to make sure that the endothermic reaction forming the semiconductor is as complete as possible. The resulting films often have optically rough surfaces, which need to be polished for use in optical experiments.

The CdS investigated further down was dissolved in solution with 10^{-8} M Cu^{+}, and sprayed onto a Pyrex® substrate to ensure thermal stability. After deposition, the film was polished close to optical smoothness of the surface.

4.2.3 Evaporation

This is a very simple process, which is also used for organic molecules that are thermally resistant to evaporation, and basically involves heating up a crystal and sublimating it. The two compounds have different evaporation temperatures, and therefore the stoichiometry can be influenced, although typically a balanced stoichiometry is desired. The substrate is heatred to make sure that the thin film grows slowly onto the substrate. The biggest problem with this method for deposition is that typically one compound will evaporate more readily than the other, and a lot of dangling bonds as well as displacement and substitution defects will deter the sample quality.

4.2.4 Close-space vapor transport (CSVT)

CSVT is either based on the principle of chemical vapor deposition (CVD), or on physical vapor deposition. The basics of this method can be found in many books.[95]

The principle of this method is that the reaction of a compound to chemically bond with the vapor can be endothermic or exothermic. This determines whether the temperature of the substrate (exothermic) or the deposition material (endothermic) has to be higher. The transport vapor is reused through the deposition process, in contrast to open tube vapor transport. When tuned correctly, the transport vapor continuously accepts compound material at a temperature T_A and deposits continuously onto the substrate at a temperature T_S. Therefore, the chemical reaction between compound material and transport vapor has to be completely reversible.

For the specific example CdS, reacting with the vapor (either H_2 or I_2) is an endothermic process, so the source material is kept at a higher temperature than the substrate.

The specific reaction in the CSVT process is either:[96]

$$CdS(s) + H_2(g) \underset{680°C}{\overset{740°C}{\Longleftrightarrow}} Cd(g) + H_2S(g) \tag{4-1}$$

or:[97]

$$CdS(s) + I_2(g) \underset{680°C}{\overset{740°C}{\Longleftrightarrow}} CdI_2(g) + S(g) \tag{4-2}$$

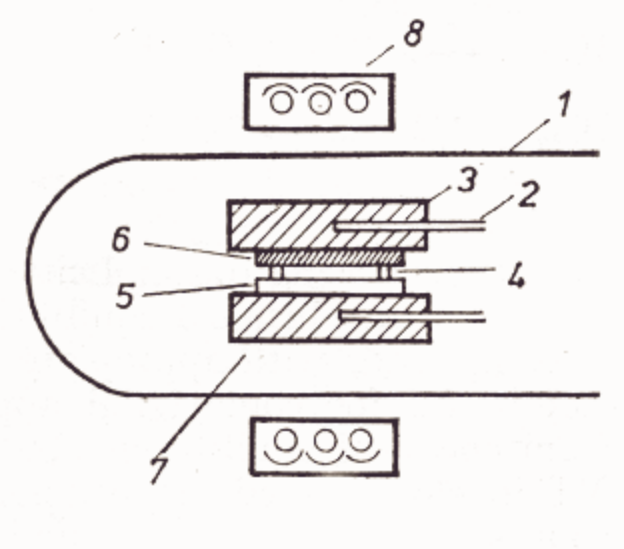

Figure 48: Close-space vapor transport deposition tube.
The different elements are, (1) tube containing the transport vapor, (2) thermocouples, (3) graphite slabs, (4) spacers, (5) deposition material, (6) substrate, (7) transport vapor, (8) infrared heaters.

The substrates used for CdS CSVT deposition range from GaAs, over GaP, to Tantalum (Ta).

The samples studied during my thesis work, however, are based on a physical vapor transport. The transport vapor in this case is argon, and the substrate for the deposition is CaF, due to the excellent lattice matching with CdS.

The decisive advantage of the CSVT deposition is that the growth process is normally epitactical on the surface of the substrate, which makes the quality of the interface and the bulk of the film much better with regard to the previously discussed methods. It also limits the number of usable substrates, and all three substrates listed above are not transparent in the majority of the visible spectrum – which can be undesirable for many emissive or photovoltaic device applications.

4.2.5 Laser ablation / pulsed laser deposition (PLD)

PLD is a method not too dissimilar from evaporation, as it does not involve the use of any chemicals in the deposition process, any sort of substrate can be used, and it is a thermal process as well.

However, this is where the similarities end. PLD delivers much higher sample quality, offers two distinctively different ways to ablate the material, one on an atomic level, and one on a cluster level.

The principle of PLD is the following. A high power laser source, often a Nd:YAG laser, is used to illuminate a target with a highly focused beam. The target needs to be absorptive around the laser wavelength. The material thermally evaporates and hits a heated substrate surface, where it deposits.

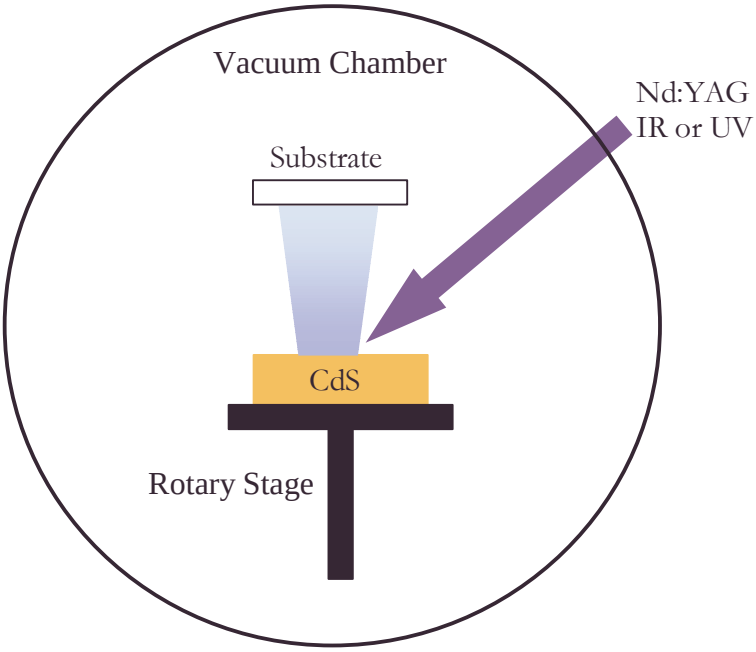

Figure 49: Pulsed laser deposition setup

In Figure 49 a typical PLD setup is shown. The target, CdS in that case, is mounted on a rotary stage to ensure that the material is ablated homogeneously off of the target. The vacuum chamber makes sure that the ablated CdS does not collide with any air particles, which could lead to impurity incorporation or chemical altering of the compound. The substrate is preheated to allow the films to grow as smoothly as possible. However, ablation is a process that has the target material travel very fast towards the surface, so epitactical growth does not occur.

The choice of the laser line has a very specific role in the PLD. One possibility is to use the main 1.17 eV infrared laser line of a Nd:YAG. Although many semiconductors have a bandgap exceeding that value, e.g. CdS 2.5 eV, ZnS 3.9 eV, there is some residual absorption due to impurities in the target. The low absorption ensures homogeneous illumination of the entire target. Because the absorption is intra-gap, all recombination is non-radiative, heating up the sample. The residual absorption typically shows values of the

order of magnitude of $\alpha = 10\ cm^{-1}$. Thus, the penetration depth is about 1 mm, which is the part of the target that actually gets heated through the laser. This kind of PLD is very similar to evaporation, as it evaporates cadmium and sulfide as separate atoms, before the CdS compound is formed once more on the substrate. Similarly to evaporation, the rate of evaporated Cd and S, and especially the rate of atoms settling on the surface depends on their evaporation temperature. Cd and S have boiling points of 1040 K and 718 K, respectively.[98] Due to this difference, the stoichiometry may not be balanced. This will lead to either strong n-doping or p-doping, depending if there is an exceeding amount of sulfure or cadmium, respectively. A picture of laser ablation using this principle is shown in Figure 50, below.

The other possible laser line is one that is above the bandgap. In this case the excitation will be stronger localized, because the absorption is much higher, $\alpha > 10^5\ cm^{-1}$. Also, luminescent recombination is possible in this case and is a competitive process to the thermal excitation. The biggest difference, however, is the strongly localized heating, and the resulting high temperature gradients. The result is that the compound in this case is ablated as a cluster of several molecules. Therefore, the stoichiometry is much more balanced and the resulting film will be intrinsic or only lightly doped. Additionally, it seems intuitive that since the clusters will attach themselves differently depending on their speed, or the slope of the local temperature gradient, that the laser intensity can control the film morphology on the substrate to some extent. This is shown in Figure 51.

Figure 50: Picture of laser ablation with 1.17 eV Nd:YAG line. The picture shows thermally emitting cadmium and sulfide particles emerging from the target.

For CdS, with a gap of about 2.5 eV, the 3.5 eV Nd:YAG laser line is sufficiently above the bandgap to allow this type of laser ablation. Although their will be some grain boundaries, many high impact energies allow "in-situ" annealing of the simple, i.e. the clusters have enough energy upon reaching the substrate to align their grain boundaries, especially when the substrate is heated. The crystallinity of the film, however, will be lower than in IR-PL deposited films, as shall be shown with X-ray measurements below. Additionally, initial

growth of the film on the substrate surface will be poly-crystalline with a high defect rate, since the substrate does not show a similar lattice structure. The adherence CdS on glass is not very high either, and the initial deposit grows as islands, ref. Figure 52.

Figure 51: Picture of laser ablation with 3.51 eV Nd:YAG line. The picture shows clusters of CdS as a plume moving from the target, bottom left, to the substrate, top right.

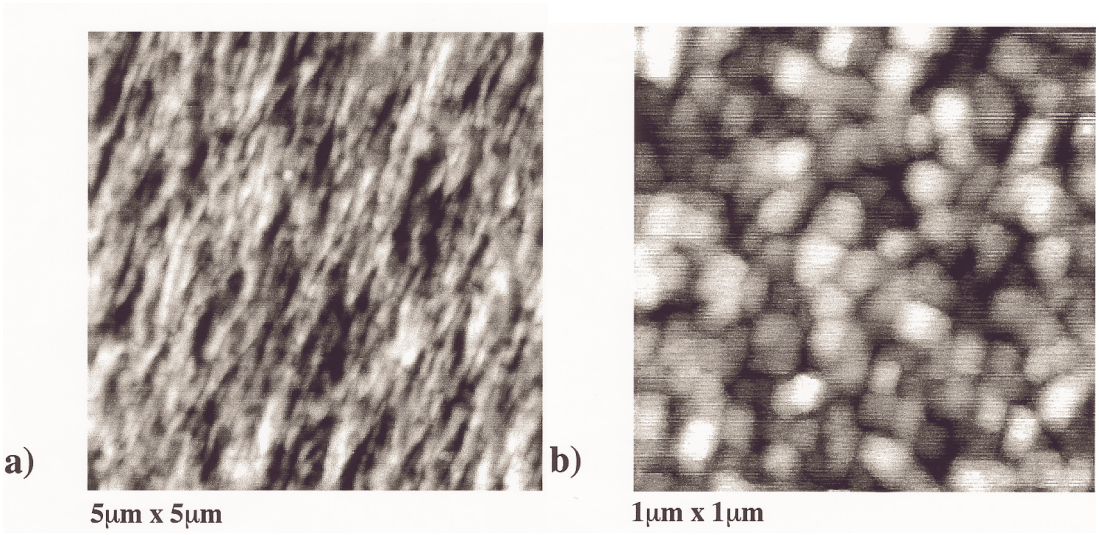

Figure 52: AFM picture of thin film CdS.
a) Depth profile of thin film CdS (< 200 nm) on a five by five micron scale. b) Depth profile of thin film CdS on one by one micron scale.

Only after about 200 nm of growth, the film surface starts to be smoother and the crystallinity improves dramatically.

Specifically when CdS is deposited with laser ablation, the thin film properties depend both on the ablation laser line, as mentioned above, but also on the laser intensity on the sample. It was already mentioned that using the infrared Nd:YAG laser line leads to thin films with unbalanced stoichiometry, or heavy doping in other words. This also limits the applications for these kinds of films.

IR-deposited CdS films exhibit a very high n-type doping, typically on the order of 10^{18} cm^{-3}, and therefore any charge carrier pairs created by a photovoltaic effects have a very low lifetime, since a hole created that way, immediately recombines with an electron. However, for the same reason of an abundant availability of electrons in the conduction band, radiative recombination with injected holes is very high, and therefore this type of CdS thin films shows a very high electroluminescence and photoluminescence efficiency.

Additionally, due to the high level of doping, IR-deposited CdS films exhibit the Burstein-Moss shift[99] naturally, i.e. due to the high concentration of donors, the lowest states in the conduction band are filled, and thus the bandgap is increased. The effect is described by the following equation,[99] assuming high degeneracy and a simplified parabolic bandstructure as discussed in 2.1.2 ,

$$E_{abs} = E_g + \frac{\hbar^2}{2m_e^*}\left(3\pi^2 n\right)^{2/3}, \tag{4-3}$$

where: E_{abs} *is the energy of the absorption edge,* E_g *is the bandgap energy,* n *is the dopand carrier concentration.*

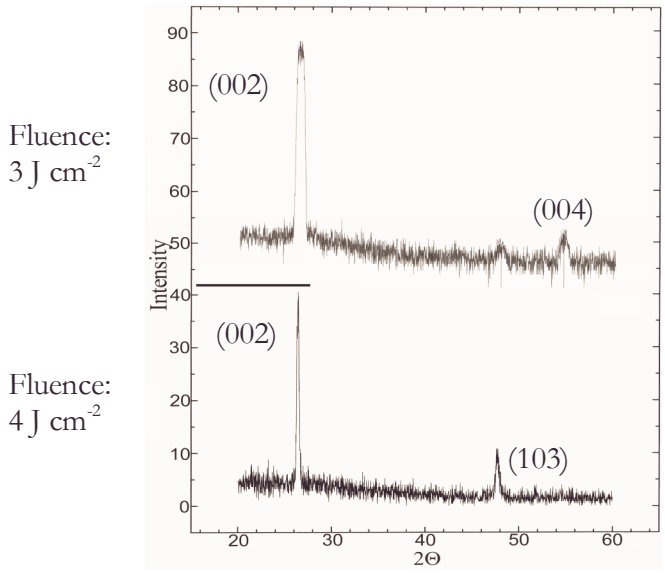

Figure 53: X-ray analysis of CdS thin films deposited by IR-PLD.[100,101]
Top: CdS thin film created with a laser fluence of 3 J cm^{-2}. The orientation of the c-axis is strictly perpendicular to the surface, a (001) orientation. However, the FWHM of the peaks suggests imperfect crystalline order. Bottom: CdS film created with a laser fluence of 4 J cm^{-2}. The c-axis is now tilted away from being perfectly perpendicular to the substrate, and the film has a better crystallinity.

Additionally, CdS deposited with IR PLD is always oriented along the (001) axis, which can be determined by X-ray analysis, as seen in Figure 53.

Contrarily, CdS ablated by UV radiation exhibits much less doping, typically below 10^{16} cm^{-3}, and is therefore more ideally suited for photovoltaic applications, since the radiative recombination rate is much lower than in IR-PLD thin films. By the same token, it exhibits much lower luminescence. Due to the reduced doping level, there is no Burrstein-Moss shift and the optical gap coincides with the energy gap (if we neglect the Urbach tail for now, see further down in this chapter). Even more importantly, depending on the laser intensity, the growth of the crystalline islands on the substrate can vary dramatically.

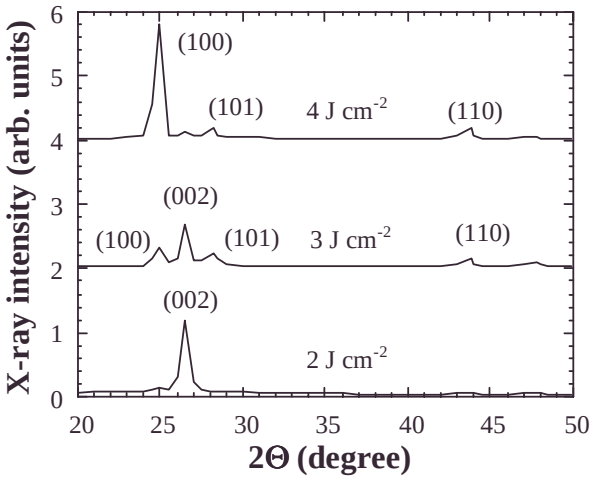

Figure 54: X-ray analysis of CdS thin films deposited by UV-PLD.[102] Top: CdS thin film created with a laser fluence of 4 J cm^{-2}. The peaks indicate a hexagonal symmetry, which occurs if the Wurtzite structure CdS has its c-axis in plane with the surface. Bottom: CdS film created with a laser fluence of 2 J cm^{-2}. The c-axis is now tilted away from being perfectly perpendicular to the substrate. In the middles, at a laser fluence of 3 J cm-2, an intermediate film morphology is shown, with clusters of CdS having their c-axis in plane with or perpendicular to the surface.

In Figure 54, the diochroism of CdS deposited with UV line laser ablation is shown. Depending on the impinging laser intensity, the Wurtzite structure can either be oriented with the c-axis perpendicular or parallel to the surface. This induces a shift in the absorption edge, depending on whether or not the **E** vector of the incident radiation is parallel or perpendicular to the c-axis, which can change its lattice constant more freely than in the x-y plane, due to the hexagonal structure.

In fact, this is a very interesting property of CdS that shall be investigated in the next section.

4.2.6 Experimental analysis techniques

The photocurrent was measured under the illumination of a 300 W tungsten lamp through a SPEX monochromator and an optical chopper, and the signal was detected with a lock-in amplifier and a picoammeter without the optical chopper in the beam path.

The photoluminescence was detected with an Ocean Optics optical fiber spectrometer, fiber diameter of 100 μm. The photoluminescence was detected either in transmission or reflection geometry, that is the fiber on the opposite side or same side as the excitation, respectively. Unless otherwise noted, the transmission geometry was used.

The excitation was provided by a Coherent ultrafast laser system in the case of the two-photon excited photoluminescence (TPL). A femtosecond oscillator and amplifier array emitted 804 nm (1.54 eV) pulses of 4 μJ per pulse. The beam was focused onto the sample with a focal radius of 50 μm. In the case of single photon excited photo-luminescence (SPL) a multiline Ar+ laser was used, and the 457 nm line was selected with the aide of an interference filter.

4.3 Dichroism of UV Laser Ablated Thin Film CdS

4.3.1 CdS samples investigated by transmission, photocurrent, and photoluminescence spectroscopy

The samples investigated here were prepared by PLD by guiding the 355 nm emission of Nd:YAG laser (pulse width 5 ns, repetition rate 10 Hz) onto a target of sintered CdS (99.999%) powder. The distance between the target and the fused silica glass substrate was 3 cm. During the PLD process the substrate temperature and ambient pressure were kept at 250°C and 10^{-3} Pa, respectively. The samples were formed with laser fluences of 2 J cm^{-2} and 5 J cm^{-2}, resulting in CdS with the c-axis perpendicular to the surface, $CdS_{\perp}$, and CdS with the c-axis oriented in plane with the surface, $CdS_{||}$. The corresponding X-ray patterns are shown in Figure 55.

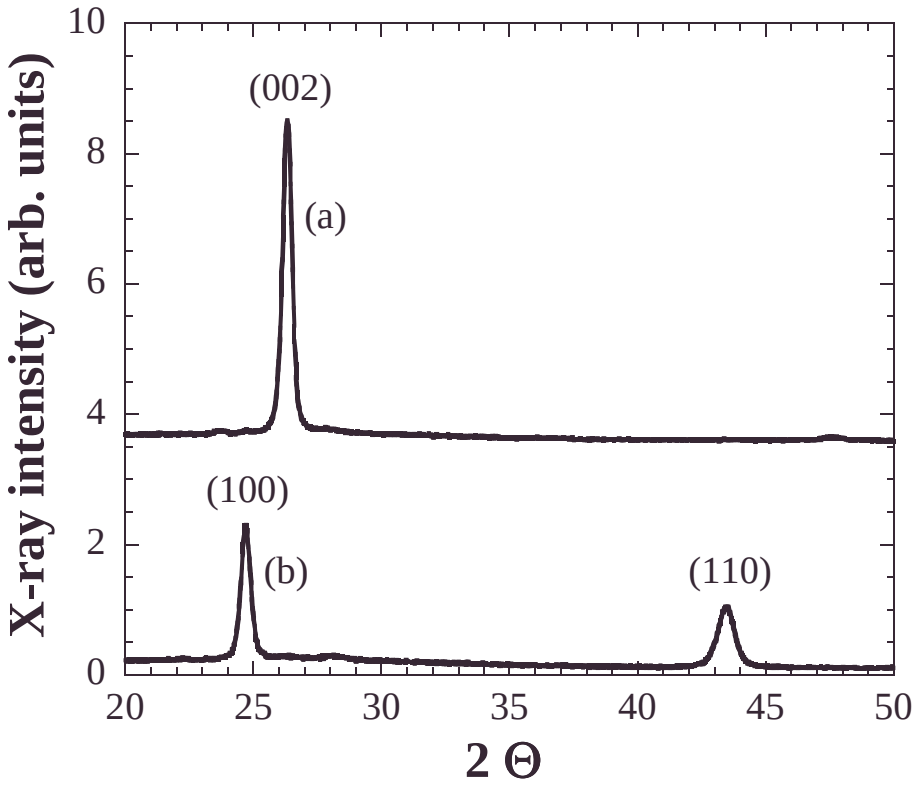

Figure 55: X-ray patterns of $CdS_{\perp}$ (a) and $CdS_{||}$ (b)

The thickness of the layers was determined by evaluating the interference fringes, and using the following equation:

$$t = \frac{1}{2n}\frac{\lambda_1\lambda_2}{\lambda_1 - \lambda_2}, \tag{4-4}$$

where: t *is the thickness of the sample,* λ_1 *is the first of two adjacent interference maxima,* λ_2 *is the second of two adjacent interference maxima.*

The thickness calculated for the two films is 1.7 μm and 0.82 μm for $CdS_{\perp}$ and $CdS_{||}$, respectively.

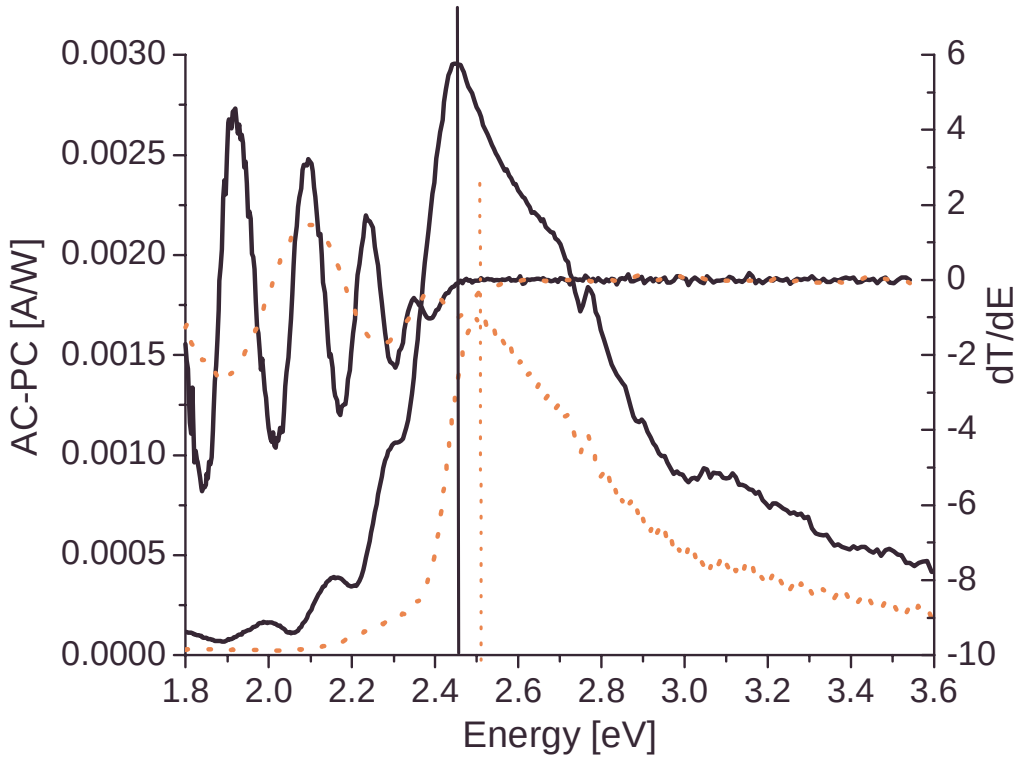

Figure 56: Dichroism in CdS, comparison of absorption with photocurrent measurements.
The dotted curves represent the CdS with the c-axis parallel to the surface, the complete curves CdS with the c-axis perpendicular to the c-axis. The two curves with the peak at 2.5, respective 2.45 eV depict the photocurrent measurements, measured with a lock-in amplifier. The associated scale is shown on the left y-axis. The other two curves show the first derivative of the transmission with respect to the energy. The absorption onset and the photocurrent response peaks coincide in both cases and are shifted by 50 meV with respect to the two different CdS thin films.

In Figure 56, the dichroism shift between $CdS_{\perp}$ and $CdS_{||}$ is shown for the first derivative of the transmission with respect to the photon energy, and compares it to the dichroism shift of the photocurrent, measured by means of a lock-in amplifier (AC photocurrent). In $CdS_{\perp}$, the onset of the absorption occurs at about 2.45 eV, which coincides with the photocurrent maximum.

This behavior is easy to explain: The CdS sample is about an order of magnitude thicker than the penetration depth for photons above the bandgap energy. That means that photons absorbed in the surface region do not contribute highly to the photocurrent, and the bulk only sees a strongly reduced intensity due to the high absorption. This is called parasitic absorption, or internal filter effect. Photons absorbed within the bandgap (Urbach tail, see the next section), do not contribute a lot to the photocurrent. This leaves photons

around the bandgap to contribute the strongest to the photocurrent, as they penetrate the sample, and at the same time create free electron/hole pairs.

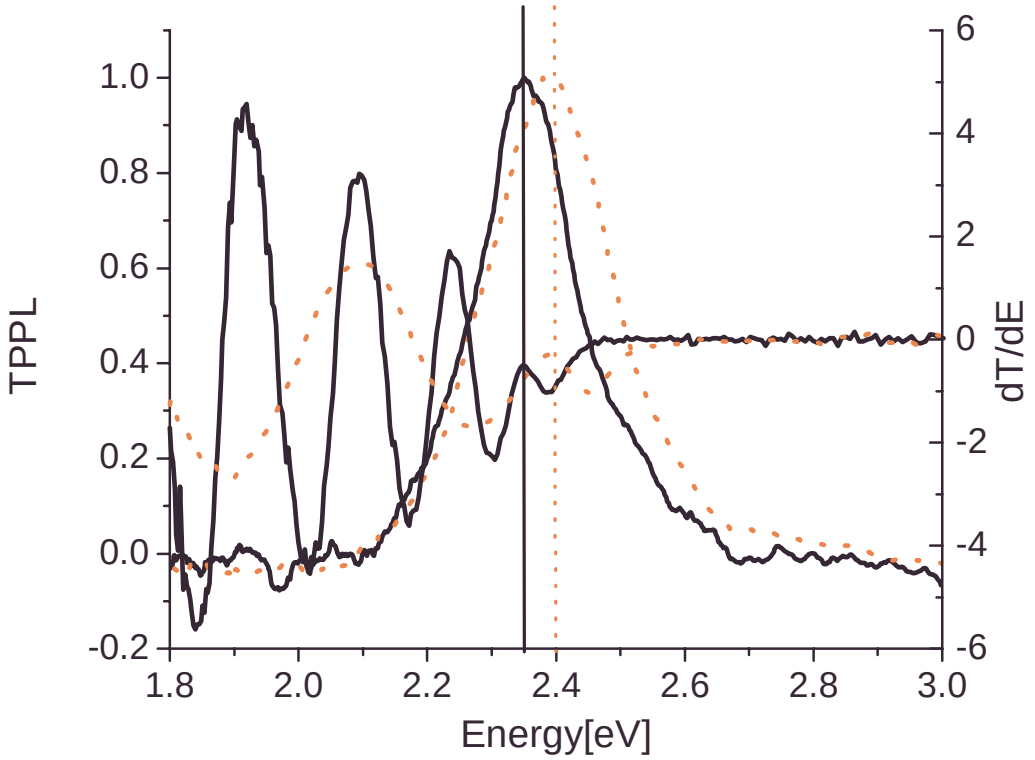

Figure 57: Dichroism in CdS, comparison of absorption with two-photon excited photoluminescence.
The dotted curves represent the CdS with the c-axis parallel to the surface, the complete curves CdS with the c-axis perpendicular to the c-axis. The two curves with the peak at 2.40, respective 2.35 eV depict the two-photon excited photoluminescence, measured with the Ocean Optics fiber optic spectrometer. The associated scale is shown on the left y-axis. The other two curves show the first derivative of the transmission with respect to the energy. The photoluminescence peaks in both cases coincide with the first minimum fringe in the absorption data, and show a 50 meV shift between the two thin films.

The shift between the samples is identical for both measurements, and amounts to 50 meV, a value that is conform to previous measurements.[103]

In Figure 57, the photoluminescence due to two-photon excitation is again compared to the first derivative of the transmission with respect to the energy. The two-photon luminescence (TEPL) is especially interesting, since it does not show any contribution in the red part of the visible spectrum, which *is* seen in the single photon excited photoluminescence (SEPL). Comparing the TEPL to the derivative of the transmission, we see that for both samples the maximum of the TEPL coincides with a relative minimum of the first derivative. This corresponds to a transmission maximum in the transmission, or in

other words constructive interference occurs in the sample at this wavelength. Once more, the shift equated to 50 meV, which is in accordance with the values for the photocurrent spectra.

4.3.2 Theoretical analysis of the luminescence with the van Roosbroeck/Shockley equation

In fact, the position of the emission maxima can be theoretically described with a simple principle derived by van Roosbroeck and Shockley.[104] The first thing we need to take into account is the thermal equilibrium distribution of the photon density, which depends on the density distribution of the normal modes in k-space,[104] or the Planck distribution of photon energies:

$$\rho_\nu = \frac{8\pi\nu^2}{c^3} n^3 \left(e^{[h\nu/kT]} - 1\right)^{-1}, \tag{4-5}$$

where: ρ_ν *is the density distribution of photons,* ν *is the photon frequency,* n *is the refractive index,* n_ν *is the number of normal photon modes in the material.*

Equation (4-5) gives us the distribution of photons we can expect due to photoluminescence. However, the re-absorption of emitted photons also needs to be taken into account. The transmission probability distribution for a photon of a given frequency ν can be described as:[104]

$$P(\nu) = \alpha v_g = \alpha \frac{c}{n}, \tag{4-6}$$

where: $P(\nu)$ *is the transmission probability for a photon,* α *is the absorption coefficient,* c *is the speed of light in the medium, and* v_g *is the group velocity of the photons.*

The photoluminescence we measure is the product of Equations (4-5) and (4-6) and hence:

$$I_{PL}(\nu) = \frac{8\pi\nu^2 n^2}{c^2} \alpha \left(e^{[h\nu/kT]} - 1\right)^{-1}, \tag{4-7}$$

where: I_{PL} *is the measured photoluminescence intensity.*

Equation (4-7) is sometimes called the principle of detailed balance, or the van Roosbroeck/Shockley equation.

For a perfect semiconductor, α depends solely on the distribution of the electronic density of states:[105]

$$\alpha_{DOS}(h\nu) = A\sqrt{h\nu - E_g}, \tag{4-8}$$

where: A *is a factor with a specific value for a certain semiconductor,* E_g *is the bandgap energy.*

However, in real semiconductors, Equation (4-8) only holds true well above the bandgap energy, since there are so-called "tail states" within the gap, due to surface states and intrinsic as well as extrinsic impurities, that influence the absorption. The residual absorption near the bandgap due to these intragap "tail states" is called the Urbach tail, and can be expressed with the following equation close to the bandgap:[105]

$$\alpha_{\text{Urbach}}(h\nu) = Ke^{\left[\frac{\sigma}{kT}(h\nu - E_g)\right]}. \tag{4-9}$$

where: σ *is a factor that determines the quality of the semiconductor. The higher* σ*, the lower the impurity concentration and the smaller is the absorption due to the Urbach tail.*

Equation (4-9) is basically just an exponential tail to the absorption, the magnitude of which is defined by *K*, the slope by σ and kT. Our free parameter is K, and it will be used to match Equation (4-8) and (4-9) at a crossover energy E_{cr}.

In order to be able to fit the photoluminescence data in Figure 57 with Equation (4-7), we need a function for α that is valid for the entire spectral range, i.e. an equation that combines (4-8) and (4-9) and is smooth at E_{cr}:

$$\alpha_{\text{DOS}}(E_{cr}) = \alpha_{\text{Urbach}}(E_{cr}), \tag{4-10a}$$

$$\alpha'_{\text{DOS}}(E_{cr}) = \alpha'_{\text{Urbach}}(E_{cr}), \tag{4-10b}$$

where: α' *denotes the first derivative with respect to the energy.*

With Equations (4-10a) and (4-10b) the following conditions are obtained:

$$A\sqrt{E_{cr} - E_g} = Ke^{\left[\frac{\sigma}{kT}(E_{cr} - E_g)\right]} \text{ or } \sqrt{E_{cr} - E_g} = \frac{K}{A}e^{\left[\frac{\sigma}{kT}(E_{cr} - E_g)\right]}, \tag{4-11a}$$

$$A\frac{1}{2\sqrt{E_{cr} - E_g}} = Ke^{\left[\frac{\sigma}{kT}(E_{cr} - E_g)\right]}\frac{\sigma}{kT}. \tag{4-11b}$$

Substituting for the square root in Equation (4-11b) with (4-11a) leads to:

$$K^2 = \frac{kT}{2\sigma}\frac{A^2}{\left\{\exp\left[\frac{\sigma}{kT}(E_{cr} - E_g)\right]\right\}^2}. \tag{4-11c}$$

Only the positive solution for K is physically relevant, and substituting (4-11c) into Equation (4-9) leads to:

$$\alpha_{\text{DUrb}}(h\nu) = A\sqrt{\frac{kT}{2\sigma}}e^{\left[\frac{\sigma}{kT}(h\nu - E_{cr})\right]}. \tag{4.12}$$

Instead of using E_{cr}, it would be preferable to use Equation (4.12) in terms of the bandgap energy E_g. From the requirement α_{DOS} and α_{DUrb} to be equal at E_{cr}, it follows that $A\sqrt{E_{cr}-E_g} = A\sqrt{\frac{kT}{2\sigma}}$ or $E_{cr} = E_g + \frac{kT}{2\sigma}$.

We can now express the crossover energy in (4-12) in terms of the bandgap energy.

$$\alpha_{DUrb}(h\nu) = A\sqrt{\frac{kT}{2\sigma}}e^{\left[\frac{\sigma}{kT}(h\nu - E_g) - \frac{1}{2}\right]} \tag{4-13}$$

Thus, Equation (4-13) is valid for $h\nu < E_{cr}$, and Equation (4-8) is valid for $h\nu > E_{cr}$ – and these equations can be used in Equation (4-7).

For undoped intrinsic CdS, it is generally accepted that σ=2.17. Numbers below 2.17 are typical for thin film CdS and indicate tail states beyond the intrinsic density. The following parameters were used to fit the data for $CdS_{\perp}$, E_g=2.33 eV, kT=25 meV, kT_c=55 meV, and σ=0.7, and for $CdS_{||}$, E_g=2.37 eV, kT=25 meV, kT_c=60 meV, and σ=0.6. The fit of photoluminescence data from Figure 57 is shown in Figure 58 and Figure 59, and the theory is in excellent agreement with the experimental data.

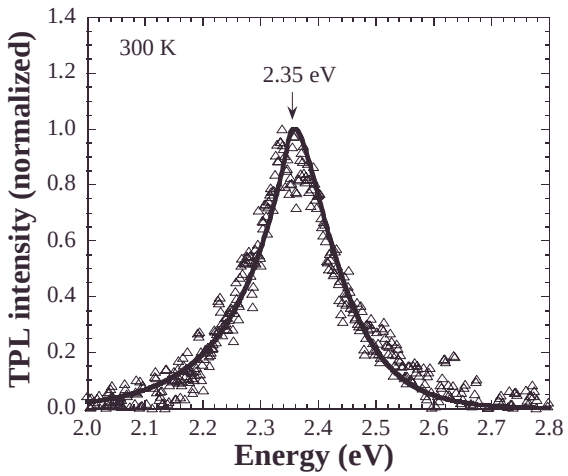

Figure 58: TEPL spectrum of $CdS_{\perp}$, experiment and fit.

The fit values once again show that the dichroic shift in CdS with perpendicular respective orientations is on the order of 50 meV. It is actually quite extraordinary to be able to fit the photoluminescence in a thin film with an equation that was only believed to be true for single crystals. The two-photo excited photoluminescence, in fact, seems to show very different recombination features than the single photon photoluminescence, as will be shown in the next section. The possible reasons for this are the high excitation density on the one hand, but also the altered recombination path due to the different parity of the two photon process.

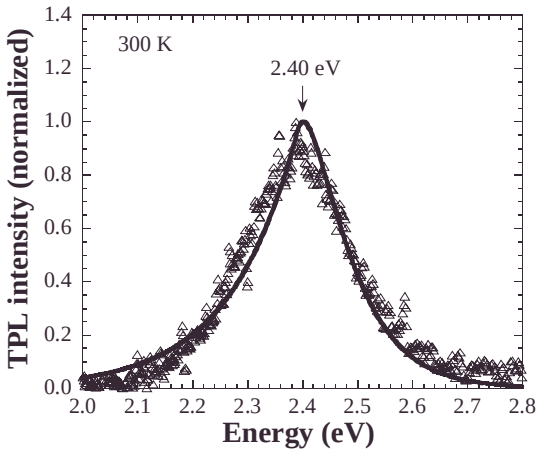

Figure 59: TEPL spectrum of CdS||, experiment and fit.

4.4 Glass/CdS interface analysis using two-photon absorption

In the previous section, the diochroism of UV deposited CdS was discussed by comparing the transmission data, photocurrent, and two-photon excited photoluminescence. We were able to describe the photoluminescence of a non-epitactically UV-PLD grown CdS thin film sample with the principle of detailed balance, valid for single crystals. In this section, we shall take a closer look at the emission properties of IR-PLD grown CdS films.

IR-PLD CdS is interesting because of its outstanding emission properties. Room temperature PL at 2.48 eV was shown to clearly dominate the emission spectrum, although the films exhibit emission in the red spectral region. [106] Furthermore, optically pumped lasing at 2.48 eV has been achieved with thin film CdS formed by PLD.[100,101,107] The quality of the samples are even more astonishing since the films are deposited onto amorphous substrates (glass), i.e., they represent a thin film in the "classic" sense and not an epilayer, which is grown on oriented substrates.

To analyze the absorptive and emissive properties of the surfaces/interfaced of the sample grown by IR-PLD, it is helpful to measure the photoluminescence invoked by both single photon and two-photon excitation, measuring the photoluminescence in reflection and transmission geometry.

The penetration depths of single photon and two-photon excitation are in fact quite different. Whereas the penetration depth for single photon absorption above the bandgap is equal to α^{-1}, i.e. $d_{pen} \approx 10^{-5}$ cm, two-photon excitation penetrates a sample much deeper. If we define the penetration depth for two-photon excitation analogous, i.e. $I = I_0/e$, then we get the following equation:

$$d_p = \frac{1}{\beta I_0}(e-1), \tag{4-14}$$

where: β *(=6.4 cm/GW)*[108] *is the two-photon absorption coefficient and* I_0 *is the impinging laser intensity (=190 GW/cm*^{2}*), and find* d_p*=14 μm.*

The studied sample has a thickness on the order of or less than 2 μm, therefore we assume that the sample are homogeneously illuminated by the two-photon excitation.

The investigated sample was prepared using Nd:YAG laser induced PLD at 1064 nm. Pulse width and repetition rate were 180 μs and 10 Hz. The sintered CdS target (99.999 %) was exposed to a laser fluence of 4 J cm^{-2}. During the deposition the substrate temperature and ambient pressure were kept a 250°C and 10^{-3} Pa, respectively. The distance between source material and substrate (glass slide) was about 3 cm. By transmission measurements it was found that the thickness of the film is 2 μm.

Although two-photon excitation allows us to illuminate the entire sample and therefore gives us a good idea about the bulk luminescence properties, the emitted light has to pass through either the glass/CdS interface or the CdS top face, depending on our measurement geometry. In order to exclude any influence occuring while measuring with only one geometry setup, we measured both and compared the results. The two setups are shown below:

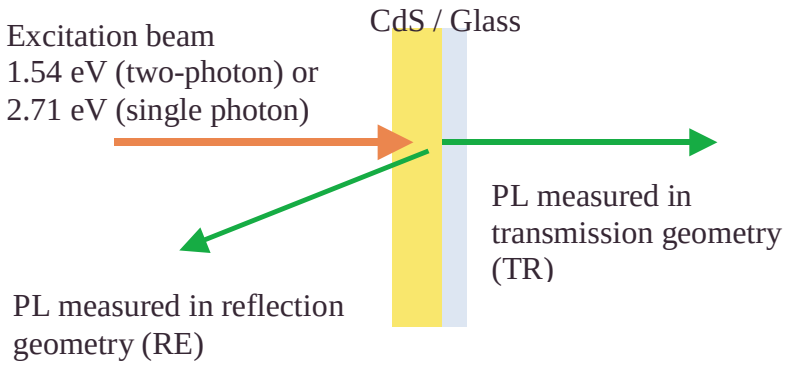

Figure 60: Measurement geometries for photoluminescence experiments.

The single photon excited photoluminescence (SPL) is shown in Figure 61. It can be seen that the green bulk emission is shifted to lower energies, whereas the red impurity luminescence does not seem to shift at all.

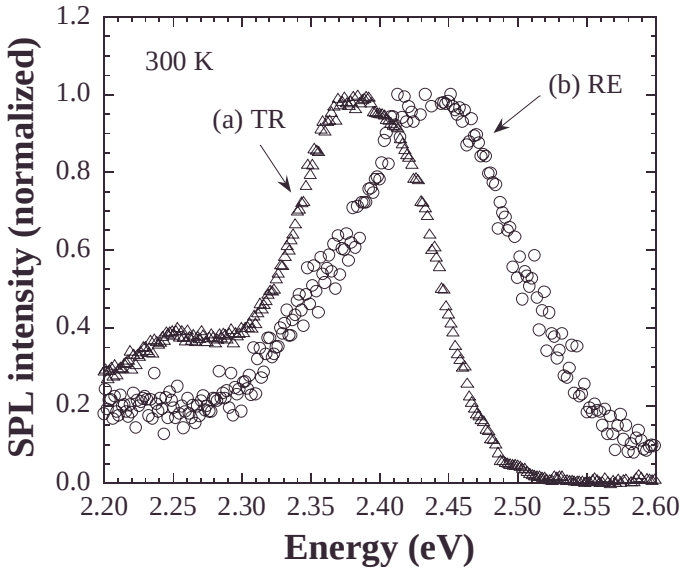

Figure 61: SPL of thin film IR-PLD CdS measured in (a) in TR and (b) RE geometry.

The reason why we see red luminescence in the green emitter CdS is that especially near the interface, the film morphology is far from perfect, and there are many displacement defects and unpaired compound atoms with dangling bonds. These intragap states actually have a non-zero luminescent recombination rate and deter from the pure green CdS luminescence.

Upon illumination of the same sample with two-photon excitation, the spectra look slightly different. First of all, looking at Figure 62, we note the absence of any photoluminescence contributions in the red spectral range. There are several possibilities as of why this would occur. First of all, with single photon excitation we illuminate mostly the surface area of CdS, which is much more prone to dangling bonds due to unbalanced stoichiometry, surface contaminations, and displacement impurities; whereas the two-photon absorption provides homogeneous excitation throughout the sample. The other possibility is that due to the even parity excitation, the recombination path differs between the case of single and two-photon absorption. Also, the excitation density tends to be higher in the case of two-photon excitation.

Again, the photoluminescence measured in the transmission geometry shifts to lower energies, although to a lesser degree than the SPL. Using Equation (4-7), we can fit the exact experimental photoluminescence spectra of CdS for two-photon excitation. However, in order to properly account for the shift, we have to assume different bandgap energies for the two different geometries, which does not make any physical sense. In fact, however, we will see that the apparent change in bandgap energy is entirely due to increased interface absorption.

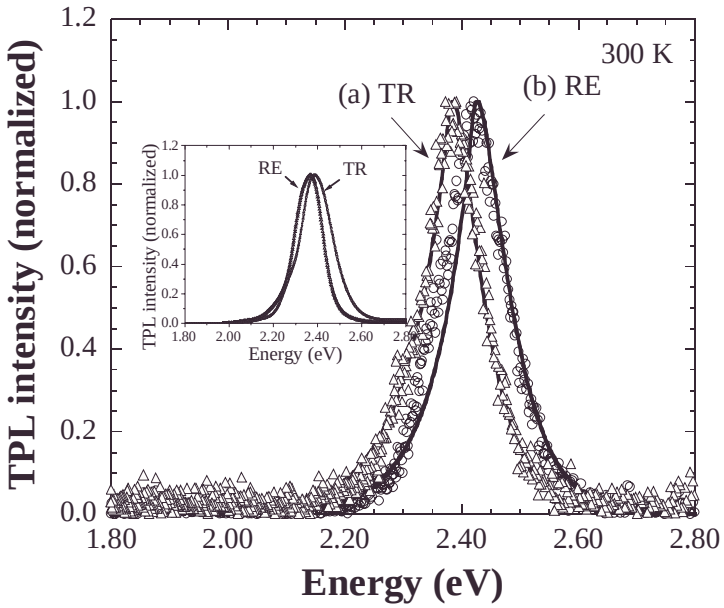

Figure 62: TPL of thin film IR-PLD CdS measured in (a) in TR and (b) RE geometry.
No photoluminescence in the red spectral range is visible. The inset shows the TPL for the same sample with illumination through the glass side.

The following parameters are used to fit the data, σ = 0.95, kT=25 meV, kT_c=40 meV for both spectra and E_g=2.365 eV and E_g=2.405 eV, for the TR and RE spectrum. The σ-value of 0.95 shows that the film is considerably doped directly after deposition. Compared to the fit parameters in the previous section, the value of σ has almost double. This shows once more that the stoichiometry in the IR-PLD process is off, and due to an excess amount of sulfur, there is considerable n-doping, on the order of 10^{17} cm^{-3}.

In Figure 62, the inset shows the photoluminescence in reflection and transmission geometry when the excitation is impinging through the glass side of the sample, in other words the excitation beam in Figure 60 is coming from the other side, in which case the roles of reflection and transmission geometry should be reversed. Indeed, that is the case, and the only explanation is that the residual absorption due to intragap states is higher at the glass/CdS interface area, which makes sense when thinking about the initial CdS growth process in glass, as shown in Figure 52.

In order to confirm this assumption, we need to check if the increased absorption of the interface explains the shift to lower energies properly, i.e. whether additional theoretically modeled absorption applied to the emission spectrum in reflection geometry shifts over to match the emission spectrum in transmission geometry.

The simplest approach to simulate the added absorption is with Beer's law:

$$I_{TR}(h\nu) \propto I_{RE}(h\nu)\exp(-\rho\alpha(h\nu)d_i), \tag{4-15}$$

where ρ *is the increased absorption of the glass/CdS interface,* α *is absorption coefficient calculated in Equation (4-8) and (4-13),* d_i *is the thickness of the interface.*

The thickness of the interface can be estimated at d_i = 100 nm, which is the initial surface roughness during the laser ablation process. Figure 63 shows the result of the fit according to Equation (4-15) with ρ=2.5 and d_i=100 nm.

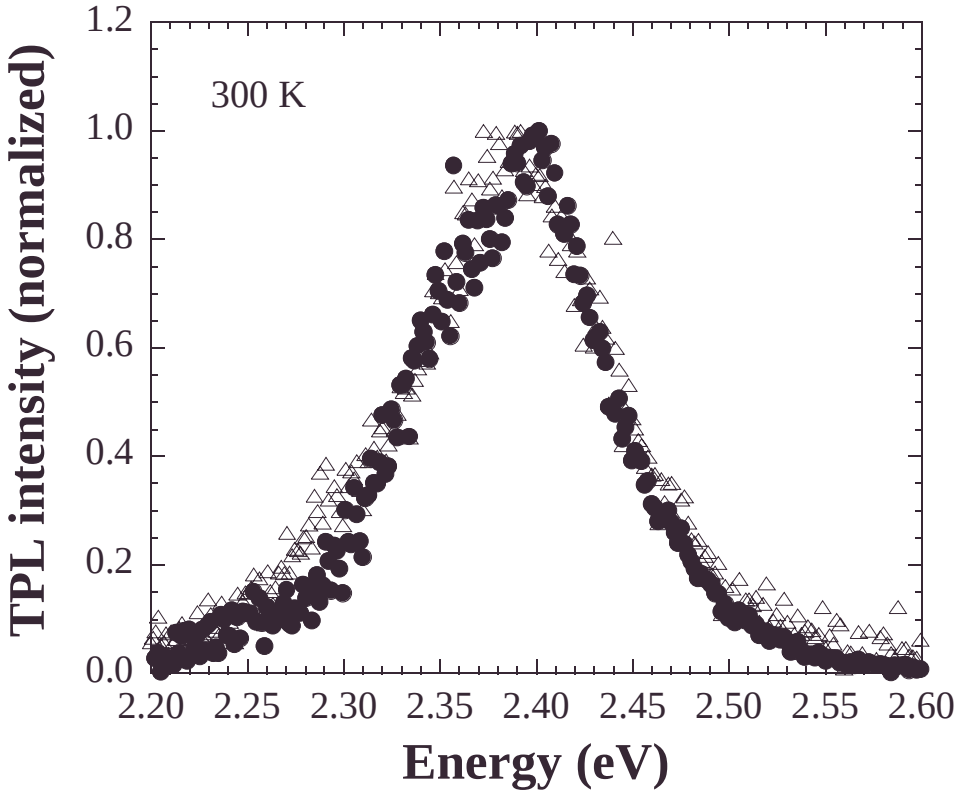

Figure 63: Comparison of the TPL in transmission geometry and the theoretically shifted TPL in reflection geometry.
The TPL spectrum in transmission geometry is shown unaltered as in Figure 62, using open triangle symbols. The TPL in reflection geometry from Figure 62 – solid circles – is shifted using Equation (4-15). The excellent overlap of the two curves is a proof that the shift in transmission geometry is described by Equation (4-15).

The two experimental curves in Figure 63 lie exactly on top of each other, proving the point that the shift in luminescence is entirely due to increased intragap absorption. Thus, we have shown that by means of two-photon excitation and measurement of the subsequent

luminescence, we can probe the CdS/glass interface quality, and it is possible to give some quantitative analysis of the increased absorption at the interface. It should be noted at this point that this analysis is of course not limited to CdS deposited with PLD on glass substrate. Impurity absorption at interfaces is not uncommon in today's thin film technology, except for when some form of epitaxy is used as deposition process. Knowledge of these parameters and fine tuning deposition techniques to minimize interface influences on the device performance has become a very important task for application optimizations, and this method certainly supports this effort.

4.5 Bandgap Shrinkage Observed in CdS Deposited with Spray-Pyrolysis

The CdS:Cu film investigated in this section of the thesis was prepared as outlined in 4.2.2 or in ref. [109]. It was 10 μm thick, and polished to achieve optical quality of the surface.

Please excuse the upcoming rambling, as it deviates from the style of the previous sections. No valuable measurements ever coming from sheer luck or chance, no matter what other people may believe. Published papers, and the results of this section were published in the journal "Semiconductor Science and Technology", are the result of an idea, an outline, the experiment, and the discussion afterwards. Period. The relative amount of time spent on each part can vary, however, and this may give the impression that something happened by chance. These results are a consequence of the two-photon excited photoluminescence measurements on PLD CdS in 4.3.1 , and my advisor Dr. Ullrich suggested we should look into a few other CdS samples to see if the emission is comparable. Well, in fact, the emission of CdS deposited by spray-pyrolysis were excellent, and additionally we were able to detect strong optically induced carrier doping, as seen by bandgap shrinkage.

It was already mentioned that PLD CdS has outstanding film qualities, however from a point of view of the thin film deposition cost, spray-pyrolysis is a very interesting alternative if the sample quality is somewhat comparable to that of PLD CdS. Also, spray-pyrolysis is a very interesting candidate for large area deposition of thin films, similar as it is devised now for organic films and spin coating. In that regard, this deposition technique could become very interesting for solar cells, for example.[110]

The photoluminescence properties of the spray-pyrolysis CdS:Cu (henceforward just CdS) were studied both under single photon excitation (457 nm of an Ar+ laser) and two-photon excitation (805 nm of the Ti:Sapphire femtosecond laser). The luminescence under two-photon excitation is especially impressive, as it shows a very strong green gap emission, and is shown below in Figure 64. The CCD camera with which the picture was taken reacts very strongly to the laser illumination of 805 nm, which can be seen as white illumination in the picture. To properly visualize the green emission, a high pass filter was used separate the laser and sample emission.

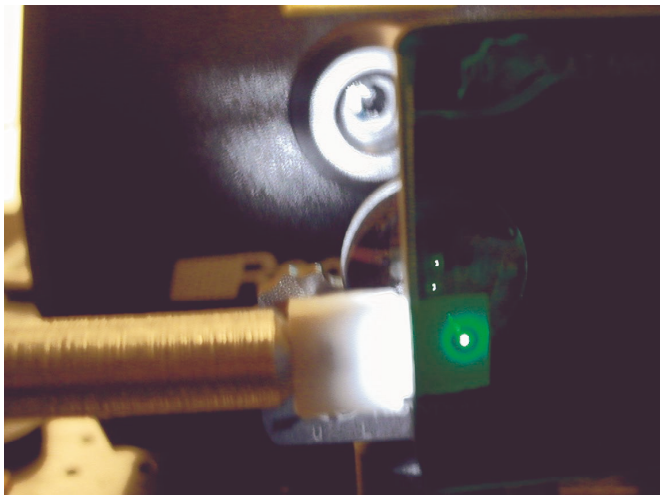

Figure 64: Photoluminescence of spray-pyrolysis CdS, excited by two-photon absorption.
The strong white illumination at the sample holder stems from infrared saturation of the digital camera's charge coupled device (CCD). Therefore, an appropriate subtractive filter was used to keep the CCD sensitive to the green emission.

4.5.1 Photoluminescence measurements

The main difference between single photon excited and two-photon excited photoluminescence is the penetration depth, as was briefly mentioned before. While the photons with energies above 2.45 eV are strongly absorbed with a penetration depth of $d = \frac{1}{\alpha}$, or $d < 10^{-5}$ cm, a similarly defined penetration depth for two-photon excitation, as outlined in Equation (4-14) is higher by 2 – 3 orders of magnitude. Therefore, the photoluminescence shown in Figure 65, excited by two-photon absorption, shows the bulk luminescence of CdS, which is clearly gap emission. Figure 66, however, depicts photoluminescence due to an Ar+ laser (457 nm line) excitation, and both intragap emission (impurity, mostly at the surface or interface) and gap luminescence. Figure 66 also shows a large shift between the photoluminescence measured in reflection and transmission (c.f. Figure 60), which is due to the self absorption of the photoluminescence in the sample, where the emitted photon are only absorbed for around 100 nm in the reflection geometry, but ten times as much in the transmission geometry, causing the shift to the lower energies. In the two-photon excited photoluminescence, Figure 65, no shift is seen due to the homogeneous illumination of the sample. Contrary to Section 4.4 , where PLD CdS showed a shift between the transmission and reflection geometry in the two-photon excited luminescence due to an increased absorption at the interface, there are no indication of any asymmetries in the spray-pyrolysis CdS device.

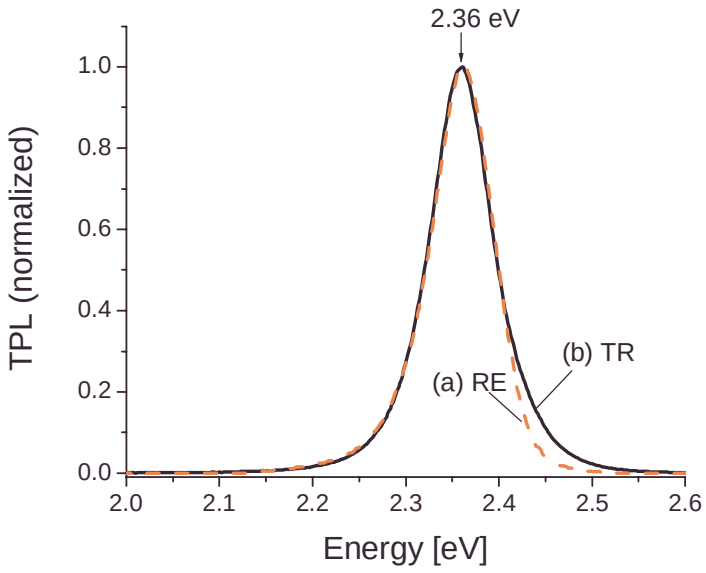

Figure 65: TPL spectra measured in (a) RE and (b) TR geometry. The spectrum is measured at an intensity of 200 GW/cm². The TPL emission intensity is normalized to one at the peak of the band-gap luminescence.

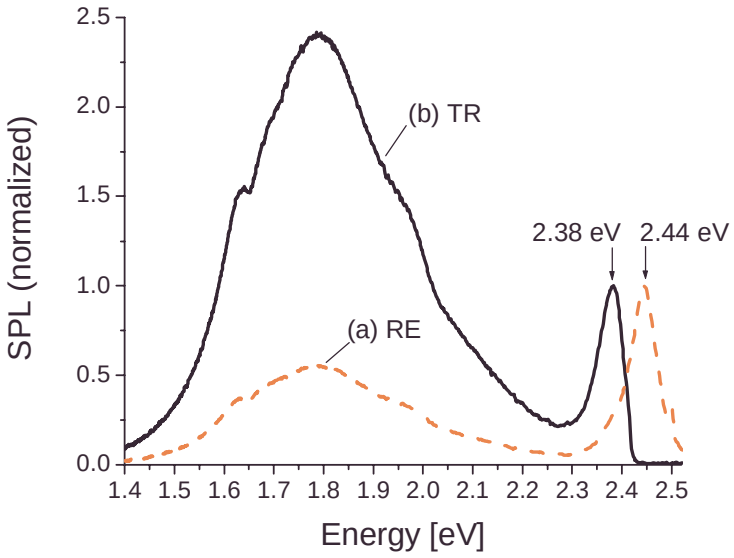

Figure 66: SPL spectra measured in (a) RE and (b) TR geometry. The SPL emission intensity is normalized to one at the peak of the band-gap photoluminescence.

4.5.2 Bandgap shrinkage

Additionally, the position of the emission peak in Figure 65 depends on the impinging intensity of the laser. This shift of the emission to lower energies at high intensities can be explained by the fact that the high number of electron hole pairs induced by optical absorption are better at shielding the repulsive forces between equal charges. Thus, the energy of the electrons in the bandstructure is lowered, and the energy of the holes is raised, which incurs the effect of bandgap shrinkage.[99]

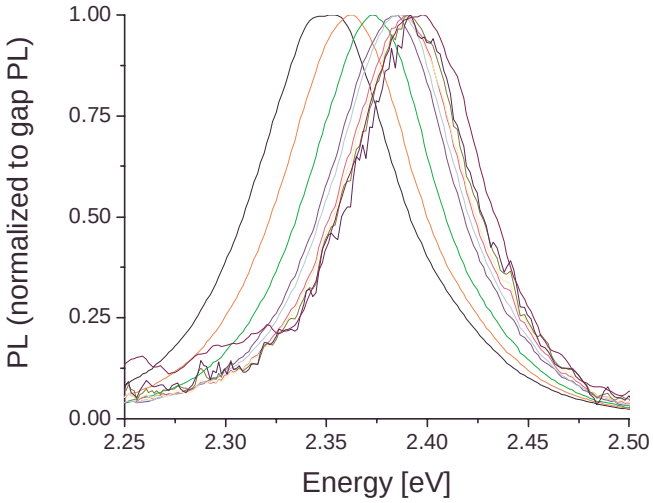

Figure 67: Emission peak positions of spray-pyrolysis CdS:Cu
Left most spectrum (lowest energy emission peak) was taken at 200 GW cm^{-2}, right most spectrum (highest energy emission peak) was taken at 7 GW cm^{-2}.

This also explains neatly why the emission peak of the TPL lies at a lower energy than that of the SPL in TR geometry, which would not be expected by the effects of self-absorption. However, since the excitation density in the two-photon absorption is much higher than in the single photon absorption, the bandgap shrinkage further lowers the emission peak of the TPL.

In Figure 68, the energy shift plotted vs. the impinging intensity is shown. The dependence of the energy shift with the incident intensity is clearly linear. In fact, this is the expected behavior for the Debye screening induced bandgap shrinkage.[99]

At zero intensity, the emission peak is found to be 2.396 eV, which corresponds to the band-gap energy of the integrated bulk emission of the film. The energy difference to the peak of curve (a) in Figure 66 at 2.44 eV is caused by self-absorption, since the reflection SPL barely penetrates the sample, whereas the TPL is present in the entire sample. The band-gap renormalization is expressed in terms of the Debye screening radius,

$$\Delta E_g = -\frac{q^3\sqrt{n}}{4\pi(\varepsilon\varepsilon_0)^{3/2}\sqrt{kT_c}} \quad (2)$$

where, q is the elementary charge, n is the excited electron density, ε is the permittivity of CdS (=8.9), ε_0 is the permittivity of the vacuum, k is the Boltzmann constant and T_c the carrier temperature.

Theoretical analysis of the PL features of thin film CdS according to the principle of detailed balance has shown that for highly excited samples $kT_c \approx 40$ meV [15]. With equation (2) and $n \propto \beta I^2$, it follows for the band-gap narrowing due to two-photon photo doping,

$$\Delta E_g \propto -\sqrt{\beta} \times I. \quad (3)$$

Figure 68 demonstrates the band-gap decreases according to the relation (3) and the single line linear dependence on the intensity indicates that the intensity dependence of β does not play an essential role for band-gap narrowing and seems to be set aside by the many-body effects. By rewriting equation (2), we find the excited electron density,

$$n = 16\pi^2 q^{-6} (\Delta E_g)^2 (\varepsilon\varepsilon_0)^3 kT_c. \quad (4)$$

For the complete band-gap shrinkage, i.e., ΔE_g=2.396 eV-2.349 eV=0.047 eV in Figure 68, we find n=1.6×10^{18} cm^{-3}. It is of interest to compare this value with the number of generated electrons per pulse, which is expressed by,[111]

$$G_{pulse} = \frac{E_{pulse}(1-T)}{2E_{photon}V}, \quad (5)$$

where E_{pulse} is the pulse energy (=1μJ), T is the transmittance of the film (=0.3), E_{photon} is the energy of the femtosecond excitation (=1.54 eV) and V is the excited volume (=7.9×10^{-14} m^3).

We find G=1.8×10^{19} cm^{-3} per pulse. It makes sense that this number exceeds the result of equation (4) since one cannot expect that all electrons excited per pulse contribute to the screening process within a time scale as short as 200 fs. As a consequence, the excited electron concentration found with the Debye formula corresponds to a steady state value representing the equilibrium concentration for the applied repetition rate, pulse duration and lifetime of the electrons.

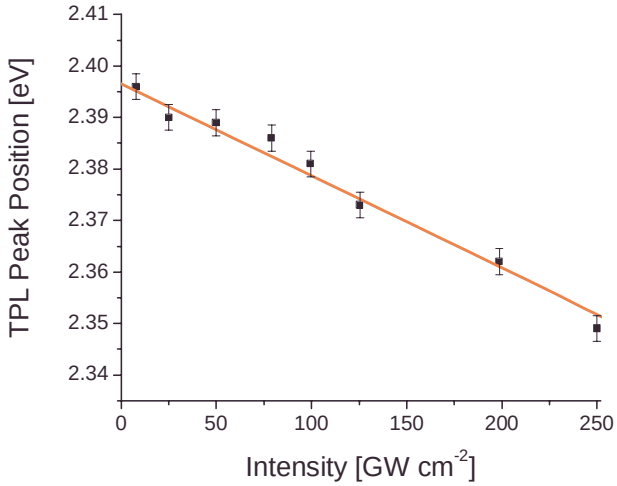

Figure 68: Bandgap shrinkage: TPL peak position versus impinging intensity.

Chapter 4

Chapter 5

INORGANIC/ORGANIC HYBRID SEMICONDUCTOR JUNCTION DEVICES

We haven't the money, so we've got to think.

Ernest Rutherford

5.1 Motivation for Organic/Inorganic Hybrid Solar Cells

Solar power conversion with photovoltaic devices is one of the most important research areas to eliminate energy shortage and pollution problems in the future. Currently, inorganic semiconductors are the main player in this field, with power conversion efficiencies of about 10% for reasonably priced commercially available cells, typically based on amorphous silicon.[112] For multi-junction inorganic devices, efficiencies are reaching and exceeding 25%.[113,114] However, high quality, high efficiency solar cells based on inorganic multi-junction devices are difficult and expensive to manufacture. Additionally, semiconductors with very different bandgap energies, and therefore very different spectral sensitivities, as it is required for highly efficient solar cells,[115] are not easily manufactured in a multi-layer setup, and therefore the choice of suitable materials is restricted.

Organic semiconductors, however, offer the advantage of tunable optical gaps, and relative ease of film forming, which makes devices cheap to produce, which could be crucial to breakthroughs in the solar cell production industry. Efficiencies, however, are limited by low conductivities and especially by the formation of excitons, which limit the charge collection to the interface area. Still, simple heterojunction devices achieve power conversion efficiencies of around 1%,[116] and advanced designs with larger interface areas between donors and acceptors reach efficiencies of up to 5%.[19-22] Recently, the conductivity has been raised in organic crystals, and efficiencies are increased as a result even for simple device geometries.[117]

Recently, efforts have been begun to combine the desired properties of inorganic and organic layers in hybrid devices. Although research has been focused on the development of hybrid light emitting devices,[118,119] the general physical properties of hybrid devices have been studied as well.[120-122] Hybrid photovoltaic devices, however, have not been studied as much in recent years.

In this section of the thesis, we study the photovoltaic properties of hybrid devices based on cadmium sulfide (CdS) and a diisoquinoline perrylene derivate, DQP. CdS is desposited by

pulsed laser deposition (PLD), a simple and inexpensive technique that allows the formation of extremely high quality films, nonetheless.[123,124] The film formation of CdS by PLD can occur on any kind of substrate, be it glass, plastic, ITO, or even another semiconductor layer. DQP can be deposited from solution with toluene as a solvent, by spincoating, or evaporation, and can be formed on a variety of substrates. Due to the inherent flexibility of both deposition techniques, a variety of device geometries are technically possible as seen in Figure 69 below:

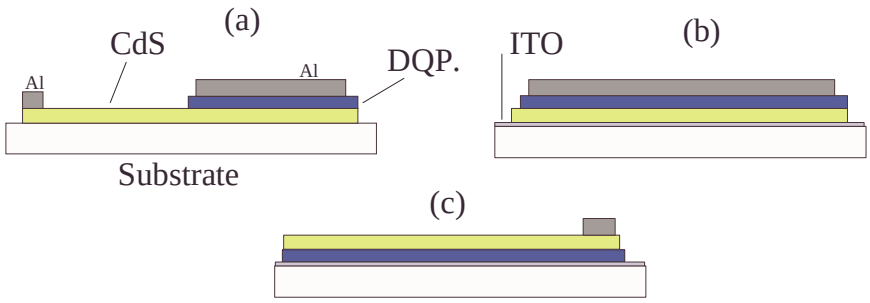

Figure 69: Possible device geometries for hybrid devices.
(a) Two backside electrodes – Advantage: any substrate, (b) sandwich device – Advantage: high built-in field, (c) reverse sandwich device – Advantage: transmits remaining light, good for photovoltaic devices that convert UV light and transmit visible light.

For the results presented in this paper, device geometry (a) has been used.

5.2 Organic and Inorganic Semiconductor Deposition

For the deposition of CdS on glass, a 99.999% pure CdS target was excited with the 355 nm (3.5 eV) line of a Nd:YAG laser, and the fluence of the laser on the target was 3 J/cm. The substrate was 3 cm away from the target. The resulting polycrystalline CdS film was partly oriented with the c-axis perpendicular to surface, partly with the c-axis parallel to the surface. Its thickness was determined to be 1.8 μm by means of transmission spectroscopy. This is the same procedure as described in 4.2.5 .

PLQ (cf. Figure 70) was spincast from a toluene solution at room temperature, with film thicknesses varying up to 50 nm. Film quality on glass or CdS was optically very good. PLQ was also evaporated in a vacuum at 10^{-5} Torr onto CdS, with excellent film quality and thickness exceeding 50 nm.

The photocurrent was measured under the illumination of a 300 W tungsten lamp through a SPEX monochromator and an optical chopper, and the signal was detected with a lock-in amplifier.

Figure 70: Structure of the diisoquinoline perrylene derivative.

5.3 Experimental Results and Discussion

5.3.1 Transmission and photoluminescence measurements

In order to determine if the CdS/DQP device would be suitable for photovoltaic or emissive applications, the transmission spectra and photoluminescence emission spectra were collected. CdS deposited by UV PLD shows very little to no luminescence under single photon (457 nm) excitation, because of the low penetration depth and the fact that the CdS faces have a low optical quality (cf. 4.2.5) and apparently equally bad emission properties in the top and bottom 100 nm of the film. The bulk luminescence, however, is much better as shown by two-photon absorption – together with the absorption spectrum in Figure 71. The emission and absorption of DQP is shown in Figure 72.

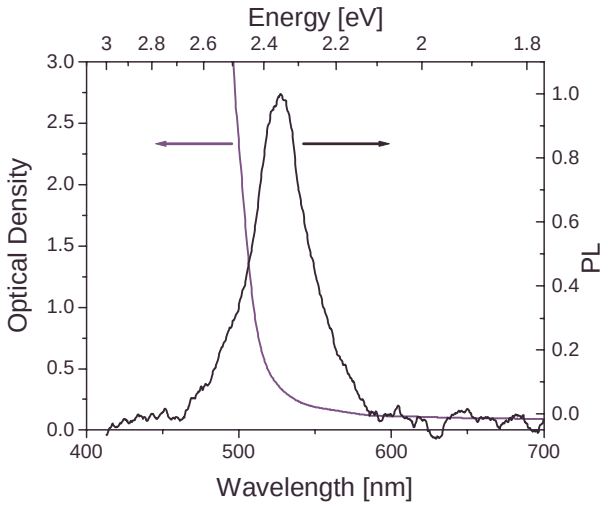

Figure 71: Optical density and photoluminescence spectra of CdS. The photoluminescence emission was excited via two-photon absorption with the 805 nm line of a femtosecond laser system.

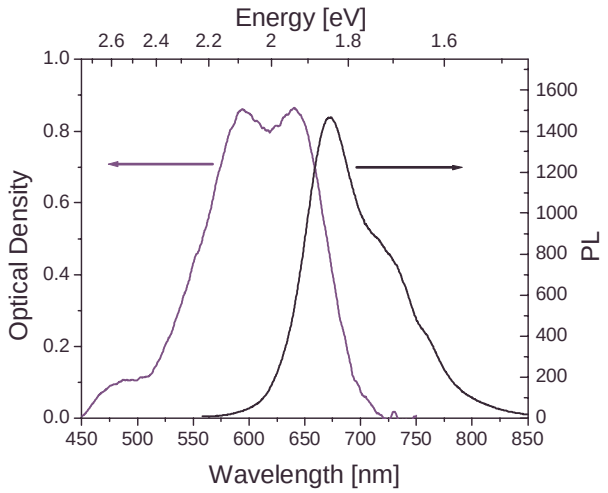

Figure 72: Optical density and photoluminescence spectra of DQP

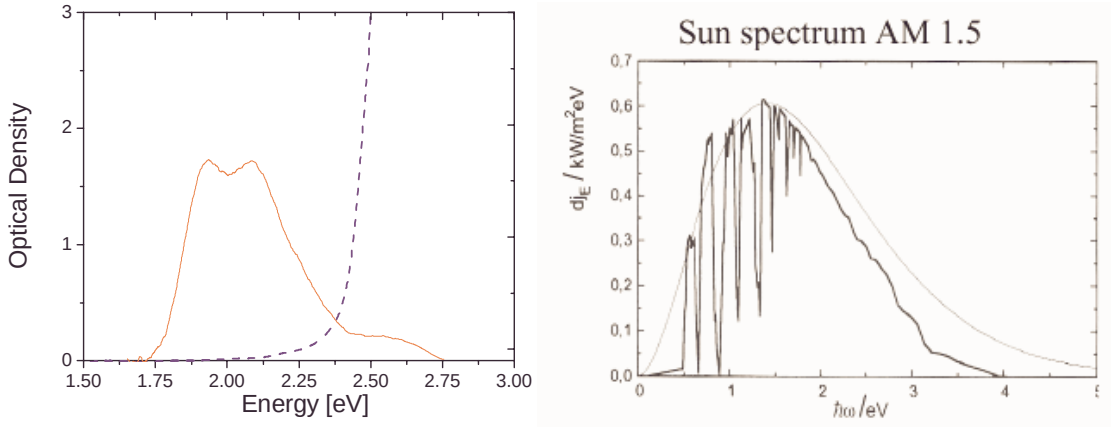

Figure 73: Comparison of the absorption spectra of CdS and DQP, and the solar spectrum under AM1.5 conditions (solid line), or AM0 conditions (dotted, light gray line).[125]

Due to the fact that in an emissive device, most of the radiative recombination comes from the interface, a UV PLD CdS / organic hybrid device most definitely requires a high quality deposition to achieve a significant amount of luminescence efficiency. As a first try, a photovoltaic device seemed to be the more viable path. In Figure 73 the absorption spectra of CdS and DQP are compared, and this combination would absorb a high percentage of the light in the visible spectral range, but none in the infrared above 700 nm, where there is still significant illumination from the sun.

5.3.2 Photocurrent measurements

In Figure 74, the photocurrent of a device is shown where DQP is spincast on top of CdS deposited by PLD. The DQP film did not adhere well on CdS during spincoating, and the thickness of the film was very low, less than 20 nm. Hence, it can be seen that there is only a major photocurrent contribution from CdS, with a peak at 500 nm, which is near the bandgap of CdS. The photocurrent response is low, even low than for a single layer CdS film, and it seems that the DQP film has bad morphology, likely resulting in a low efficiency charge extraction through the aluminum electrode on top of it. The electrodes were biased with a 9V block battery.

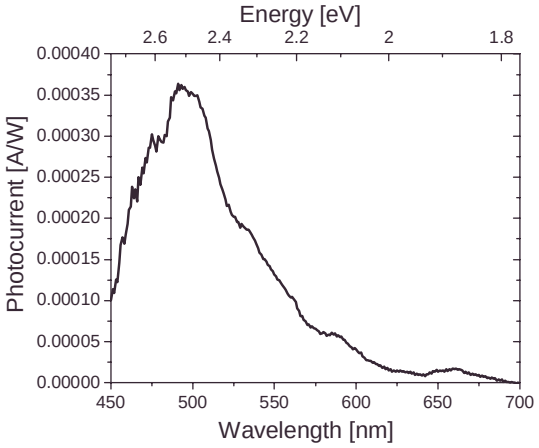

Figure 74: Photocurrent response of a PLD CdS and spincast DQP device.

In Figure 75, the photocurrent response of a device with CdS and evaporated DQP is shown. The film thickness is higher, greater than 60 nm, and both the interface between DQP and CdS as well as DQP and aluminum are of better quality. Figure 75 (a) shows the device under reverse bias, i.e. the electrode on top of CdS is positive, the electrode on DQP is negative, the photocurrent is very good, 0.02 A/W, with a response peak at about 510 nm. The response above 550 nm is still low, although the contribution of DQP is now visible. Apparently, CdS is not a good electron acceptor for DPQ, and the hole mobility in DPQ is limited.

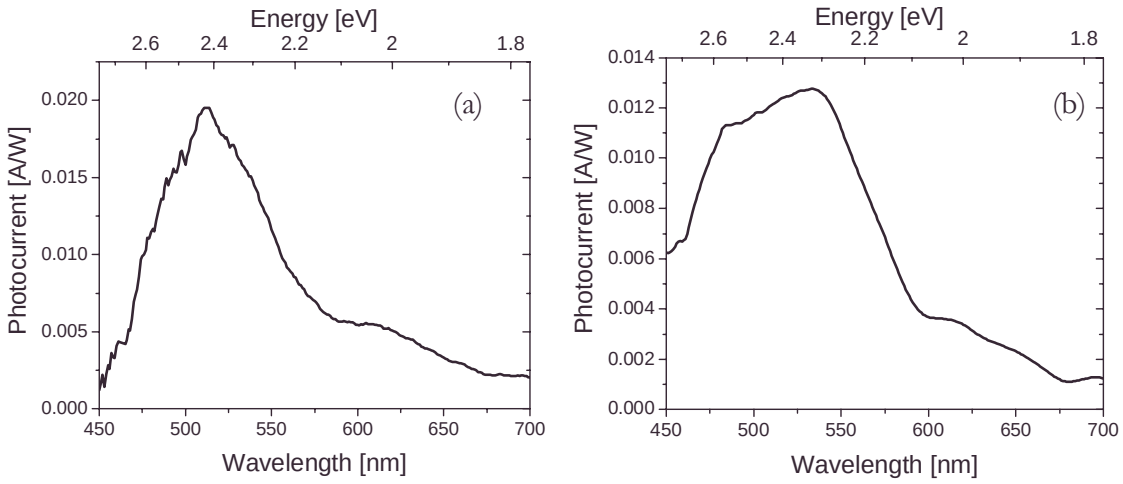

Figure 75: Photocurrent response of a PLD CdS and evaporated DQP device…
(a) … under reverse bias. (b) … under reverse bias

In Figure 75 (b), the same device is shown under forward bias. The photocurrent now has a maximum at 550 nm, which is very close to the peak solar illumination under AM 1.5 conditions. The peak photocurrent response is comparable to the device under reverse bias in Figure 75 (a). The photocurrent shows a response up to 675 nm, where the optical gap of DQP lies; the cell converts most of the visible spectrum into electrical power. From Figure 75 (b) it also appears that electron hole pairs created in DQP by photon below 600 nm (above 2.07 eV) contribute stronger to the photovoltaic response. At the moment, we can only hypothesize about the reason, but it appears that the electron hole pairs created at energies above 2.07 eV either dissociate more readily, or allow for a more efficient charge transfer to CdS.

Chapter 6

VCSEL LAYER PROBING WITH TWO-PHOTON SPECTROSCOPY

Some things have to be believed to be seen.

Ralph Hodgson

6.1 Motivation

Vertical cavity surface-emitting laser (VCSEL) structures have been of increasing importance in the semiconductor laser field, because they offer huge advantages over edge emitting lasers as ease of two-dimensional structured fabrication, circular beam profiles, and dynamic single frequency operation.[126-130] Although they are already commonly used for IR emitting laser applications, the move to visible wavelengths is difficult and has led to strong research efforts in the past years. A promising emitting material for visible red laser emission, such as used for DVDs (Digitial Versatile Discs) is GaInP, which has been studied in detail.[131-137] There are several important properties to be controlled: The reversed band offsets of the sandwiched distributed Bragg reflectors (DBR), optical cavity material and the substrate misalignment, doping profiles are the big challenges from an electronical and crystallographic point of view, respectively.[137]

An important step to master the formation of VCSEL structures is the tight control over the manufacturing processes. With common methods, it is difficult to distinguish advancements in electronic conductivity from better morphological structures leading to higher emission efficiencies. Regular photon spectroscopy has to deal with strong absorption in the DBR and cavity lasers and does not allow sampling of the active layer. Trials of probing the VCSEL structures studied here with laser excitation at 632 nm and 532 nm did not show photoluminescence.

In this paper, we propose the use of two-photon excitation, to quantitatively measure the bulk properties without the influence of electrical properties inherent to a specific production method. The excitation of 804 nm (1.54 eV) is well out of the absorption range of the investigated VCSEL, which is formed by GaInP active layer quantum well, AlGaInP cavity spacers, and AlAs/AlGaAs Bragg mirrors. Two-photon absorption is well suited for measurements penetrating several layers of a sample since the absorption coefficients are smaller and also because the decay of the excitation intensity is not exponential, but goes

with one over the length. Additionally, since the DBR's were tuned to reflect around the VCSEL emission wavelength, the lower energy excitation laser pulses were able to excite the whole sample.

The two-photon excitation was generated by an ultrafast laser system, and as such the excitation is a purely coherent two-photon excitation, that means that two photons are absorbed by one electron at once, and the final state has an even parity to the initial state.

6.2 Description of the Experiment

6.2.1 VCSELs investigated for this thesis

Three different VCSEL structures were analyzed using two-photon absorption. One VCSEL structure (Figure 76, left) was a "mini" VCSEL structure that only features line narrowing. However, due to the smaller number of DBR's – 15.5 pairs on the back-reflector side, 7 pairs on the emission side, not only the main emission of the GaInP active layer could be probed but also characteristic signatures of elements of the cavity and mirrors were sampled. The other two structures (Figure 76, right) have identical numbers of DBR's – 55.5 pairs on the back side, 35 on the emission side, but the cavities are optimized for different wavelengths due to different optical lengths of the cavities. The mini-VCSEL will be referred to as VCSEL 2, the other two as VCSEL 1 and 3. The formation of the VCSEL cells is described in.[137]

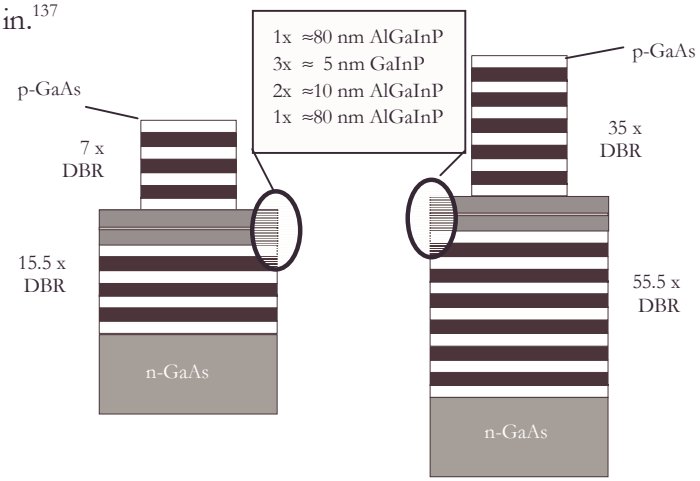

Figure 76: Layer structures of the investigated VCSELs
(a) VCSEL structures with GaInP as the active layer, AlGaInP as the cavity spacers, and AlAs/AlGaAs as Bragg mirrors. Left side: Mini-VCSEL (referred to VCSEL 2 in the text), right side: regular VCSEL structures (referred to VCSEL 1 and 3 in the text). The difference between VCSEL 1 and 3 lies solely in a slightly altered cavity.

6.2.2 Measurement geometries

The samples were excited with a femtosecond laser system consisting of a Coherent Innova Ar^+ laser, which pumps a Coherent Mira Ti-Sapphire oscillator and a Coherent RegA amplifier. The incident laser beam was focused to less than 60 microns in radius. The laser beam has an energy of 2.8 μJ per pulse, a repetition rate of 249 kHz, and a pulse width of approximately 200 fs. Thus, the maximum excitation intensity is 180 GW cm^{-2}. The photon energy of the laser is 1.54 eV (804 nm).

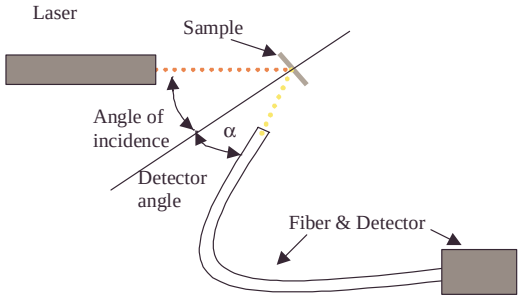

Figure 77: The measurement geometry for the VCSEL photoluminescence experiments.

The photoluminescence of the sample was detected with a 100 μm fiber, which is transmissive in the visible and ultraviolet spectral range and an attached Ocean Optics spectrometer. The measurement geometry is shown in Figure 77. Due to the high reflectivity of the DBR array on the substrate, and the fact the GaAs substrate is highly absorptive in the whole visible region, the active layer emission had to be detected through the lesser reflective top DBR array. The angle of incidence was kept at 30 degrees and the detector angle γ was optimized for the strongest emission of the sample. For the intensity dependent measurements, the laser excitation was attenuated using neutral density filters that were previously calibrated for power throughput.

6.3 Results and Discussion

Except for the GaAs layers (as seen in Figure 76) the whole VCSEL structure does not show single photon absorption for the 1.54 eV laser beam. For two-photon absorption, the change in intensity per space element is

$$\frac{\mathrm{d}I}{\mathrm{d}x} = \alpha_2 I^2, \tag{6-1}$$

where, I *is the intensity and* α_2 *is the two-photon absorption coefficient.*

Integration over the whole thickness leads to the well-known Equation

$$\frac{1}{T} = \alpha_2 I_0 t + 1, \tag{6-2}$$

where, T *is the transmission,* I_0 *is the incident intensity, and* t *is the thickness.*

It has to be noted that Equation (6-2) only holds for constant α_2 – an assumption valid for the intensities used to probe the VCSEL structure presented.

The generated electron-hole pairs per laser pulse are expressed by

$$G_{\text{pulse}} = \frac{E_{\text{pulse}}(1-T)}{2E_{\text{photon}}V}, \tag{6-3}$$

where, E_{pulse} *is the energy per pulse,* E_{photon} *is the energy per single photon,* V *is the excited volume.*

Inserting Equation (6-2) into Equation (6-3) and substituting $E_{\text{pulse}}=I_0\tau_{\text{pulse}}A_{\text{beam}}$ leads to

$$n_{\text{pulse}} = G_{\text{pulse}} = \frac{\tau_{\text{pulse}}A_{\text{beam}}}{2E_{\text{photon}}V}\frac{I_0^2\alpha_2 t}{I_0\alpha_2 t + 1}, \tag{6-4}$$

where, n_{pulse} *is the number of electron-hole pairs created,* τ_{pulse} *is the laser pulse duration, and* A_{beam} *is the area of the laser beam.*

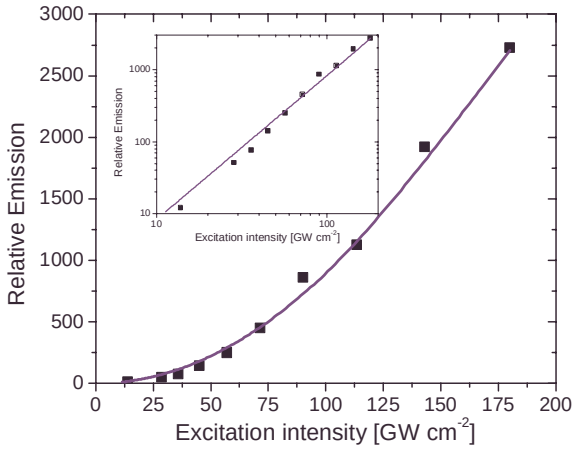

Figure 78: Maximum of the emission intensity of the VCSEL 2 vs. excitation intensity.
The measured intensities are depicted as the full squares; a theoretical quadratic dependence is shown as solid line. The emission is depending on the squared incident intensity, a characteristic for the two-photon excitation. The inset shows the same graph in a double logarithmic scale.

For $I_0\alpha_2 t << 1$, the generation term has a quadratic dependence on the incident intensity, which will be the case for the very thin films in the VCSEL structure. For thicker films or higher excitation intensity, the dependence will be sub-quadratic and finally linear for $I_0\alpha_2 t >> 1$. Hence, with Equation (6-4) it is possible to check the regime in which one is measuring. Figure 78 shows the dependence of the emission of the GaInP active layer with respect to the incident laser intensity. The measured points and the theoretical quadratic dependence curve lie on top of each other. The perfect quadratic dependence and the fact that there are 4 µs between two pulses are strong evidences for coherent two-photon excitation in the regime of $I_0\alpha_2 t << 1$.

Additionally, Equation (6-4) allows the estimation of n_{pulse} for the active GaInP layer. We did not find a α_2 value for GaInP in the literature, however the two-photon absorption coefficient for InP of 9 cm/GW[138] is a good approximation. The top GaAs cladding layer both reflects and absorbs the incident laser beam. The intensity past the cladding layer is ≈ 70% of the incident beam. With $V = A_{beam} \times t$, E_{photon} = 1.54 eV, I_0 = 180 × 0.7 GW cm^{-2}, and $I_0\alpha_2 t << 1$, it follows that $n \geq 10^{19}$ cm^{-3}. This is the number of charge carriers directly after the absorption, which takes place in 200 fs. Since the stimulated emission occurs within the picosecond range, the "effective" number of charge carriers is 1-2 orders of magnitude lower.

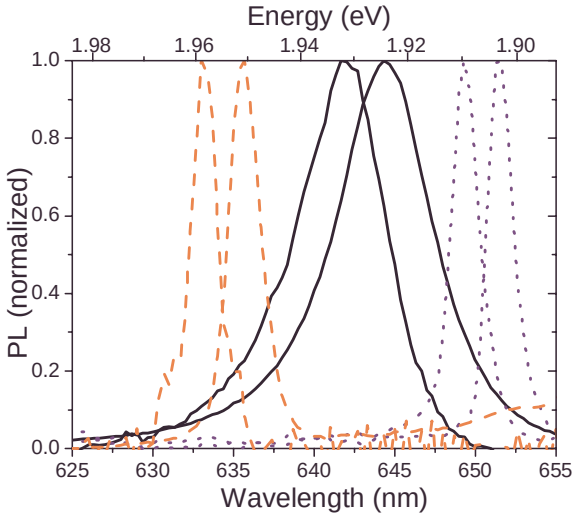

Figure 79: Intensity dependent VCSEL photoluminescence spectra. From left to right: Normalized two-photon excited peak emission of VCSEL 1, 2 and 3 at low (L) intensities (≈10 GW cm^{-2}) and high (H) intensities (≈180 GW cm^{-2}). The VCSEL 2 emission spectra does not show superluminescence but line narrowed emission due to the smaller number of mirror pairs.

In Figure 79, the emission peaks of the GaInP active layers of VCSEL 1, 2, and 3 are shown. The full-width at half maximum (FWHM) is 20 meV (6.5 nm) – line narrowed stimulated emission – for VCSEL 2, the mini-VCSEL with a low number of mirror pairs. The FWHM is only 5 meV (1.8 nm) – lasing – for VCSEL 1 and 3. The reason for the appearance of lasing for VCSEL 1 and 3 is the more than tripled number of DBR mirror pairs. The letter H denotes a high excitation density of 170–180 GW cm^{-2} and L denotes a lower excitation density of 10–15 GW cm^{-2}. It is apparent that all three samples show a shift of the peak photoluminescence as a function of the intensity. The shift appears to be very similar in all three cases.

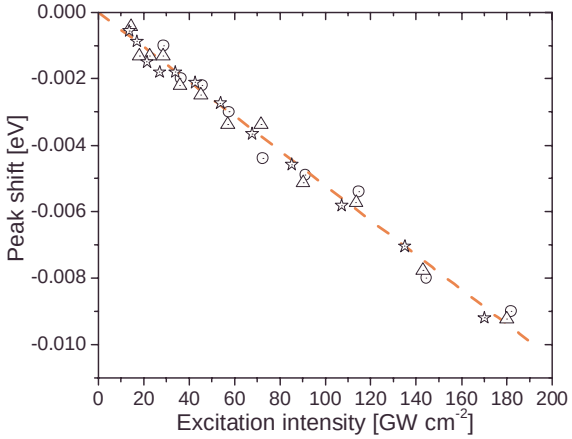

Figure 80: Emission peak wavelengths vs. incident intensity. VCSEL 1 (stars), VCSEL 2 (circles), and VCSEL 3 (triangles). A linear fit describes the bandgap narrowing very well for all three samples.

Figure 80 shows the underlying mathematical proportionality of the relative peak positions for the samples for several different incident intensities. The shift in energy is proportional to the intensity and is directly related to a change in the bandgap of the emissive material. This phenomenon is caused by optically induced bandgap narrowing as observed recently in thin film CdS under comparable experimental conditions.[139] Bandgap narrowing is caused by many-body effects, which are subject to Fermi-repulsion of electrons. In general, bandgap shrinkage is described with the equation below,[99]

$$\Delta E_g = -k \times n^{1/d}, \tag{6-5}$$

where, ΔE_g *is the lowering of the band gap energy,* n *is the effective number of excited charge carriers,* d *is the exponent and can vary from 2 to 6,* k *is a proportionality factor.*

Using Equation (6-4) in the $I_0 \alpha_2 t << 1$ regime and with $V = A_{beam} \times t$, it follows from Equation (6-5)

$$\Delta E_g = -k\left(\frac{\tau_{\text{pulse}}\alpha_2}{2E_{\text{photon}}}\right)^{1/d} I_0^{2/d}. \tag{6-6}$$

Figure 80 follows the model very closely for $d = 2$. The proportionality factor between ΔE_g and I_0 is found via linear regression to be $b = -5.2\times10^{-5}$ eV cm^2/GW, and after correcting for reflection losses of about 30%, $b = -7.4\times10^{-5}$ eV cm^2/GW:

$$b = -k\sqrt{\frac{\tau_{\text{pulse}}\alpha_2}{2E_{\text{photon}}}}. \tag{6-7}$$

From Equation (6-7) k can be estimated: $k \approx 3\times10^{-34}$ J m$^{3/2}$. Since the dimensionality of n was found to be $d = 2$, which corresponds to the case of bandgap narrowing due to coulombic interaction (Debye model), it would be interesting to compare k to the value for the Debye model. The active layer is a quantum well, therefore the Debye model oversimplifies the problem. The proportionality factor is,[99]

$$k = \frac{q^3}{4\pi(\varepsilon\varepsilon_0)^{3/2}\sqrt{k_B T_c}}, \tag{6-8}$$

where, q *is the electron charge,* T_c *is the temperature of the charge carriers,* ε_0 *is the dielectric constant, and* ε *is the dielectric permittivity of the layer.*

The dielectric permittivity for GaInP is 12,[138] and $k_B T_c$ was assumed to be ≥ 25 meV (room temperature). Charge carrier temperatures are typically higher than lattice temperatures, and thus the value given in Equation (6-8) is the lower limit. Charge carrier temperatures are often found to be 370 K to 480 K, or $k_B T_c$ = 30-40 meV.[138,140]

From Equation (6-8), the proportionality factor is calculated to $k \approx 10^{-33}$ J m$^{3/2}$. As expected, this is not a perfect agreement with the value obtained from the experiment and Equation (6-7), and therefore the Debye model is indeed too straightforward to describe the bandgap narrowing accurately in the VCSEL. It is, however, a useful first approximation.

It has been pointed out in ref. [142] that a similar effect of red shifting can occur due to temperature elongation of the cavity. However, in this case the average intensity per second (i.e. cw intensity) is not high enough to heat the sample by several ten degrees, i.e., the necessary value for the observed red shift. Also, as has been noted above, the cavities of the investigated VCSEL's are tuned for different wavelengths, yet the relative shift stays constant. This proves that the bandgap shrinkage of the VCSEL's does not depend on specific cavity features.

To verify whether or not bandgap shrinkage really occurs, we repeated the measurements for the AlGaInP/GaInP cavity on a GaAs buffer without DBR's. Upon evaluations of the photoluminescence, depicted in Fig. 5, two details become apparent: There is a shift to

lower energies for higher intensities, albeit smaller, and the emission is very weak compared to the VCSEL structures. This leads to believe that the presence of the lower-bandgap material GaAs significantly reduces the number of electron-hole pairs in the cavity when not interfaced with several hundred nanometers of DBR's. Judging from the intensity of the emission, a decrease of at least one order of magnitude in the electron-hole pairs is expected. The shift observed in Figure 81 is about 3 meV, which is expected when analyzing Figure 80 for low intensities.

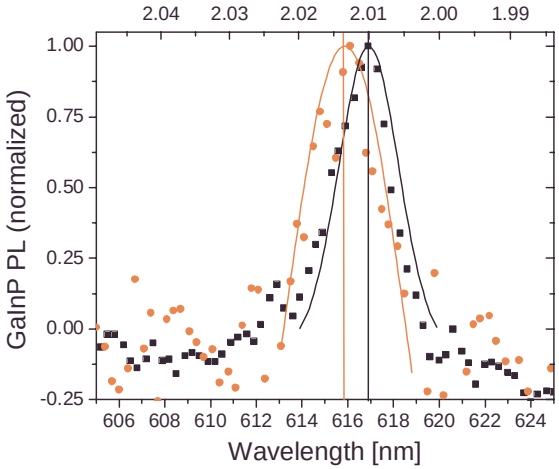

Figure 81: Photoluminescence spectra of an AlGaInP/GaInP cavity without mirrors.
The right curve has been measured with an incident intensity of 215 GW cm^{-2}, the left curve with 54 GW cm^{-2}. The data points have been fitted with a Gaussian theoretical curve to determine the peak position more accurately.

It is important to note that this bandgap narrowing not only occurs for optical pumping, as in this case, but also due to electrical pumping. Therefore, it is essential to keep this shift in mind when designing the VCSEL for the desired emission wavelength.

Apart from GaInP emission from the active quantum wells, emission features from the DBR mirror materials were also measured. The emission peaks are depicted in Figure 82. It is important to determine the peak positions, as they are indicators for the actual bandgap of the mirror materials; it is imperative that the bandgap energies of both mirror materials are substantially higher than the highest energy of the cavity gain curve.

The two emission peaks are located at 546 nm (2.27 eV) and 617 nm (2.01 eV). From Refs., [143,144] the peaks can be assigned to the cavity and mirror layers. For $Al_xGa_{0.5-x}In_{0.5}P$, the bandgap energy is reported as 2.30 – 2.33 for x = 0.25. This corresponds to the emission peak at 2.27 eV. For $Al_xGa_{1-x}As$, the reported values are $E_g = 1.705 + 0.695x$ for the L conduction band minimum, which is the lowest for $x > 0.47$. For the VCSEL structures discussed in this paper, $x = 0.5$, and $E_g = 2.053$ eV (or 604 nm), which is a reasonable

agreement with the photoluminescence peak of 2.01 eV. As such, the respective bandgap energies for $Al_{0.25}Ga_{0.25}In_{0.5}P$ and $Al_{0.5}Ga_{0.5}As$ have been determined to be at a reasonable distance from the highest observed emission energy of GaInP in VCSEL 1, E_{photon} = 1.96 eV, or 632.5 nm.

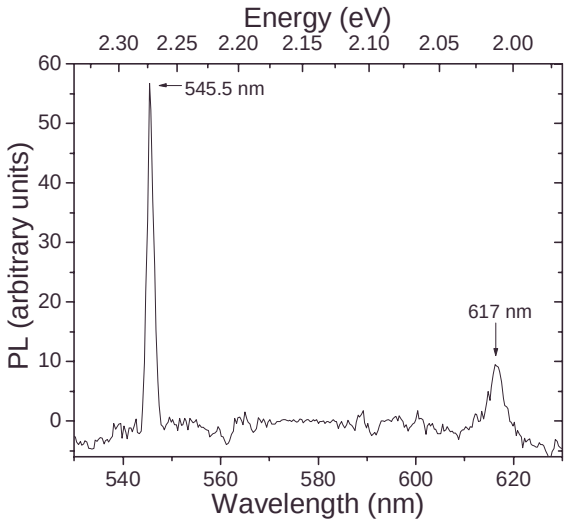

Figure 82: Two-photon excited emission peaks of cavity and DBR's in VCSEL 2.
The left peak at 545.5 nm and 617.0 nm stem from AlGaInP and Al0.5Ga0.5As, respectively.

Chapter 6

Chapter 7

CONCLUSIONS

Prediction is difficult, especially the future.

Niels Bohr

7.1 Conclusions

As has been promised in the introduction and the outline, this thesis has analyzed a range of semiconductors with different methods, and we have found some interesting physics and new theories along the way. I will try to sum it up over the next few paragraphs.

- Through photoluminescence measurements on ISAM devices with low, medium, and high rate of electron acceptor layers, we were able to study the exciton diffusion in PPV, and calculate the exciton separation / charge generation rate for several ISAM devices.
- With two-photon excited photoluminescence, we were able to show that in mLPPP, excitons on the same chain induce non-radiative recombination (intra-chain exciton quenching), whereas the PF2/6 polyfluorene shows no quenching at all. During the derivation of this result, which consisted of fitting the data with equations describing the two-photon absorption and luminescence, we derived a set of equations that describe saturation processes in two-photon processes physically meaningful, as opposed to previous phenomenological approaches in the literature.
- We analyzed the dichroism in laser ablated CdS films, and found that the shift in the photovoltaic spectra, transmission spectra, and photoluminescence spectra to be equal. While it is easy to understand the correlation between photocurrent and transmission, or rather, absorption, the photoluminescence shift shows that that self-absorption is indeed the decisive factor for the emission properties, which leads to the principle of detailed balance (Roosbroeck-Shockley equation).
- Using the Roosbroeck-Shockley equation, in addition to a theoretically calculated absorption spectrum only considering the density of states and Urbach tails, fits the photoluminescence spectra of CdS perfectly when excited by two-photon absorption processes. This is because most of the luminescence in that case comes from the bulk of CdS – with a small impurity concentration – and the different recombination path due to altered symmetries and high excitation.

- In CdS deposited by spray-pryrolysis, we were able to demonstrate that bandgap shrinkage in semiconductors can occur due to not only chemical doping, but also optical doping.
- A CdS and DQP (perrylene derivative) hybrid photovoltaic device was built and measured as a proof of concept study, showing that these two materials have the ability to match the entire visible part of the solar spectrum. Even with non-optimized deposition methods, the photocurrent is considerable. However due to the fact that we used Aluminum for both electrodes, an external bias had to be applied, so no power conversion efficiency can be given at this point.
- Finally, a complex VCSEL structure was studied by means of two-photo excitation, and the photoluminescence signatures of the individual layers were recorded. Again, we were able to find bandgap shrinkage in the GaInP quantum dots at high optical excitations.

In summary, there are actually very different topics covered in this thesis, which may be slightly unusual and may have left the reader with the feeling of lack of continuity, however the spectroscopical methods were a constant throughout the thesis. It was my aim to demonstrate how versatile the simple tools on our hands are, and with them we can unlock powerful secrets in physics.

Obviously, there are many points in this thesis at which one could continue the research where it was left off in this thesis. The future only will tell if this work will be a part in the puzzle to gain more significant knowledge in the future.

APPENDIX A: DESCRIPTION OF KOTTANSPEC

On the following pages, I would like to offer you a short description on the program used to obtain almost all the spectra in this thesis. It took a long time to complete and beta test, but in the end, it was worth it. It was worth it, though, since on the one hand it allows for great freedom and flexibility in the measurements, but at the same time tries to make sure that the parameters are somewhat sane.

1. General description

Kottan Spec is a computer program for scientific measurements in optoelectronics and photonics. The program has been developed with the focus on high flexibility and wide application possibilities.

In fact, the program can be used for photoluminescence, photocurrent, transmission, reflection, and z-scan measurements. For this purpose, the program controls one or two measuring devices and a monochromator or a translation stage. Hence, if necessary, it is possible to measure simultaneously two parameters whereas the combination of the measuring devices is free eligible and does not require specific instruments. The following examples illustrate some of the application possibilities of Kottan Spec.

2. Measuring Spectra

Below, a few examples of spectral measurements are listed. These setups can easily be adjusted for your needs. The aim was to make the measurements desired by the user as numerous as possible.

2.1. Photocurrent measurements

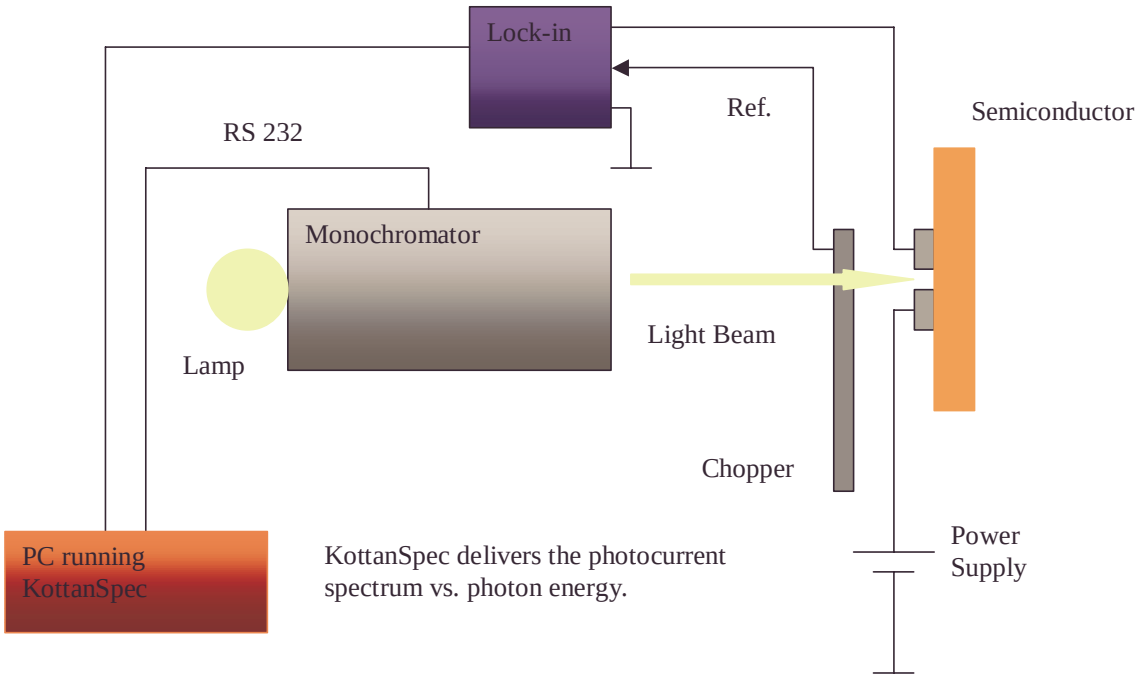

Figure 83 Schematic of the alternate current photocurrent measurements.

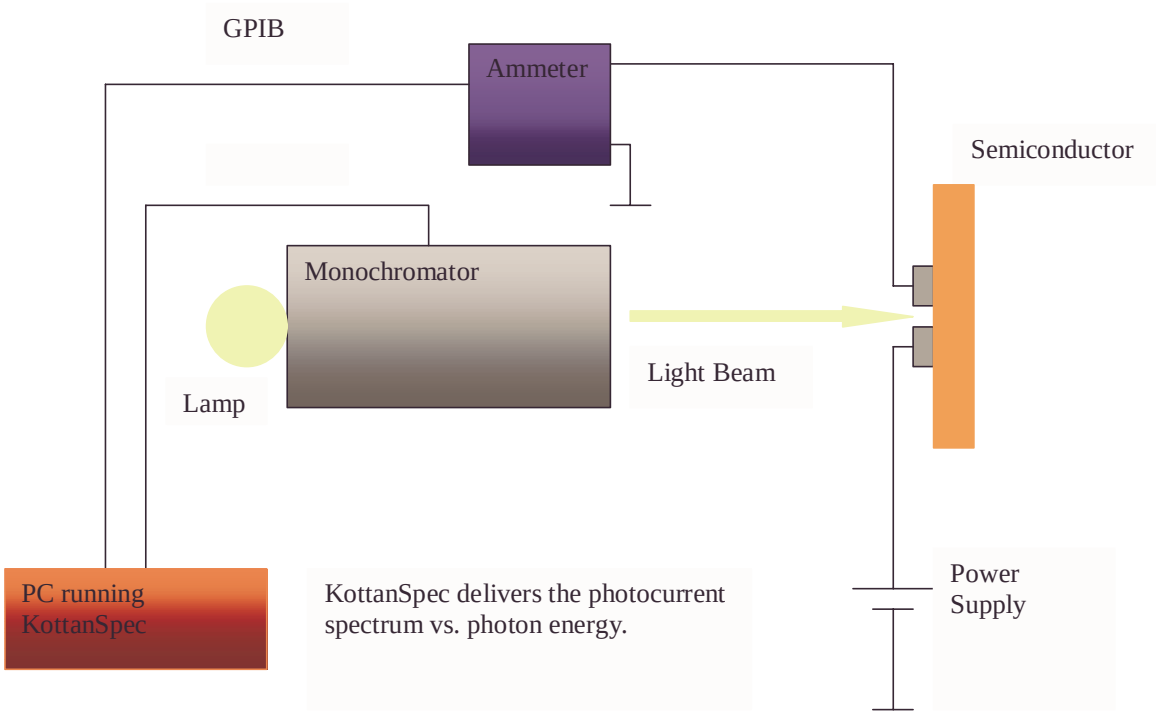

Figure 84 Schematic of the direct current photocurrent measurements

Figure 83 and Figure 84 are examples of a frequently used characterization for semiconductors: photovoltaic or photocurrent measurements. Allowing both alternate current (AC) and direct current (DC) runs is important, considering the different mechanisms in the charge transport and trapping / de-trapping processes when looking at the two methods.[1,2]

In fact, both parameters can be measured at the same time when using an ammeter and lock-in at the same time.

Other measurements, such as measuring the photovoltage spectrum are equally possible.

[1] B. Ullrich et al. "Photoelectric dichroism of oriented thin film CdS fabricated by PLD", *Solid State Comm.* **116**, 33 (2000)

[2] S. Barth and H. Bässler "Intrinsic Photoconduction in PPV-Type Conjugated Polymers", Phys. Rev. B 79, 4445 (1997)

2.2. Transmission and reflection measurements

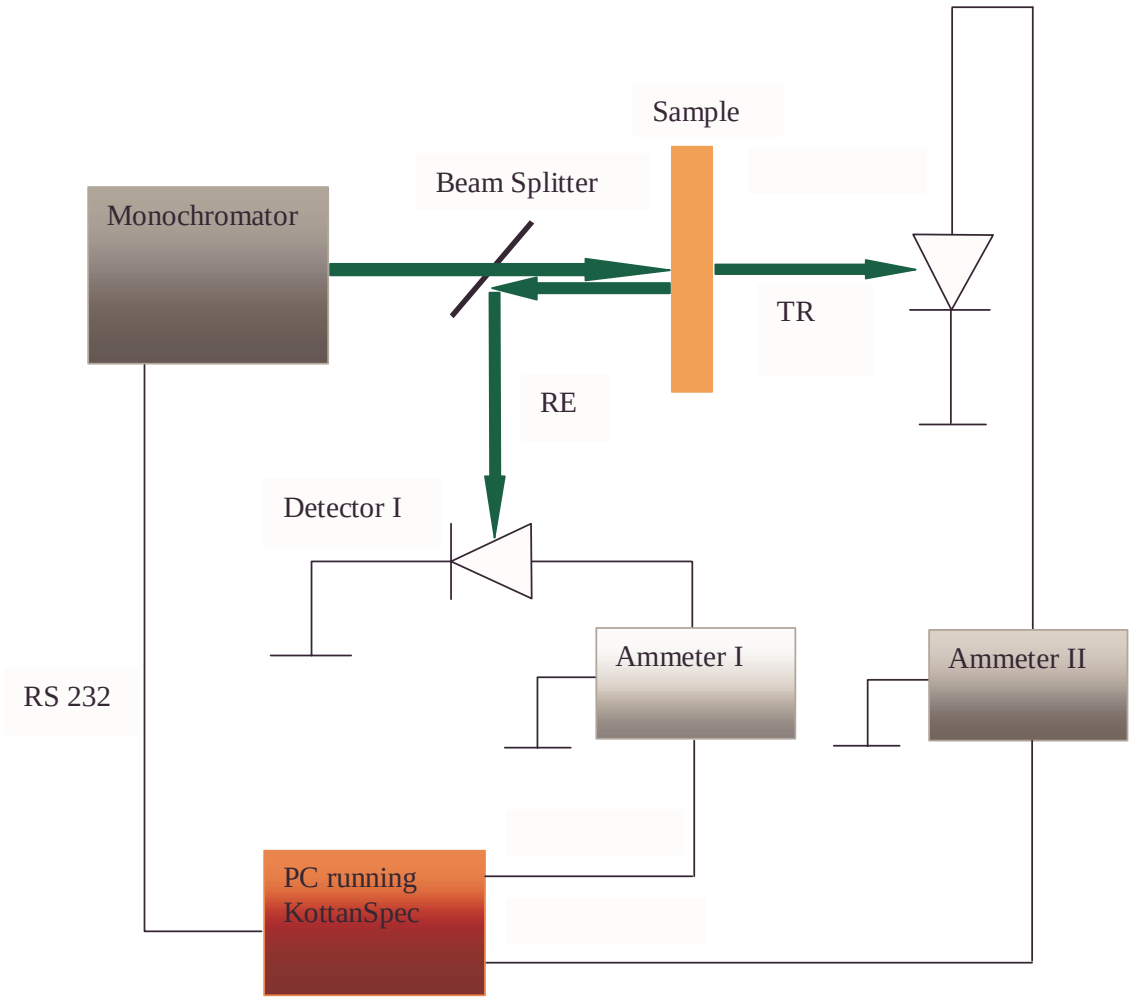

KottanSpec delivers simultaneously transmission and reflection spectra vs. photon energy.

Figure 85 Setup for tramsmission and reflection measurements.

This setup is similar to the one discussed in 2.1. on page 112, but it uses a photodetector (e.g. silicon diode) to measure the light transmitted through and / or reflected from the sample. Although it is not as convenient and simple to use as a commercial transmission spectrometer, it provides more flexibility in characterizing the sample.

Using Kottan Spec

3. Required and supported equipment

3.1. PC hardware requirements

- Intel Pentium I/II/III/IV, AMD K6/Athlon/Duron, or compatible
- 32 MB RAM (64 MB RAM are recommended for NT/2000) – actual memory usage of the program: < 7 MB
- 2 MB free disk space for the program (additional disk space for measured data)
- HP / Agilent SICL compatible GPIB bus card

  OR

  National Instrument NI 488.2 compatible GPIB bus card
- RS 232 cable for monochromator communication: CVI monochromators need a direct link serial cable, SPEX monochromators need a null-modem cable

3.2. PC Software requirements

- Windows 95/98/NT 4.0 SP5/2000. For reasons of stability, NT 4.0 or 2000 are recommended. Windows ME compatibility has NOT been tested.

3.3. Supported measurement equipment

- Any SPEX monochromator control-able via the SPEX232 interface (e.g. 180D, MSD2, 220M, 270M, 1870 series). The software is preset for SPEX 500 monochromator and values need to be adjusted for your monochromator.
- Any CVI monochromator compatible with the CM110 command set.
- Keithley multimeters of the 1xx series. Caution: change of input from voltage to current cannot be remotely controlled and need to be set by hand
- Keithley multimeters of the 2000 series or compatible products
- SRS 530 lockin amplifier. Again, changing from voltage to current measurements requires the user to switch the lock-in manually

- SRS 830 lockin amplifier.
- Keithley picoammeter 485
- Newport stage controller ESP 300

4. Operating Kottan Spec

4.1. Getting started:

Start Kottan Spec by double-clicking its icon on the desktop (or select it from the start menu):

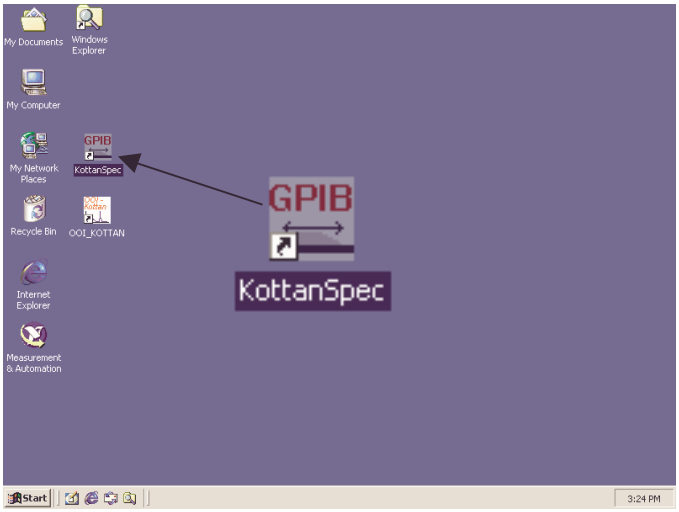

Figure 86 Typical desktop showing Kottan Spec shortcut.

The main program screen will pop up and a dialog will request some information from the user (Figure 87 below). From left to right, top to bottom, the following settings need to be reviewed and possibly adjusted. All settings are stored in the program directory.

- Name of Operator: The name of the operator will be shown in the window, and the data collected by this user will be saved in the sub-folder bearing the same name. The folder in which this sub-folder is stored is determined by the option "Measurement Directory" (see below). Most alphanumeric characters and spaces can be used. The "$" sign should not be used since it represents a space " " in the configuration files. A user has to type in his or her name in the edit field when using Kottan Spec for the first time, later, the arrow button to the right displays all known users for selection.

- GPIB Interface: There are three possible settings. "HP GPIB" refers to any HP or Agilent SICL compatible GPIB cards. "NI GPIB" refers to any National Instruments NI 488.2 compatible GPIB cards. "No GPIB" should be selected if the program is run on a computer without a GPIB card. Saved files can be opened with the program, as well as monochromators can be moved even without a GPIB interface attached.

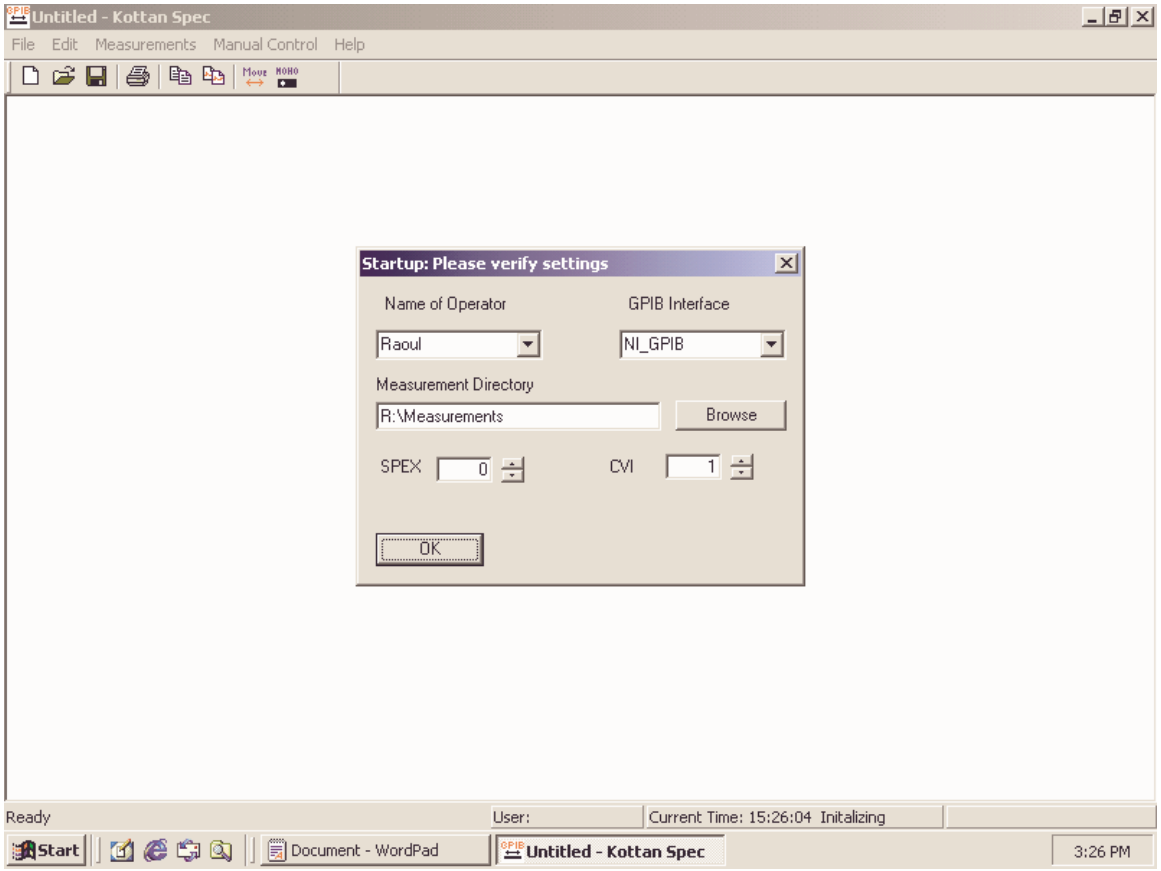

Figure 87 Kottan Spec main window showing the initialization dialog.

Measurement Directory: Enter a Directory or hit "Browse" to select a directory in which the user folders will be placed. This setting only needs to be set the first time the program is run, but can be altered later as well. If the directory does not exist, the program offers to create it. User subfolders will not be moved to any new location. If the current selected user does not have a sub-folder in the selected measurement directory, a new sub-folder will be created as well.

SPEX / CVI: Enter the COM port (serial interface port) to which the monochromators are connected. Typical PCs only have COM 1 and COM 2, which refers to the serial ports on the back of the PC. COM 1 is typically the one closer up higher on a mid tower, COM 2 is the lower one. If either monochromators is not attached to the PC, select 0. Again, these settings only need to be modified the first time Kottan Spec is run, or when a monochromator is added/removed.

Press "OK" after reviewing the selections.

Next, Kottan Spec will start probing the GPIB bus for attached instruments. While it is doing that, it will show an animation saying "Scanning GPIB bus. Please wait – this will take less than one minute" (see Figure 88 below)

Figure 88 Scanning GPIB bus animation.

The actual time it takes to scan depends on a two factors: How many GPIB devices are attached, how many of them are turned on, how many devices are old vs. new.

In general, the SRS 530 and most old unsupported devices will take longest to be detected. Keithley multimeters with the old 1xx command set also take relatively long. New instruments as the Keithley 2000 multimeter or the SRS 830 lock in amplifier will be detected very fast.

It may seem that instead of having a waiting period every time it would be easier to configure the devices by hand, but this way Kottan Spec can be sure that all instruments listed can really be used.

If there is a SPEX monochromator attached, one more dialog will pop up to make sure that it is still at the position when Kottan Spec exited. Also, when used for the first time, two important parameters describing your SPEX monochromator model have to be entered. When you run Kottan Spec for the first time, the following dialog will appear (left side):

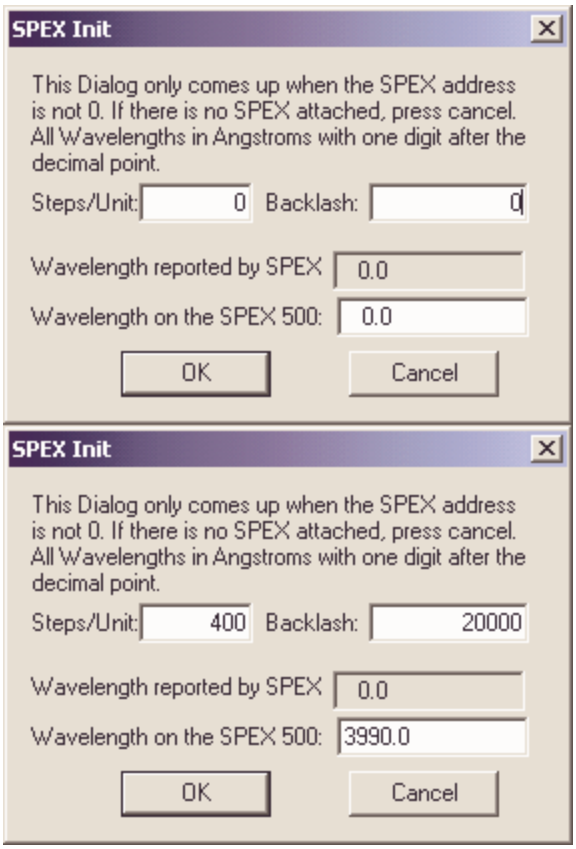

Figure 89 Left side: SPEX Init dialog during first run after installation. Right side: Values entered for a SPEX 500 monochromator, positioned at 3990 A as shown on the side.

When Kottan Spec is run at a later time, the first two fields will be grayed (read only) to make sure that no unauthorized or accidental changes are applied. The dialog will look like this:

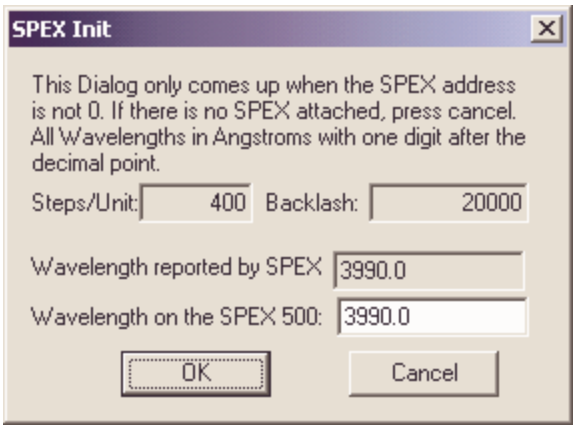

Figure 90 SPEX Init dialog at any time after the first run

Finally, the appearance of the screen in Figure 91 signalizes that the initialization is done and Kottan Spec is fully operational:

This "Stand By" screen shows the attached devices. There are three different messages possible:

Supported Dev(ice): This device has been recognized and is supported by the current version of Kottan Spec.

Unsupported Dev(ice): This device is recognized, but not yet supported by Kottan Spec.

Unknown Dev(ice): This device is neither recognized nor supported.

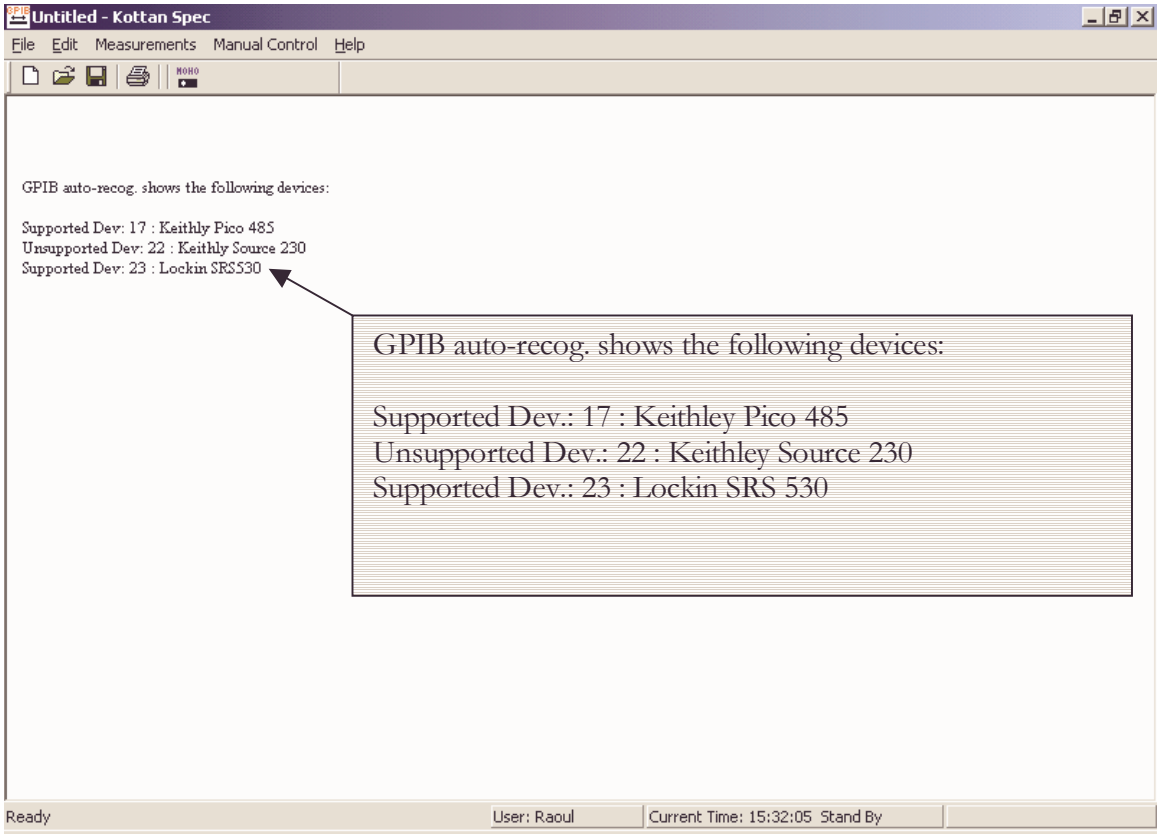

Figure 91 "Stand by" screen after successful initialization.

Both the tool bar and the menu bar will reflect the state of Kottan Spec. Comparing Figure 87 and Figure 91, there are three icons not shown in Figure 91. The two icons showing two sheets on top of each other are used to copy data or images into the clipboard. They will be discussed below. Since there is not data after initial start-up, those icons are hidden. The third hidden icon says "Move" with a double-headed arrow below. This is used to manually move any Newport stages attached. The "Stand By" screen shows that the stage is not connected and therefore this option is hidden as well. However, the user did select a monochromator (Figure 87 above) and therefore the manual monochromator control icon is shown.

4.2. First Steps in Kottan Spec

Kottan Spec allows the direct manipulation of the basic components using the tool bar (shown in Figure 92 below) and the menu bar (Figure 95 below).

Figure 92 Kottan Spec tool bar

The tool bar allows the following commands (from left to right)

- New (clears any measurement from screen)
- Open (opens a previously saved spectrum)
- Save (saves the displayed spectrum prompting for a name)
- Print (prints the current spectrum on a printer)
- Copy data (copies the underlying spreadsheet data to the clipboard) –can be pasted directly into MS Excel or Origin or any spreadsheet prg.
  (Can be accessed from the Edit submenu as well)
- Copy image (copies the current spectrum to the clipboard) – can be pasted into an imaging program or as an image into a text processing program (MS Word or similar word processor)
  (Can be accessed from the Edit submenu as well)
- Move stages (moves and controsl any stages attached to the ESP 300)
- Set monochromator (sets the wavelength on one of the monochr.)
- Stop measurement (stops the current measurement after the recording the current point. The status bar will change from "Running" to "Stand By" as soon as the measurement has stopped.

However, during normal operation, not all the icons will be shown. On the standby screen, for example, the STOP icon will be missing, since there is no measurement running. Examples of this are shown in Figure 93 and Figure 94, where the former shows the state with data loaded (so copy data and image is activate) and stage controller and monochromator attached. The latter shows the state when there is only a monochromator attached and there is no data present.

Figure 93 Toolbar during standby with data recorded or loaded, stage and monochromator attached

Figure 94 Toolbar during standby with no data recorded or loaded, monochromator only attached

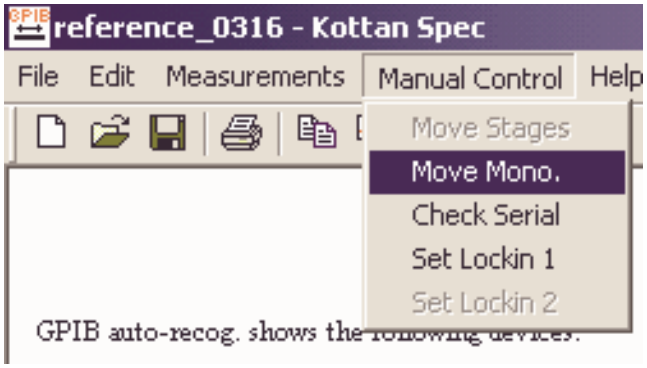

Figure 95 Kottan Spec menu bar – "Manual Control"

The first two menu items in "Manual Control" allows to move stages and set monochromators as for the tool bar icons. "Check Serial" is a diagnostic tool for the serial interfaces and can be helpful for testing if the communication to the monochromator works or not. "Set Lockin" allows to control the most important features of the attached lock-in amplifier(s). As always, options that cannot be used are grayed. "Check Serial" is always enabled to allow monochromator trouble shooting.

The use of the dialogs invoked by the menu items is described in Section 5. on page 125.

4.3. Basic I/O operations

The "File' menu allows to open and save data (see Figure 96). This is possible even when there is no monochromator or GPIB card attached. It should be noted that all measurements are saved during the measurement in any case, so "Save" and "Save As" will be used very rarely. Recently opened and saved files also show up in the "Recent" list at the bottom.

Print will print the currently displayed graph to any attached printer / network printer. The curves are solid, dashed, and dotted to be discernible if printed to a B/W printer.

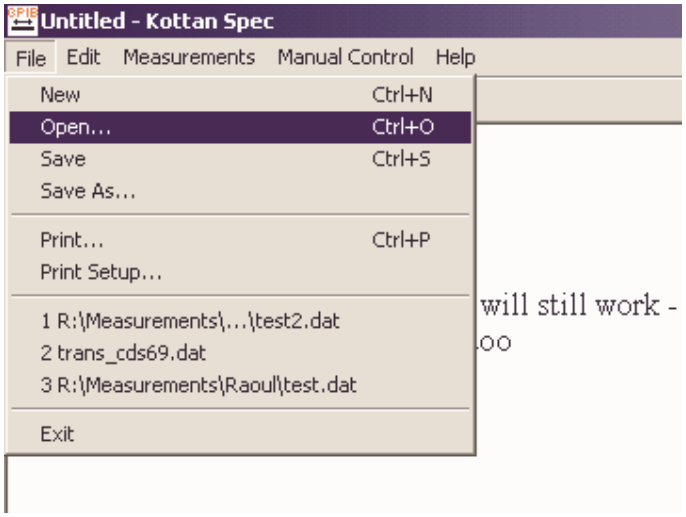

Figure 96 The "File" menu

The "Edit" menu allows to copy the currently shown data either numerically, to be pasted into a spreadsheet program, or as an image. "Copy Data" takes the data and posts it to the clipboard in the usual format, which has tabs between the columns and carriage return/line feed at the end of the line. For most spreadsheet programs (including MS Excel) only the top left field has to be highlighted when the data is pasted. Some programs, e.g. Microcal Origin, require you to select the number of columns manually. There is a simple rule of thumb to determine the number of columns: 2 + # instruments (+ 3 if one instrument is a lockin). This is the same format used to save the files to disk and will be discussed in further detail.

"Copy Image" copies the current displayed curve as an "Enhanced Meta-File" which can be pasted into almost any Windows program. Since we wanted to keep the resolution as high as possible, direct pasting to MS Word leads to a very large picture. It is recommendable to use "Paste Special" and to select "Picture" when using MS Word.

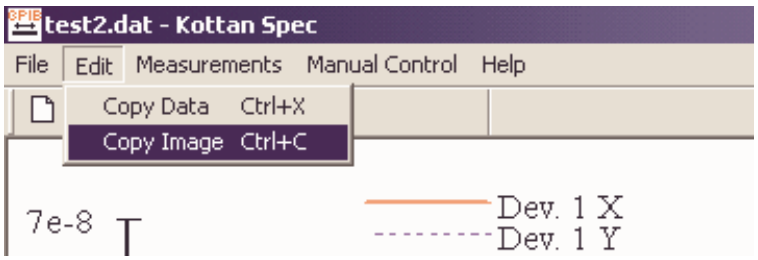

Figure 97 The "Edit" menu

5. Manual control

This section covers the use of the dialogs controlling stages, mono-chromators, lockin amplifiers.

6. Move stages

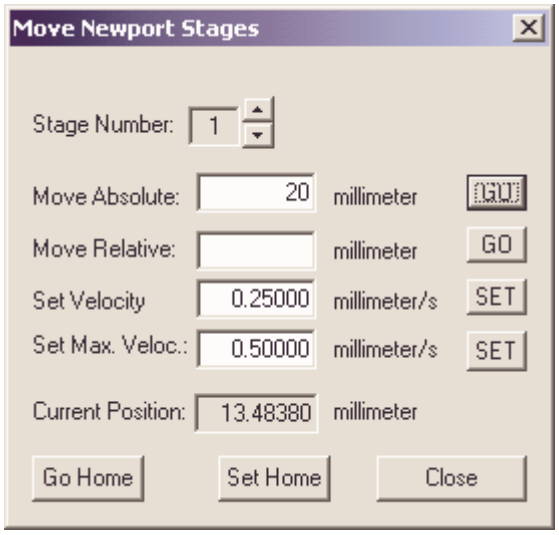

Figure 98 Move stages dialog

- The top arrows allow to set the currently used stage. This value can be anything from 1 to 3, since the ESD 300 allows control of 3 independent stages.

- Move absolute: This moves the stage with the current velocity to the position indicated in the editable box. The position can be positive or negative (zero indicates the current home position). Clicking "Go" will start the movement. Note: The movement will only start once the stage has stopped any previous movement.
- Move relative: Same as above, but the current position indicates zero, so a negative number moves the stage left, a positive number will move it to the right.
- Set Velocity: This value sets the velocity of movement. This value is not used for a "Go Home" command. It cannot exceed the maximum velocity.
- Set Max. Velocity: This is the upper value for any velocity. It is used for a "Go Home" command.

Advice 7.1.a – CAUTION: It is possible to set the velocity higher than recommendable for the stage. Since it is impossible to determine the maximum allowable speed of a stage, the user MUST make sure that the value is acceptable. As a general rule, 0.2 mm/s is acceptable even for high resolution newport stages. The author and/or distributor cannot be held accountable for misuse of the velocity option.

- Go Home: This moves the stage to the currently defined home position (0 absolute)
- Set Home: Sets the current position as home (0 absolute)

6.1. Move monochromators

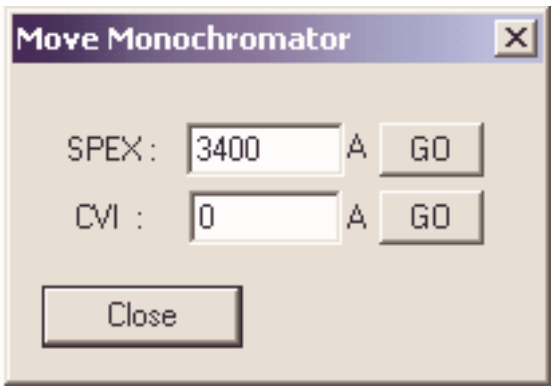

Figure 99 Move monchromators dialog

This will move the monochromators to the desired position in angstroms (Å, 10^{-10} m). If either monochromator is not attached, pressing "GO" for the unconnected monochromator will not invoke any reaction.

If the SPEX monochromator is selected to move to a wavelength lower than the current wavelength, Kottan Spec will perform an automatic "backlash", that means it will overshoot to a lower wavelength and then move back slowly to the correct wavelength. Due to the specifics of this operation, the dialog will not accept any user input until the monochromator has executed the backlash. If the change of wavelength is less than 500 Å, the backlash will not be performed.

> Advice 7.1.b – CAUTION: The lowest position in this dialog is zero, corresponding to the zeroth order (full transmission of the monochromator). The highest possible wavelength is defined by the grating, and the user has to make sure not to issue movements to wavelengths higher than the maximum possible. Most monochromators will turn off movement automatically after having reached the maximum wavelength – still, it is important to not exceed monochromator specifications. Please consult your monochromator manual.

6.2. Set lockin amplifier

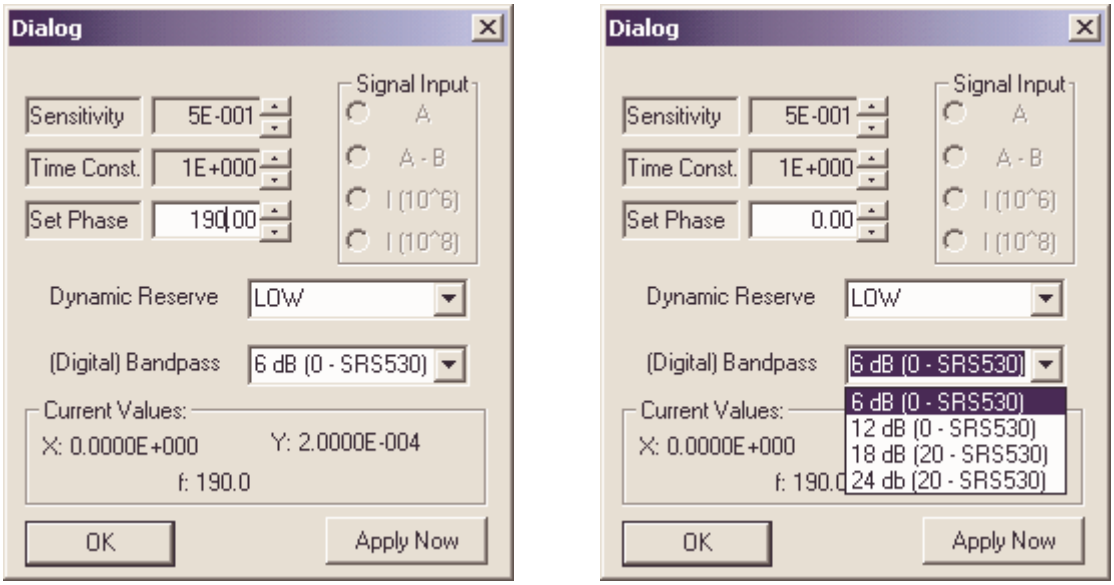

Figure 100 Left Side: Set lockin dialog. Right Side: Different bandpass filter options for the SRS 830 (left values) and the SRS 530 (right values).

This dialog allows the control of the most commonly used features of the SRS lockin amplifier series. The sensitivity and the time constant can be scrolled through with the arrows. The phase can be entered in the dialog, or be changed in 90 deg steps by pushing the arrow buttons.

The field signal input is disabled for the SRS 530, since it cannot actually set these options. The SRS 830, however, allows full control of the input.

An important difference is made in the (Digital) Bandpass field. The SRS 830 DSP lockin has a digital bandpass filter that allows four different settings (8, 12, 18, 24) as shown on the right hand side of Figure 100 above. The SRS 530 has an electronic bandpass of 20 dB, which can be selected, or removed – yielding a 0 dB "bandpass".

Dynamic Reserve: It has to be noted that most lockin amplifiers do not allow all dynamic reserve settings at all sensitivities – thus Kottan Spec may appear to not "allow" a certain setting. Please refer to your lockin amplifier manual.

Below that, the current values of the x channel and y channel along with the current reference frequency are shown. These values will be reread when changes are applied, or the "Update" button is pressed.

7. Measurements

A new measurement is always initiated by selecting the desired type of measurement in the "Measurements" menu, as shown in Figure 101. The number of types listed here may be higher than documented here. Any selections not mentioned in this manual will be discussed in the readme file.

Clicking on "Stop Measurements" invokes the same behavior as clicking the stop sign in the toolbar. Menu items that are grayed indicate the a necessary device is not attached – e.g. a stage controller for Z-Scan measurements, or a monochromator for Spectral measurements.

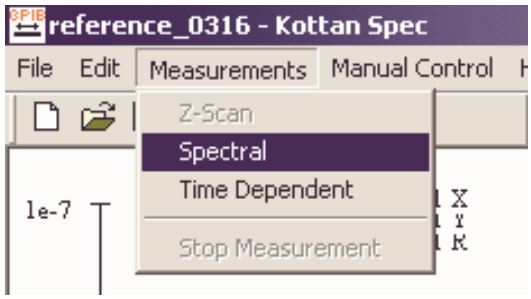

Figure 101 The "Measurements" menu

7.1. Spectral Measurements

Spectral measurements is a summary term for any measurement that requires spectrally selected light and measures the response of a system using one or two detectors. Examples would be transmission/reflection measurements, as well as photocurrent measurements.

Using this kind of measurement as an example, the dialog to select the desired program behavior will be discussed in this section.

After selecting "Measurements" – "Spectral" as shown in Figure 101 above, the following dialog will pop up:

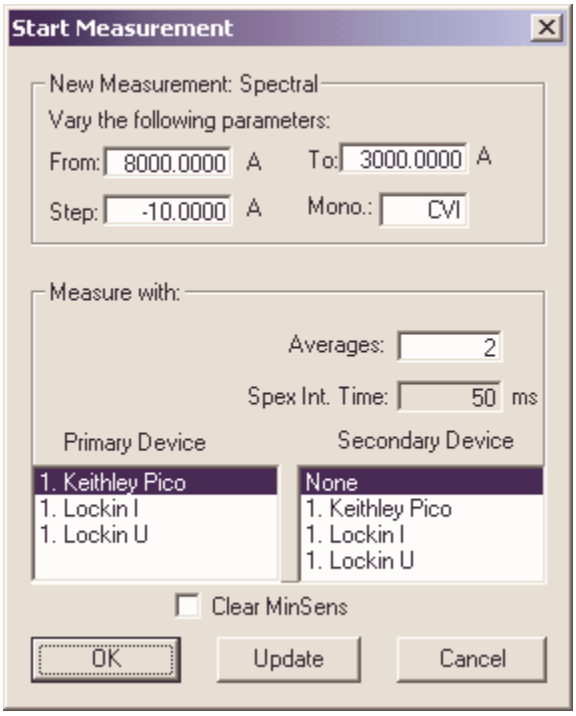

Figure 102 Start measurement dialog "Spectral"

In general, the top part will contain the section of which parameters will be varied, in this case, of course, that is the wavelength, given in Angstrom. It is typically best to scan from low photonic energies (high wavelengths) to high photonic energies (low wavelengths) because it reduces the possibility of measuring artifacts, especially during photocurrent measurements. However, the program can measure in either direction without any problems. If the "From" – "To" fields disagree with the "Step" field, "From" – "To" takes precedence. "Step" will be adjusted automatically "To" be negative if "From" > "To", and positive if "To" > "From". If "Step" is equal to zero, it will be set to ten angstroms – a reasonable setting for most applications.

The "Mono." field shows which monochromator will be used to scan through the wavelengths. It will default to the monochromator that is attached, and if both a CVI and SPEX monochromator is attached, it will default to SPEX. Alternatively, it accepts numeric input, where 1 = SPEX and 2 = CVI.

The second section concerns which instruments measure how. "Averages" signifies how often an instrument is polled for data for one measured point. For two different devices this value represents the minimum guaranteed averages for the faster device. The slower device will always measure at least once.

Example:

A Keithley Picoammeter 485 and the SRS Lockin Amplifier 530 are used as measurement devices, and averages are set to 30.

The fastest mode for the Keithley 485 series allows retrieval of data every 400 ms. This mode is exclusively used in Kottan Spec to allow a maximum number of measurements per unit of time. Thus, 2.5 readings will be taken per second.

The SRS 530 will be allowed to settle for the length of the set time constant (typical settings are 300 ms to 1 s, let's assume 1 s in this example), which is a necessity for accurate readings. Then, each 30 ms a reading will be taken.

In this example, during the acquisition of the first three points, the picoammeter 485 will typically be faster, but after settling, the SRS 530 will outmeasure the picoammeter.

For 30 averages, the SRS 530 will need 1s + 30 * 0.03 s = 1.9 s

During this time, the picoammeter will take 5 averages, since the last, the fifth, reading will be issued after 1.6 s and the program will wait until the last measurement is taken.

It may seem that 5 averages for the picoammeter is not sufficient, but since the instrument internally integrates for 333 ms (20 cycles of the line frequency in the U.S.A.), the reading is very stable in any case, and more than 2 – 3 averages are rarely needed.

The next item is labeled "Spex Int" and is typically grayed (read only). This allows setting the integration time of the analog input of the SPEX MSD2. This option will only accept values if a SPEX monochromator is attached, and is selected as either the primary or secondary instrument.

> Advice 7.1.c – CAUTION: There is unfortunately no way to distinguish between just a SPEX monochromator and a SPEX MSD2. This means that this option only makes sense if an actual MSD2 is attached to the computer on which Kottan Spec is operated.

Primary and secondary device lists all the devices that are attached. If there are two instruments of the same kind attached (as in 2 Keithley 485 picoammeters), they will be listed as 1. and 2. Picoammeter. Either one can act as the primary or the secondary

instrument. All instruments that can either act as ampere- and voltmeter will show up as both.

> Advice 7.1.d – CAUTION: As mentioned in Section 3.3. on page 115, neither the Keithley 1xx nor the SRS 530 can automatically switch between current and voltage measurements. Furthermore, the SRS 530 requires a different input to be used. Even worse, the SRS 530 does not allow any detection of which mode is the active mode, and the data sent back is always in volts, the amplification factor has to be applied by Kottan Spec – requiring the correct setting in the measurement dialog. The user has to ensure that both the instrument setting and the selection in the dialog are actually the same!

The last option, "Clear Minsens", is an extremely powerful utility if used correctly. The "Minsens", minimum sensitivity, makes sure the excessive change of measurement ranges on the selected instrument do not occur. This would delay the time required to measure one point. Basically, if the range is changed 3 times during the measurement of one point, the higher range of the two will be the new minimum sensitivity. During the first run of Kottan Spec, this value will be established for each of the used instruments. During a second, third, etc. run with the same conditions, most likely the minimum sensitivity will be the same, and the instrument will never change ranges due to reaching the noise level.

However, if a new sample is measured, the minimum sensitivity could be lower, and therefore "Clear Minsens" should be checked.

Finally, "OK" will bring you to the next dialog, "Cancel" cancels the execution of the measurement. "Update" is currently unused but may bear a function in an updated version. Please consult the "Readme" file coming with your installation.

The next dialog "Save Spectral as ASCII" allows you to specify a name and a directory. The file will be saved during the execution of the measurement and does not need to be saved separately. Even if the user aborts the measurement, all data acquired up to that point will be saved.

The default directory is set by the user selections in the initialization dialog (ref. Section 4.1. on page 116), as "Measurement Directory"\"User Name" from the dialog shown in Figure 87. If the measurement directory is "C:\Measurements" and the user name is "John Doe", the default directory will be: "C:\Measurements\John Doe\". The appearance of the dialog

"Save Spectral as ASCII" depends on the operating system. For Windows 2000, the dialog is shown in Figure 103 below. Dialogs will look similar for other Windows versions.

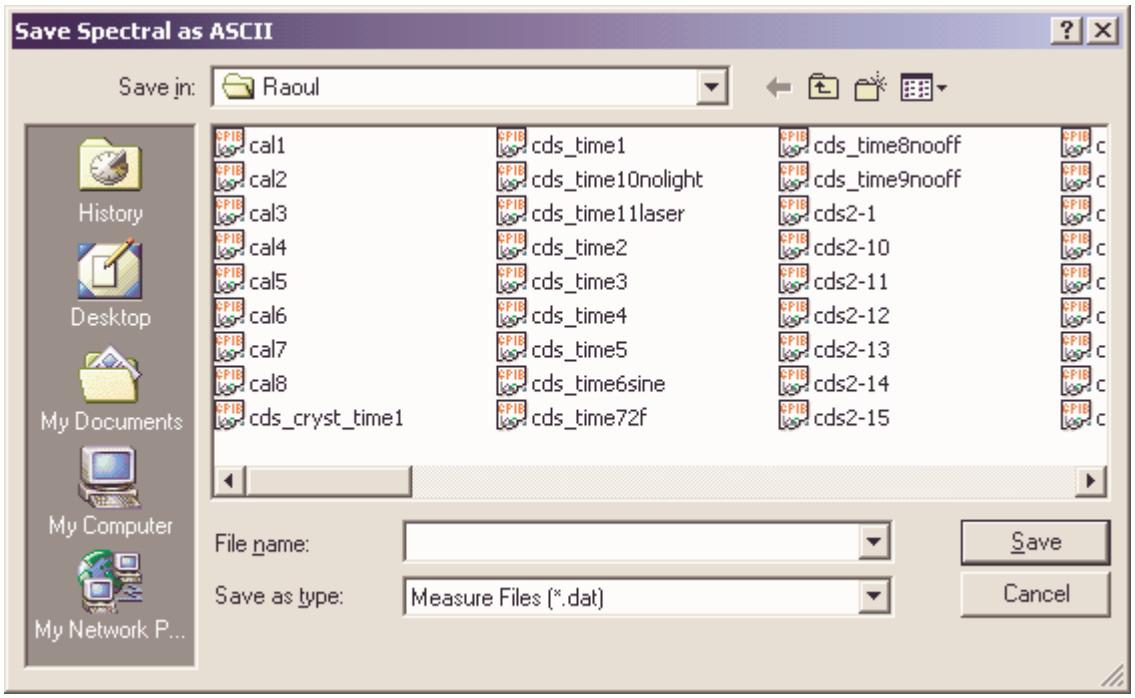

Figure 103 Dialog "Save Spectral as ASCII"

After entering a filename and clicking save, the status bar on the bottom of the screen will change to "Measuring", an estimated end of measurement time will be displayed, and the measurement will commence. If the user presses cancel, the measurement will not commence, and the program will return to the stand by mode.

7.2. Measurements involving a stage ("ZScan")

This measurement options allows to move or to rotate a stage along one axis while characterizing a sample with up to two instruments. The most common application would be a Z-Scan (using a translatory stage) or a far field illumination distribution (using a rotary stage). In this version of Kottan Spec this requires a Newport ESP 300 or compatible stage controller with the desired stage attached.

The measurement dialog will be very similar to the one shown in Figure 102 above, but the upper part reflects the specifics of the stage. The units of the From, To, Step fields will reflect the currently set units for that stage. They cannot be altered in this dialog. The fourth

field that was used to indicate the monochromator will now show the speed with which the stage shall move.

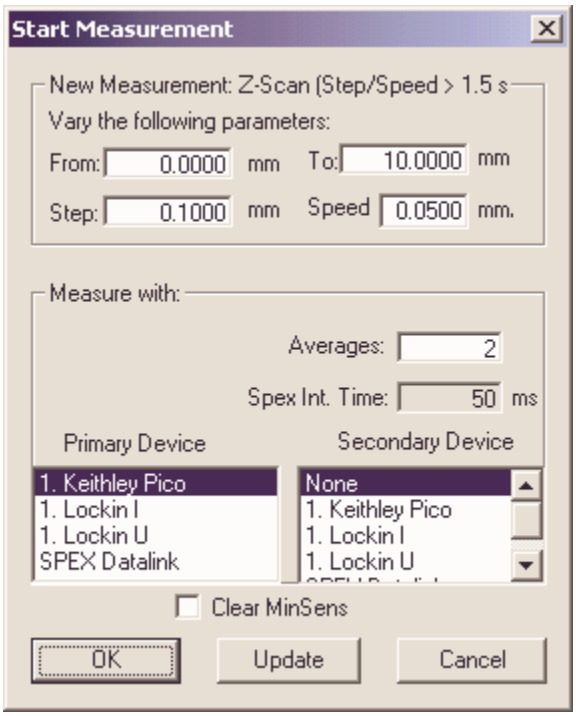

Figure 104 Dialog "Measurement: Z-Scan"

Advice 7.1.e – CAUTION: The From and To field reflect the position with respect to the home position of the stage (please refer to the ESP 300 manual for a definition of the home position), which can be set with the "Move Stage" dialog selectable from the "Manual Control" menu item. Be sure that the stage can move to these positions without being stopped by the end of the stage unit. The stage will automatically shut off at that point and may leave the program in a stage where the user needs to issue a "Stop Measurement" command.

Advice 7.1.f – CAUTION: Since the time to take a measurement is related to the number of averages, the program tries to make sure that the "Step" field only contains reasonable values. It is best for any stage to be run continuously, which is the default mode used by Kottan Spec. This means that the "Step" distance should be such that it takes the stage two times the

measurement time to run this distance. If that is not the case, the step distance may be higher than expected. The saved file will reflect this – in fact, the first column (position) of the saved file will be the average of the position just before the start of the measurement and the position directly afterwards. When in doubt, select a slower speed for the stage.

At the end of the measurement, the stage will return to the home position.

7.3. Time-dependent measurements

Often, it is just desired to monitor a device over time. This measurement option requires neither a monochromator nor a stage. The top section of the measurement dialog allows to give start, end, and step times. The step time, naturally, needs to be longer than the time it takes to complete the desired measurement. If this is not the case, the step time may be higher in the saved file. The time saved in the first column will reflect the average value of the time just before and after the measurement cycle.

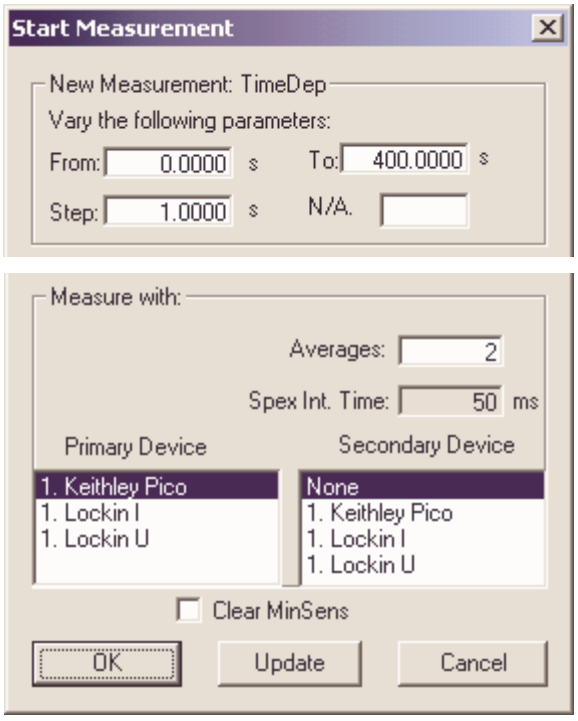

Figure 105 Dialog "Time Dependent Measurement"

Caution: Please keep in mind that ever "Step" timestep, 50 – 100 bytes are saved to disk. If the timestep is 1 s, and the measurement runs for a couple of hours, the resulting file may be huge. Please make sure that the computer running Kottan Spec has enough RAM and hard disk space. To give a rough idea: A measurement running for two hours with 5 s intervals will create about 100 to 200 kb of data.

7.4. Completed measurement

The stand by screen after a completed measurement run will look like this:

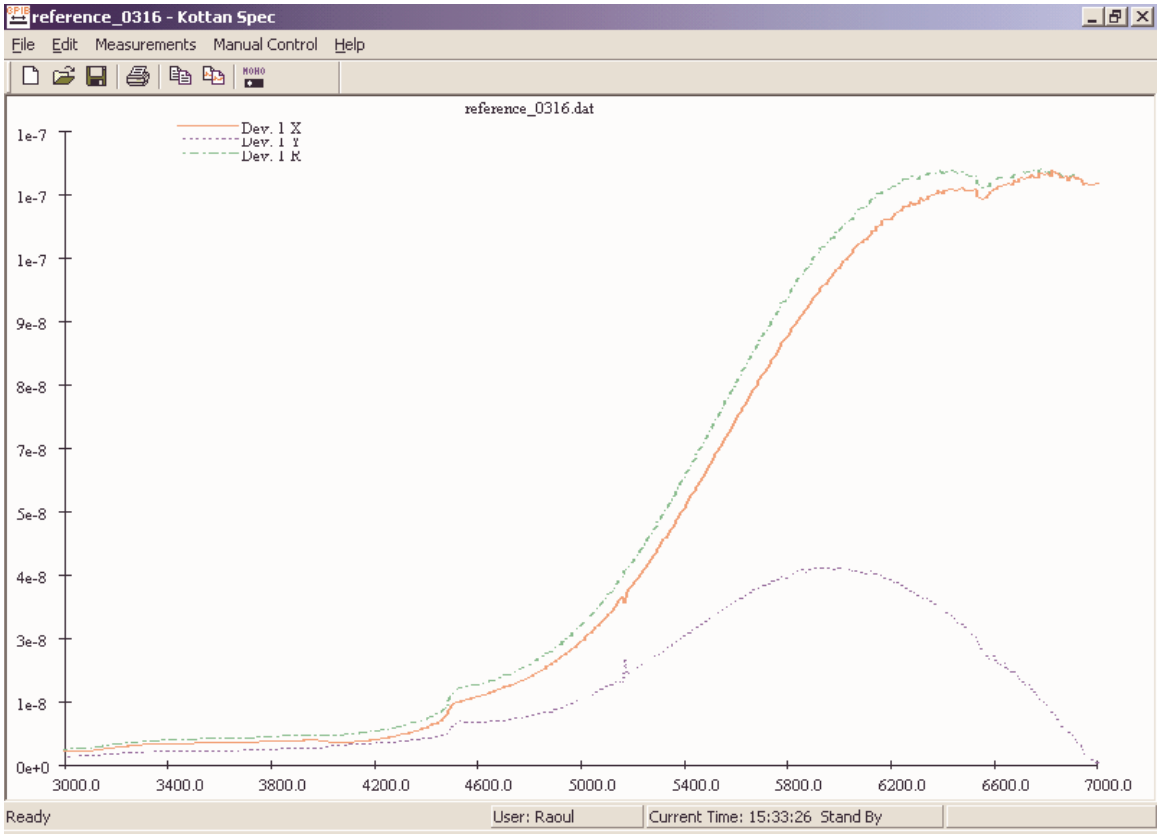

Figure 106 Spectral measurement shown on the screen

BIBLIOGRAPHY

1. M. Gussoni, C. Castigliani, G. Zerhc, "Spectroscopy of Advanced Materials", chapter 5, (john Wiley, New York, 1991)
2. Raoul Schroeder, Diploma Thesis, (1999).
3. eMagin corporation, http://www.emagin.com/svga+.pdf, OLED SVGA+ display data sheet.
4. Jaspirit Singh, *Semiconductor Optoelectronics*, (McGraw-Hill, New York, 1995).
5. Peter Yu, Manuel Cardona, *Fundamentals of Semiconductors*, (Springer, Berlin, 1996).
6. D. Beljonne, J. Cornil, R.H. Friend, R.A.J. Janssen, J.L. Brédas, *J. Am. Chem. Soc.* **118**, 6453-6456 (1996).
7. N.W. Ashcroft, N.D. Mermin, *Solid State Physics*, (Saunders College / HRW, Philadelphia, 1976).
8. G.H. Wannier *Phys. Rev.* **52**, 191-197 (1937).
9. J. Frenkel, *Phys. Rev.* **38**, 309-320 (1931).
10. C.H. Lee, G. Yu, D. Moses and A.J. Heeger, *Phys. Rev. B* **49**, 2396-2407 (1994)
11. M. Chandross, S. Mazumdar, S. Jeglinski, X. Wei. Z.V. Vardeny, E.W. Kwock and T.M. Miller, *J.Phys.:Condens.Matter* **6**, 1379-1394 (1994).
12. P. G. d. Costa and E. M. Conwell, *Am.Phys.Soc.-Rap.Comm.* **48**, 1993-1997 (1993)
13. R. N. Marks, J. J. M. Halls, D. D. C. Bradley, R. H. Friend and A. B. Holmes, *J. Phys.: Cond. Mat.* **6**,1379-1394 (1994).
14. S. Barth and H. Baessler, *Phys.Rev.Lett.* **79**, 4445-4448 (1997).
15. R. H. Friend, G. J. Denton, J. J. M. Halls, N. T. Harrison, A. B. Holmes, A. Koehler, A. Lux, S. C. Moratti, K. Pichler, N. Tessler and K. Towns, *Synth.Met.* **84**, 463-470 (1997).
16. J. Cornil, A.J. Heeger, and J.L. Bredas, *Chem. Phys. Lett.* **272**, 463-470 (1997).
17. R. H. Friend, G. J. Denton, J. J. M. Halls, N. T. Harrison, A. B. Holmes, A. Koehler, A. Lux, S. C. Moratti, K. Pichler, N. Tessler, K. Towns and H. F. Wittmann, *Solid State Communications* **102**, 249-258 (1997).
18. K. C. Kao and W. Hwang, *Electrical Transports in Solids - with Particular Reference to Organic Semiconductors*, (Pergamon Press, Oxford 1981).
19. C.J. Brabec, F. Padinger, N.S. Sariciftci, *J. Appl. Phys.* **85**, 6866 (1999).
20. G. Yu, G. Srdanov, H. Wang, Y. Cao, A. Heeger, *Organic Photonic Materials and Devices II* **3939**, 118 (2000).
21. M. Granstrom, K. Petritsch, A.C. Arias, A. Lux, M.R. Andersson and R. H. Friend. *Nature* **395**, 257-260 (1998).
22. W.R. Salaneck, Y. Ono, T. M. Granstrom, K. Petritsch, A.C. Arias and R. H. Friend, *Synth. Met.* **102**, 957-958 (1999).
23. J. H. Schön, Ch. Kloc, A. Dodabalapur, B. Batlogg, Science 289, 599-601 2000
24. Fesser, Bishop, Campbell, *Phys.Rev.B* **27**, 4804-4825 (1983).

25. E. J. W. List, J. Partee, J. Shinar, U. Scherf, K. Müllen, E. Zojer, K. Petritsch, G. Leising, W. Graupner, *Physical Review B* **61**, 10807-10814 (2000).
26. A. Köhler, D. A. dos Santos, D. Beljonne, Z. Shuai, J.-L. Bredas, A. B. Holmes, A. Kraus, K. Müllen, R. H. Friend, *Nature* **392**, 903-906 (1998).
27. W. Graupner, G. Cerullo, M. Nisoli, G. Lanzani, E. J. W. List, G. Leising, S. De Silvestri, *Phys. Rev. Lett.* **81**, 3259-3262 (1998).
28. D. Moses, J. Wang, G. Yu, A. J. Heeger, *Phys. Rev. Lett.* **80**, 2685 (1998).
29. V. I. Arkhipov, E. V. Emelianova, H. Bässler, *Phys. Rev. Lett.* **82**, 1321 (1999).
30. J.W. Baur, M.F. Rubner, J.R. Reynolds, S. Kim, *LANGMUIR 15:* **(19)**, 6460-6469 (1999).
31. R. Schroeder, G. Feistritzer, W. Graupner, G. Meinhardt, D. Berman, P. Preishuber-Pflügl, F. Stelzer, D. Faiman, G. Leising, *ANTEC 99 Proceedings* **III**, 3844-3848 (1999).
32. T. Piok, C. Brands, P. J. Neyman, A. Erlacher, C. Soman, M. A. Murray, R. Schroeder, W. Graupner, J. R. Heflin, D. Marciu, A. Drake, M. B. Miller, H. Wang, H. Gibson, H. C. Dorn, G. Leising, M. Guzy, R.M. Davis, *Synthetic Metals* **121,** 1589-1590 (2001).
33. E.J.W. List, C. Creely, G. Leising, B. Schlicke, A.D. Schlüter, U. Scherf, K. Müllen, W.Graupner, *SPIE Proceedings* **4105**, 450-463 (2001).
34. G. Decher and J. D. Hong, *Makromol. Chem., Makromol. Chem. Symp.* **46**, 321 (1991).
35. G. Decher, J. D. Hong, and J. Schmitt, *Thin Solid Films* **210/211**, 831 (1992).
36. A. C. Fou, O. Onitsuka, M. Ferreira, M. F. Rubner, and B. R. Hsieh, *J. Appl. Phys* **79**, 7501 (1996).
37. J-K. Lee, D. Yoo, and M. F. Rubner, *Chem. Mater.* **9**, 1710 (1997).
38. J.R. Heflin, C. Figura, D. Marciu, Y Liu, R.O. Claus, *Appl. Phys. Letters* **74**, 495 (1999).
39. M.J. Roberts, G.A. Lindsay, W.N. Herman, K.J. Wynne, *J. Am. Chem. Soc.* **120**, 11202 (1998).
40. R.A. Wessling, R.G. Zimmerman, *Journal of Polymer Science* **72**, 55(1985).
41. R.A. Wessling, *U.S. Patent* **3,401,152,3** ,152 (1968).
42. G. R. Hayes, I. D. W. Samuel, R. T. Philips, *Phys. Rev. B* **52**, 569 (1995).
43. R. Kersting, U. Lemmer, R.F. Mahrt, K. Leo, H. Kurz, H. Bässler, E.O. Göbel, *Phys. Rev. Letters* **70**, 3820 (1993).
44. G. Cerullo, G. Lanzani, S. DeSilvestri, C.J. Brabec, G. Zerza, N.S. Sariciftci, J.C. Hummelen,, *CLEO/QELS 2000 proceedings*, 245 (2000).
45. E.J.W. List, B. Schlicke, A.D. Schlüter, U. Scherf, K. Müllen, W. Graupner, G. Leising, *Chemical Physics Letters* **325**, 132 (2000).
46. R. Kersting, B. Mollay, M. Rusch, J. Wenisch, G. Leising, H. F. Kauffmann, *J. Chem Phys* **106**, 2850 (1997).
47. J. J. M. Halls, K. Pichler, R. H. Friend, S.C. Moratti, A.B. Holmes, *Appl. Phys. Lett.* **68** (22), 3120 (1996).

48. P. J. Hamer, K. Pichler, M. G. Harrison, R. H. Friend, B. Ratier, A. Moliton, S.C. Moratti, A.B. Holmes, *Philos. Mag.* **73**, 367 (1996).
49. M. Yan, L. J. Rothberg, F. Papadimitrakopoulos, M. E. Galvin, and T. M. Miller, *Phys. Rev. Lett.* **73**, 744-747 (1994)
50. F.Cacialli, R.H.Friend, N.Haylett, R.Daik, W.J.Feast, D. Santos, and J.L.Brédas, *Appl. Phys. Lett.* **69**, 3794 (1996)
51. S.T.Lee, Y.M.Wang, X.Y.Hou, and C.W.Tang, *Appl.Phys.Lett.* **74**, 670 (1999)
52. E.W. Forsythe, M.A. Abkowitz, Y. Gao, C.W. Tang, *J. Vac. Sci. Technol. A* **18**, 1869 (2000)
53. J.S. Wilson, A.S. Dhoot, A.J.A.B. Seeley, M. S. Khan, A.Köhler, R. H. Friend, *Nature* **413**, 428-431 (2001)
54. S.O. Barros, R. Stevens, W. Cranton, *Optical Engineering* **40**, 934-940 (2001)
55. A.J. Campbell, D.D.C Bradley, H. Antoniadis, M. Inbasekaran, W.W. Wu, E.P. Woo, *Appl. Phys. Lett.* **76**, 1734 (2000).
56. H. Sirringhaus, R.J. Wilson, R.H. Friend, M. Inbasekaran, W.W. Wu, E.P. Woo, M. Grell, D.D.C. Bradley, *Appl. Phys. Lett.* **77**, 406 (2000).
57. R.B. Fletcher, D.G. Lidzey, D.D.C. Bradley, M. Bernius, S. Walker, *Appl. Phys. Lett.* **77**, 1262 (2000).
58. U. Scherf and K. Müllen, Makromol. *Chem. Rapid Commun.* **12**, 489 (1991).
59. M. Wohlgenannt, W. Graupner, G. Leising, Z.V. Vardeny*, Phys. Rev. B* **60**, 5321 (1999).
60. S.-C. Yang, W. Graupner, S. Guha, P. Puschnig, C. Martin, H.R. Chadrasekhar, M. Chandrasekhar, G. Leising, C. Ambrosch-Draxl, U. Scherf, *Phys. Rev. Lett.* **85**, 2388 (2000).
61. M. Grell, D.D.C. Bradley, G. Ungar, J. Hill, K.S. Whitehead, *Macromolecules* **32**, 5810 (1999).
62. G. Lieser, M. Oda; T. Miteva, A. Meisel, H.-G. Nothofer, U. Scherf, D. Neher, *Macromolecules* **33**, 4490 (2000).
63. S. Tasch, E. J. W. List, O. Ekström, W. Graupner, G. Leising, P. Schlichting, U. Rohr, Y. Geerts, U. Scherf, and K. Müllen*, Appl. Phys. Lett.* **71**, 2883 (1997).
64. M. Nisoli, S. Stagira, M. Zavelani-Rossi, S. De Silvestri, P. Mataloni, C. Zenz, *Phys. Rev. B* **59**, 11328 (1999).
65. R. Schroeder, B. Ullrich, W. Graupner and U. Scherf, *J. Phys. Condens. Matter* **13**, L313 (2001).
66. M. Cha, W.E. Torruellas, G.I. Stegeman, W.H.G. Horsthuis, G.R. Möhlmann, J. Meth, *Appl. Phys. Lett.* **65**, 2648 (1994).
67. Y. Shen, D. Jakubcyk, F. Xu, J. Swiatkiewicz, P.N. Prasad, B.A. Reinhardt, *Appl. Phys. Lett.* **76**, 1 (2000).
68. F. Li, Y. Song, S. Liu, C Li., Y. Wu, X. Zuo, C. Yu, P. Zhu, *J. Appl. Phys.* **82**, 2004 (1997).
69. N. Sanz, A. Ibanez, Y. Morel, P.L. Baldeck, *Appl. Phys. Lett.* **78**, 2569 (2001).
70. M. Gu, J.O. Amistoso, A. Toriumi, M. Irie, S. Kawata, *Appl. Phys. Lett.* **79** (2001).

71. S.H. Guang, J.D. Bhawalkar, C.F. Zhao, P.N. Prasad, *Appl. Phys. Lett.* **67**, 2433 (1995).
72. J.-F. Lami, C. Hirlimann, *Phys. Rev. B* **60**, 4763 (1999).
73. Hyatt M. Gibbs, *"Optical Bistability: Controlling Light with Light"*, (Academic Press Inc, Orlando, 1985), p.25.
74. C.M. Heller, I.H. Campbell, B.K. Laurich, D.L. Smith, D.C.C. Bradley, P.L. Burn, J.P. Ferraris, K. Müllen, *Phys. Rev. B* **54**, 5516 (1996).
75. C.H. Henry, R.A. Logan, K.A. Bertness, *Journal of Applied Physics* **52**, 4457-4461 (1981).
76. W. Drube, D. Straub, F.J. Himpsel, *Phys. Rev. B* **35**, 5563-5568 (1987).
77. K.E. Gonsalves, S.P. Rangarajan, G. Carlson, *Appl. Phys. Lett.* **71**, 2175-2177 (1997).
78. A.J. Steckl, M. Garter, R. Birkhahn, *Appl. Phys. Lett.* **73**, 2450-2452 (1998).
79. A J Steckl, M Garter, D S Lee, *Appl. Phys. Lett.* **75**, 2184-2186 (1999).
80. H. Ariza-Calderon, R. Lozada-Morales, O. Zelaya-Angel, *J. Vac. Sci. Technol. A* **14**, 2480-2482 (1996).
81. B.J. Wu, L.H. Kuo, J.M. DePuydt, *Appl. Phys. Lett.* **68**, 379-381 (1996).
82. B. Ullrich, H. Ezumi, S. Keitoku, T. Kobayashi, *Mater. Sci. Eng. B* **117**, 117-119 (1995).
83. B. Ullrich, H. Sakai, N. M. Dushkina, H. Ezumi, S. Keitoku, T. Kobayashi, *Mater. Sci. Eng. B* **47**, 187-189 (1997).
84. B. J. Feldman, J. A. Duisman, *Appl. Phys. Lett.* **37**, 1092-1093 (1982).
85. C. Mejía-García, A. Escamilla-Esquivel, G. Contreras-Puente, M. Tufiño-Velázquez, M. L. Albor-Aguilera, O. Vigil, L. Vaillant, *J. Appl. Phys.* **86**, 3171-3174 (1999).
86. C. Bouchenaki, B. Ullrich, J. P. Zielinger, *J. Lum.* **48/49**, 649-654 (1991).
87. R. Takahashi, *J. Lum.* **24/25**, 67-70 (1981).
88. M. Claybourn, M. D. Scott, J. O. Williams, and R. C. Goodfellow, *J. Crystal Growth* **58**, 417-423 (1982).
89. T. Yodo, S. Tanaka, *J. Appl. Phys.* **72**, 2781-2790 (1992).
90. M. Gracia-Jimenez, G. Martinez, J. L. Martinez, E. Gomez, and A. Zehe, *J. Electrochem. Soc.* **131**, 2974-2977 (1984).
91. O. Zelaya-Angel, A. E. Esparza-Garcia, C. Falcony, R. Lozada-Morales, and R. Ramirez-Bon, *Solid State Commun.* **94**, 81-85 (1995).
92. O. de Melo, L. Hernandez, O. Zelaya-Angel, R. Lozada-Morales, M. Becerril, and E. Vasco, *Appl. Phys. Lett.* **65**, 1278-1280 (1994).
93. M. Ichimura, F. Goto, and E. Arai, *J. Appl. Phys.* **85**, 7411-7417 (1998).
94. C. T. Tsai, D. S. Chuu, G. L. Chen, and S. L. Yang, *J. Appl. Phys.***79**, 9105-9109 (1996).
95. C.E. Morosanu, *"Thin Films by Chemical Vapour Deposition"*, (Elsevier, Amsterdam, 1990)
96. W.M. Feist, S.R. Steele, D.W. Ready, Phys. Thin Film 5, 237 (1969)
97. A. Yoshikawa, Y. Sakai, *J. Appl. Phys.* **45**, 3521 (1974); *Jpn. J. Appl. Phys.* **16**, 1203 (1974)

98. Periodic Table and Materials Data, www.webelements.com.
99. E.F. Schubert, *"Doping in III-V Semiconductors"*, (Cambridge Univeristy Press, New York, 1993).
100. D.M. Bagnall, B. Ullrich, H. Sakai, Y. Segawa, *Optics Lett.* **25**, 757-760 (1999).
101. D.M. Bagnall, B. Ullrich, H. Sakai, Y. Segawa, *J. Crystal Growth* **214/215**, 1015-1018 (2000).
102. H. Sakai, T. Tamaru, T. Sumomogi, H. Ezumi, and B. Ullrich, *Jpn. J. Appl. Phys.* **37**, 4149 (1998).
103. B. Ullrich, H. Sakai, and Y. Segawa, *Thin Solid Films* **385**, 220 (2001).
104. W. van Roosbroeck, W. Shockley, *Phys. Rev.* **94**, 1558 (1954).
105. J.I. Pankove, *"Optical Processes in Semiconductors"*, (Dover, NewYork, 1971)
106. B. Ullrich, D. M. Bagnall, H. Sakai, and Y. Segawa, *Solid State Commun.* **109**, pp. 757-760 (1999).
107. B. Ullrich, D. M. Bagnall, H. Sakai, and Y. Segawa, *J. Lum.* **87-89**, 1162-1164, (2000).
108. T. D. Krauss and F. W. Wise, *Appl. Phys. Lett.* **65**, 1739-1741 (1994).
109. C. Bouchenaki, B. Ullrich, J.P. Zielinger, H.N. Cong, P. Chartier, *J. Opt. Soc. Am B* **8**, 691 (1991)
110. W.A. Strifler, C.W. Bates Jr, *J. Appl. Phys.* **71**, 4358 (1992).
111. R. Schroeder, B. Ullrich, W. Graupner, U. Scherf *J.Phys: Condens.* Matter **13**, L313 (2001)
112. Z. Xu, X. Zou, X. Zhou, B. Zhao, C.W. Wang, and Y. Hamakawa, *J. Appl. Phys.* **75**, 588-595 (1994).
113. A. Hübner, A.G. Aberle, and R. Hezel, *Appl. Phys. Lett.* **70**, 1008-1010 (1996).
114. A. Niemegeers, and M. Burgelman, *J. Appl. Phys.* **81**, 2881-2886 (1996).
115. B.-C. Chung, G.F. Virshup, M. Klausmeier-Brown, M. Ladle Ristow, and M.W. Wanlass, *Appl. Phys. Lett.* **60**, 1691-1693 (1992).
116. C.W. Tang, *Appl. Phys. Lett.* **48**, 183-185 (1986).
117. J.H. Schön, Ch. Kloc, and B. Batlogg, *Appl. Phys. Lett.* **77**, 2473 – 2475 (2000).
118. V.I. Yudson, P. Reineker, and V.M. Agranovich, *Phys. Rev. B* **52**, R5543-5545 (1995).
119. S. Guha, R.A. Haight, N.A. Bojarczuk, and D.W. Kisker, *J. Appl. Phys.* **82**, 4126-4128 (1997).
120. X. Yang, and X. Xu, *Appl. Phys. Lett.* **77**, 797-799 (2000).
121. W.M.K.P. Wijekoon, M.Y.M Kyktey, P.N. Prasad, and J.F. Garvey, *Appl. Phys. Lett.* **67**, 1698-1699 (1995).
122. F. Bassani, G.C. La Rocca, D.M. Basko, and V.M. Agranovich, *Phys. Sol. State* **41**, 701-703 (1999).
123. B. Ullrich, H. Sakai, N. M. Dushkina, H. Ezumi, S. Keitoku, T. Kobayashi, *Microelect. Engng.* **43/44**, 695-700 (1998).
124. H. Sakai, T. Tamaru, T. Sumomogi, H. Ezumi, B. Ullrich, *Jpn. J. Appl. Phys. Part 1* **37**, 4149-4153 (1998).
125. Peter Würfel, *"Physik der Solarzellen"*, (Spektrum Akademischer Verlag, Heidelberg, 2000)

126. R.F.M. Hendricks, M.P. van Exter, J.P. Woerdman, A. van Geelen, L. Weegels, K.H. Gulden, M. Moser, "Electro-optic birefringence in semiconductor vertical-cavity lasers", Appl. Phys. Lett., vol. 71, pp. 2599-2601, 1997.
127. D. Burak, S.A. Kemme, R.K. Kostuk, R. Binder, Appl. Phys. Lett. 73, 3501-3502 (1998).
128. S.J. Sweeney, G. Knowles, T.E. Sale, Appl. Phys. Lett. 78, 865-867 (2001).
129. D.K. Serkland, K.D. Choquette, G.R. Hadley, K.M. Geib, A.A. Allerman, "Two-element phased array of antiguided vertical-cavity lasers", Appl. Phys. Lett., vol. 75, pp. 3754 – 3756, 1999.
130. J.M. Redwing, D.A.S. Loeber, N.G. Anderson, M. A. Tischler, J.S. Flynn, Appl. Phys. Lett. 69, 1-3 (1996).
131. B. Pezeshki, M. Hagberg, M. Zelinski, S.D. DeMars, E. Kolev, R.J. Lang, IEEE Phot. Techn. Lett. 11, 791-793 (1999).
132. O. Imafuji, T. Fukuhisa, M. Yuri, M. Manno, A. Yoshikawa, K. Itoh, IEEE J. Sel. Top. Quant. Elec. 5, 721 – 725 (1999).
133. M. Kondow, S. Minagawa, J. Appl. Phys. 64, 793 – 796 (1988).
134. M. Guina, J. Dekker, A. Tukainen, S. Orsila, M. Saarinen, M. Dumitrescu, P. Sipalä, P. Savolainen, M. Pessa, J. Appl. Phys. 89, 1151-1155 (2001).
135. A. Oster, M. Zorn, K. Vogel, J. Fricke, J. Sebastian, W. John, M. Weyers, G. Tränkle, SPIE proceedings for Photonics West, 2001, (in print).
136. A. Knigge, M. Zorn, H. Wenzel, M. Weyers, G. Tränkle, Electronic Letters 37, 1222-1223 (2001).
137. A. Bhattacharya, M. Zorn, A. Oster, M. Nasarek, H. Wenzel, J. Sebastian, M. Weyers, G. Tränkle, J. of Cryst. Growth 221, 663-667 (2000).
138. M. D. Dvorak, B. L. Justus, D. K. Gaskill, and D. G. Hendershot, Appl. Phys. Lett., 66, 804-806 (1995).
139. B. Ullrich and R. Schroeder, Semicond. Sci. Technol. 16, L37-39 (2001).
140. M. Bleicher, "Halbleiter-Optoelektronik", (Dr. Alfred Hüthig Verlag, Heidelberg, Germany, 1986).
141. P. Y. Yu and B. Welber, Solid State Commun. 25, 209-211 (1978).
142. V. Vilokkinen, P. Sipilä, P. Melanen, M. Saarinen, S. Orsila, M. Dumitrescu, P. Savolainen, M. Toivonen, M. Pessa, Mat. Sci. Eng. B 74, 165-167 (2000).
143. X. H. Zhang, S. J. Chua, W. J. Fan, Appl. Phys. Lett. 32, 1098-1100 (1998).
144. O. Madelung (editor), "Data in Science and Technology: Semiconductors, Group IV Elements and III-V Compnds", (Springer Verlag, Heidelberg, Germany, 1991).

LIST OF PUBLICATIONS

1. "Photovoltaic Properties of Multilayer and Molecularly Doped Organic Devices",

   G. Meinhardt, W. Graupner, G. Feistritzer, R. Schroeder, E.J.W. List, A. Pogantsch, G. Dicker, B. Schlicke, A. D. Schlüter, G. Winter, M. Hanack, U. Scherf, K. Müllen, G. Leising,

   SPIE Proceedings **3623**, 46-57 (1999)

2. "Organic Solar Cells - Stabilization by Plastic Encapsulation",

   R. Schroeder, G. Feistritzer, W. Graupner, G. Meinhardt, D. Berman, P. Preishuber-Pflügl, F. Stelzer, D. Faiman, G. Leising, Society of Plastics Engineers,

   Technical Papers - ANTEC 99 **III**, 3844-3848 (1999)

3. "Photovoltaic Effect in Multilayer Organic Systems",

   G. Meinhardt, E. Moderegger, R. Schroeder, G. Winter, M. Hanack, H. Quante, Y. Geerts, K. Müllen, H. Tillmann, H.-H. Hörhold, G. Leising,

   Materials Research Society, Fall 1999 Proceedings, Symposium BB (online) (1999)

4. "Photovoltaic Responses in Ionically Self-Assembled Nanostructures Containing Conjugated Polymers and Fullerenes",

   C. Brands, T. Piok, P. J. Neyman, A. Erlacher, C. Soman, M. A. Murray, R. Schroeder, J. R. Heflin, W. Graupner, D. Marciu, A. Drake, M. B. Miller, H. Wang, H. Gibson, H. C. Dorn, G. Leising, M. Guzy, R.M. Davis,

   SPIE Proceedings **3937**, 51-62 (2000)

5. "Efficient Charge Generation in Conjugated Molecules",

   W. Graupner, T. Piok, C. Brands, P. J. Neyman, A. Erlacher, C. Soman, M. A. Murray, R. Schroeder, J. R. Heflin, D. Marciu, A. Drake, M. B. Miller, H. Wang, H. Gibson, H. C. Dorn, G. Leising, M. Guzy, R.M. Davis,

   Abstracts of Papers of the American Chemical Society **220: 258-PMSE**, Part 2, Aug 20, (2000)

6. "Photovoltaic Cells Based on Ionically Self-Assembled Nanostructures",

   T. Piok, C. Brands, P. J. Neyman, A. Erlacher, C. Soman, M. A. Murray, R. Schroeder, W. Graupner, J. R. Heflin, D. Marciu, A. Drake, M. B. Miller, H. Wang, H. Gibson, H. C. Dorn, G. Leising, M. Guzy, R.M. Davis,

   Synthetic Metals **116**, 343-347 (2001)

7. "Photocarrier Generation Quantum Yield For Ionically Self-Assembled Monolayers",

T. Piok, R. Schroeder, C. Brands, J. R. Heflin, G. Leising, W. Graupner,

Synthetic Metals **121**, 1589-1590 (2001)

8. "Control of Excited State Dynamics in Ionically Self-Assembled Monolayers of Conjugated Molecules",

   R. Schroeder, J. R. Heflin, H. Wang, H. Gibson, W. Graupner,

   Synthetic Metals **121**, 1521-1524 (2001)

9. "Photoluminescence Studies On Energy Migration in Multilayer Organic Photovoltaic Devices based on Ionically Self-Assembled Monolayers",

   R. Schroeder, C. Soman, C. Brands, J. R. Heflin, W. Graupner, H. Wang, H. Gibson, D. Marciu, M. B. Miller,

   SPIE Proceedings **4108**, 85-96 (2001)

10. "Two-Photon Absorption Properties of Soluble Phenylene-Based Polymers",

    R. Schroeder, W. Graupner, U. Scherf, B. Ullrich,

    Materials Research Society Symposium Proceedings (in print)

11. "Excitation Density and Photoluminescence Studies of Polyfluorene Excited by Two-photon Absorption",

    R Schroeder, B Ullrich, W Graupner and U Scherf,

    J. *Phys.: Condens. Matter* **13**, L313-L318 (2001)

12. "Green emission and bandgap narrowing due to two-photon excitation in thin film CdS formed by spray pyrolysis",

    B. Ullrich, R. Schroeder,

    Semicond. Sci. Technol. **16**, L37-L39 (2001)

13. "The influence of self-absorption on the photoluminescence of thin film CdS demonstrated by two-photon absorption",

    B. Ullrich, R. Schroeder, W. Graupner, H. Sakai,

    Optics Express **9, No.3** 116-120 (2001)

14. "Green Single and Two-Photon Gap Emission of Thin Film CdS Formed by Infrared Pulsed-Laser Deposition on Glass",

    B. Ullrich, R. Schroeder,

    Journal of Quantum Electronics, 37 No. 10, 1363-1367 (2001).

15. "Intrinsic gap emission and its geometry dependence of thin film CdS excited by two-photon absorption",

B. Ullrich, R. Schroeder, H. Sakai,

Semicond. Sci. Technol. **16**, L89-L92 (2001)

16. "Two-photon excited green emission of oriented thin film CdS on glass formed by laser deposition",

    B. Ullrich, R. Schroeder, H. Sakai, A. Zhang, S. Z. D. Cheng,

    Appl. Phys. Lett. (in print)

17. "Direct observation of intrachain exciton quenching in ladder-type polyparaphenylene",

    R. Schroeder, W. Graupner, U. Scherf, B. Ullrich,

    J. Chem. Phys. (accepted for publication)

Appendix D: Resumé

RESUMÉ

RESEARCH OBJECTIVE:

Thin film deposition, ultra-fast laser spectroscopy, and modulation respectively CW spectroscopy of II-VI, III-V, and organic semiconductors.

SKILLS:

- Four years of research experience with optoelectronic devices, strong background in organic semiconductors, expertise in analysis of physical properties of II-VI and III-V semiconductor structures
- Four years of experience in designing characterization setups – optical setup, GPIB controlled instruments; PC aided measurements in C, C++, monochromatic and laser excitation for photocurrent and photoluminescence experiments
- Network skills: LANs, SMB servers, web servers; programming experience: C, C++, Visual C++, MFC; Fortran, Assembler, Pascal; OS: Windows NT, 2000; FreeBSD
- Team work and team leading, teaching experience, presentation experience, organizational work
- Fluency in English, fluency in French, German native speaker

EDUCATION:

Virginia Tech, Blacksburg, VA
PhD in physics *(1999 – December 2001)*

- Student in Dr. Wilhelm Graupner's group
- Research in collaboration with Dr. James R. Heflin's group
- Research assistant in Dr. Bruno Ullrich's group, Center for Materials Science, Bowling Green State University
- Member of the physics honor society, ΣΠΣ, and the Materials Research Society

Technische Universität Graz, Austria
B.S. and M.S. in physics *(1993 – 1999)*

- Graduated with honors in December 1999

Université de Genève, Geneva, Switzerland
ERASMUS exchange student *(1996 – 1997)*

- Laboratory research on epitactically deposited ferroelectrics

RELEVANT EXPERIENCE:

TEACHING CONSULTANT
May to June 2001 — Bowling Green State University

- Summer workshop: Measuring Techniques in Optoelectronics

TEACHING ASSISTANT
August 1999 to May 2000 — Virginia Tech, Blacksburg, VA

- Grading for general physics 2205
- Teaching and grading for general physics lab 2215

DEVELOPMENT ASSISTANT
November 1997 to February 1998 — ADRES, Graz, Austria

- Design of a phosphorimeter
- Creation and implementation of measuring software

DEVELOPMENT ASSISTANT
February to March 1998 — ADRES, Graz, Austria

- Evaluation of photoluminescent materials in 1998
- Stability measurements

TEACHING ASSOCIATE
1995, 1996, 1998, 1999 — Technische Universität Graz, Austria

- Exercises, grading, exams for an introductory course in Fortran 90 for physicists
- Exercises, office hours, exams for an advanced excel course for mechanical engineers

ADDITIONAL EXPERIENCE:

- System administrator and content creator for “kottan-labs.bgsu.edu"
- President of the IAESTE (International Association for the Exchange of Students for Technical Experience) Graz (1999)
- Co-hosted the TECONOMY jobfair / exposition for the IAESTE (1998 and 1999)

PUBLICATIONS:

- 17 Publications in refereed journals and conference proceedings
- List of publication is shown in detail above